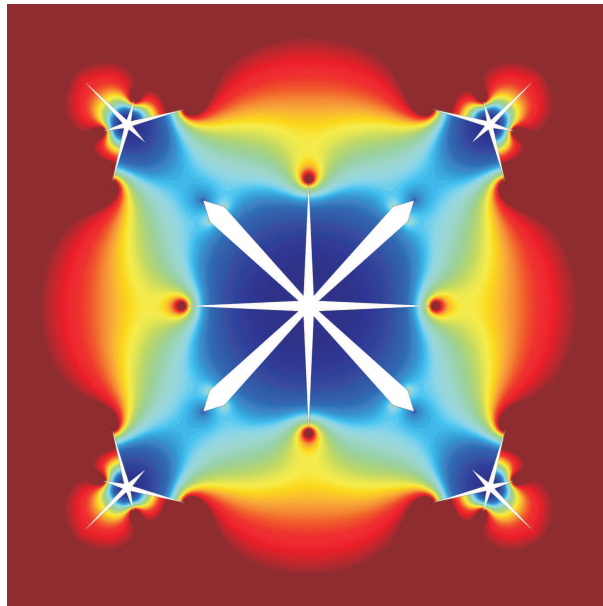




UNIVERSITY
OF TRENTO – Italy

Summer Shahzad

STRESS SINGULARITIES, ANNIHILATIONS
AND INVISIBILITIES INDUCED BY
POLYGONAL INCLUSIONS IN
LINEAR ELASTICITY



April, 2016

University of Trento
University of Bergamo
University of Brescia
University of Padova
University of Trieste
University of Udine
University IUAV of Venezia

Summer Shahzad

STRESS SINGULARITIES, ANNIHILATIONS AND
INVISIBILITIES INDUCED BY POLYGONAL
INCLUSIONS IN LINEAR ELASTICITY

Advisor: Prof. Davide Bigoni
Co-Advisor: Dr. Francesco Dal Corso

2016

UNIVERSITY OF TRENTO

Engineering of Civil and Mechanical Structural Systems

XXVIII cycle

Ph.D. Program Head: Prof. Davide Bigoni

Final Examination: April 21, 2016

Board of Examiners:

Prof. Alexander Movchan, University of Liverpool

Prof. Bozidar Stojadinovic, ETH Zürich

Prof. Daniele Zonta, University of Trento

Dedicated to my beloved wife Anna and family

Synopsis

Notches, wedges, cracks, stiffeners, inclusions and defects in plane elastostatics are known to generate singular stresses and limit the overall strength of a composite material.

In the present thesis, after showing experimentally that the singular stress field predicted by the linear elastic solution for the rigid inclusion model can be generated in reality and with great accuracy within a material, attention is devoted then in achieving the out-of-plane response of an infinite plane containing polygonal and hypocycloidal-shaped voids and rigid inclusions subject to generalized remote loading conditions.

The analytical solution obtained for the case of polygonal inclusions shows some unexpected and interesting features such as an infinite set of geometries and loading conditions exist for which not only the singularity is absent, but the stress vanishes (annihilates) at the corners. Thus the material, which even without the inclusion corners would have a finite stress, remains unstressed at these points in spite of the applied remote load. Moreover, similar conditions are determined in which a star-shaped crack or stiffener leaves the ambient stress completely unperturbed, thus reaching a condition of ‘quasi-static invisibility’.

The solution in closed-form is also obtained for the case of hypocycloidal-shaped voids and rigid inclusions, showing that cusps may in certain conditions act as stress reducers, situations for which the stress at the cusp tip in the presence of the inclusion is smaller than in the case when the inclusion is absent.

The obtained solutions provide closed-form expressions for Stress Intensity Factors and Notch Stress Intensity Factors at varying the inclusion geometry and of loading conditions, fundamental quantities in defining criteria of fracture initiation/propagation or inclusion detachment.

The findings of stress annihilation, stress reduction and inclusion invisibility define optimal loading modes for the overall strength of a composite and are useful in the design of ultra-resistant materials.

Acknowledgements

First and foremost, I would like to express my gratitude to Professor Davide Bigoni and Dr. Francesco Dal Corso for their constant patience, encouragements, motivation, suggestions and support given to me throughout the doctoral period.

I am also deeply grateful to Dr. Luca Argani, Dr. Gourgiotis, P.A., Dr. Andrea Bacigalupo, Dr. Daniele Veber, Dr. Bosi Federico, Dr. Diego Misseroni and Dr. Diego Pedrazzoli for their help and to all members of the Solid and Structural Mechanics Group at the University of Trento.

Moreover, I would like to thank my beloved wife Anna for her constant support and love.

A special thanks goes to my family: mom Treeza, Dad Sardar, mom Sabrina, Augusto, Uzma, Lubna, Elena, Aurora.

Last but not the least, thanks go to Bruno Fronza, Rita Ruffoli, Don Rino Breoni, Sir Abbas and Madam Shafqat, Ritor, Piero and Rose Mussi, Ruperto Battiston, Andrew Camelleri, Alessandro Maggi, Fondazione San Zeno, Focolare Movement, Mario Franzoia and family, Andrea Delama and family, Mario Farina and family, Luca Perolo, Andrea Perolo and family, Bruna, Franco Mucchiut and family, to all the gen and friends that i did not mention because of the limited space.

Finally, the financial support from the ERC Advanced Grant ‘Instabilities and nonlocal multiscale modelling of materials’ ERC-2013-ADG-340561- INSTABILITIES (2014-2019) is gratefully acknowledged.

Trento, March 21, 2016

Summer Shahzad

Scientific articles

The main results presented in this thesis have been summarized in the following papers:

1. **Shahzad, S.**, Dal Corso, F., and Bigoni, D. (2016)
Hypocycloid inclusions in nonuniform out-of-plane elasticity: stress singularity vs stress reduction.
Submitted.
2. Dal Corso, F., **Shahzad, S.**, Bigoni, D. (2016)
Isotoxal star-shaped polygonal voids and rigid inclusions in a nonuniform antiplane shear fields. I. Formulation and full-field solution.
International Journal of Solids and Structures,
doi:10.1016/j.ijsolstr.2016.01.027.
3. Dal Corso, F., **Shahzad, S.**, Bigoni, D. (2016)
Isotoxal star-shaped polygonal voids and rigid inclusions in nonuniform antiplane shear fields. II. Stress singularities, stress annihilation and inclusion invisibility.
International Journal of Solids and Structures,
doi:10.1016/j.ijsolstr.2016.01.026.
4. Misseroni, D., Dal Corso, F., **Shahzad, S.**, Bigoni, D. (2014)
stress concentration near stiff inclusions: validation of rigid inclusion model and boundary layers by means of photoelasticity.
Engineering Fracture Mechanics, 121-122, 87-97.

Contents

Published papers	ix
Contents	xi
1 Introduction	1
Introduction	1
2 Method of analytic functions and plane elasticity	7
2.1 Out-of-plane problem	8
2.2 In-plane problem	10
2.2.1 Airy Stress Function	11
2.3 Conformal mapping applied to plane elastic systems	13
2.3.1 Out-of-plane problem in conformal plane	13
2.3.2 In-plane problem in conformal plane	13
2.4 Schwarz-Christoffel conformal mapping	14
2.4.1 Exterior to exterior	14
2.4.2 Interior to exterior	17
2.4.3 Exterior to interior	18
2.4.4 Interior to interior	18
2.5 Isotoxal star-shaped polygons: exterior to exterior mapping	19
2.5.1 Special cases of star-shaped cracks and stiffeners . .	25
2.6 Hypocycloidal inclusions: exterior to exterior mapping . .	26
2.7 Elliptical inclusions	28

3	Experimental validation of rigid inclusion model	29
3.1	Introduction	29
3.2	Theoretical linear elastic fields near rigid polygonal inclusions	31
3.2.1	Asymptotic fields near the corner of a rigid wedge . .	31
3.2.2	Full-field solution for a polygonal rigid inclusion . .	33
3.3	Photoelastic elastic fields near rigid polygonal inclusions . .	37
4	Formulation and analytical solution for nonuniform out-of-plane problem	45
4.1	Introduction	45
4.1.1	An infinite class of antiplane shear fields	47
4.1.2	Asymptotic solution	50
4.2	Full-field solution	53
4.2.1	Closed-form solution for star-shaped cracks or stiffeners	54
4.2.2	Closed-form solution for isotoxal star-shaped polygonal inclusions	57
4.2.3	Shear stress analogies	58
5	Stress singularities, invisibilities and stress annihilations	61
5.1	Introduction	62
5.2	Stress and Notch Intensity Factors	63
5.2.1	Closed-form formulae of SIFs for star-shaped cracks or stiffeners	64
5.2.2	Closed-form formulae of NSIFs for isotoxal star-shaped voids and rigid inclusions	67
5.3	Stress fields, annihilation and invisibility	72
5.3.1	The rules of invisibility and annihilation	76
5.3.2	Partial-invisibility and Partial-annihilation	77
5.3.3	Beyond the hypotheses of infinite matrix and regular shape inclusion	77
6	Stress singularities vs stress reductions	85
6.1	Introduction	86
6.2	Closed-form solution for hypocycloidal-shaped inclusion . .	87
6.2.1	Stress Intensity Factors	92
6.2.2	Stress Reduction Factors	96

A	Fundamental equations in linear elasticity	103
A.1	Basic Formulas	103
A.1.1	Direct constitutive law	105
A.1.2	Inverse constitutive law	107
A.2	Plane elasticity	107
A.2.1	Plane stress problem	107
A.2.2	Plane strain problem	108
A.2.3	A general stress-strain relationship in in-plane elasticity	110
B	Some theorems in complex analysis with related examples	111
B.1	Cauchy Residue Theorem	111
B.2	Cauchy Integral Formula	114
	Bibliography	117

Chapter 1

Introduction

The determination of the mechanical fields near a crack, a stiffener, a notch, a wedge, an inclusion, or a defect in an elastic matrix material is a key problem for the engineering design of composites. In fact, stress fields around these types of inclusion exhibit strong stress concentrations, leading to a severe limitation of the composite strength.

In the present thesis, the experimental validation of the rigid inclusion model is proven through the comparison of the singular stress fields and the photoelastic observations. Moreover, some unexpected and surprising features such as stress annihilation, stress reduction, and inclusion invisibility are discovered for special inclusion geometries and loading conditions.

Chapter 2 is dedicated to the presentation of analytical methods used to obtain full-field solutions for mechanical fields. In chapter 3 asymptotic and full-field solution have been reported for rectangular and rhombohedral rigid inclusions, embedded in an infinite elastic matrix subject to remote uniform tensile stress. The singular behaviour of the linear elastic solution for the stress field at the tips of the rigid inclusion vertexes is experimentally confirmed by means of photoelastic tests¹. This result shows that elastic stress fields can be generated in reality with great accuracy, as shown in figure 1.1 and that the rigid inclusion model is a reliable mathematical representation of stiff inclusion embedded in a soft matrix.

¹All the experiments have been performed at the Instabilities Lab of the Department of Civil, Environmental and Mechanical Engineering of the University of Trento.

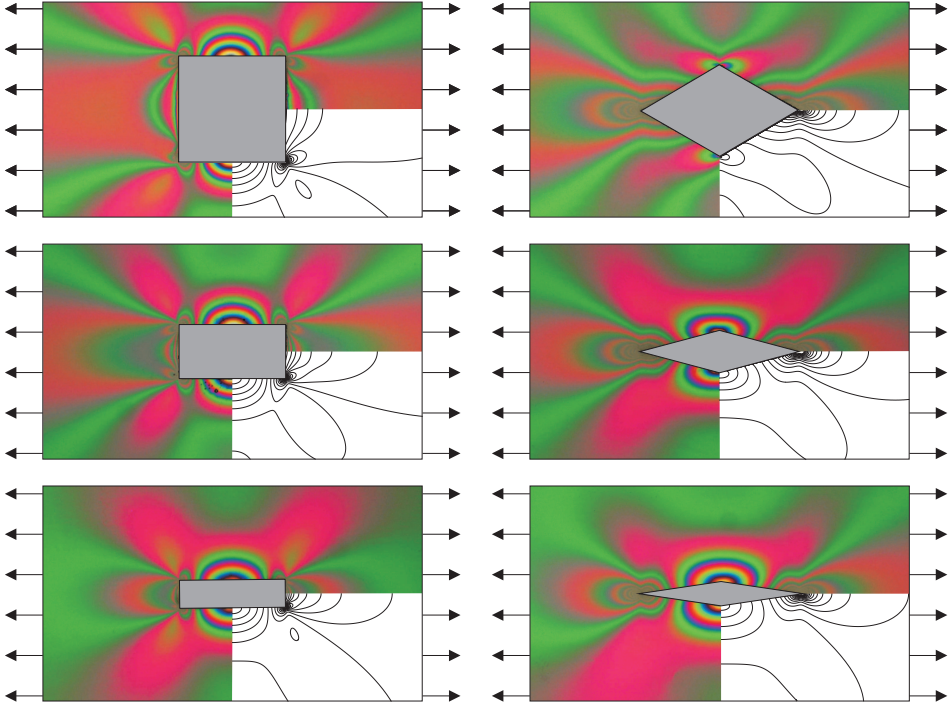


Figure 1.1: Photoelastic fringes revealing the stress field near stiff (made up of polycarbonate, Young modulus 2350 MPa) rectangular (large edge $l_1 = 20$ mm, edges aspect ratios 1, 1/2, 1/4) and rhombohedral (large axis $l_1 = 30$ mm, axis aspect ratios 2/15, 4/15, 9/15) inclusions embedded in an elastic matrix (a two-component epoxy resin, Young modulus 22 MPa, approximately 100 times less stiff than the inclusions) and loaded with uniaxial tensile stress $\sigma_{11}^\infty = 0.28$ MPa, compared to the elastic solution for rigid inclusions (in plane stress, with Poisson's ratio equal to 0.49).

In chapter 4, 5 and 6 attention is focussed in solving the generalized out-of-plane problem in the presence of a polygonal and hypocycloidal inclusion. Via binomial, generalized binomial and multinomial theorems the mechanical response under generalized out-of-plane conditions has been obtained for star-shaped cracks/stiffeners and isotoxal star-shaped polygonal inclusions (chapter 4).

The solution obtained for polygonal inclusions is exploited (chapter 5) to show that beside the usual stress singularities at the vertexes of voids or

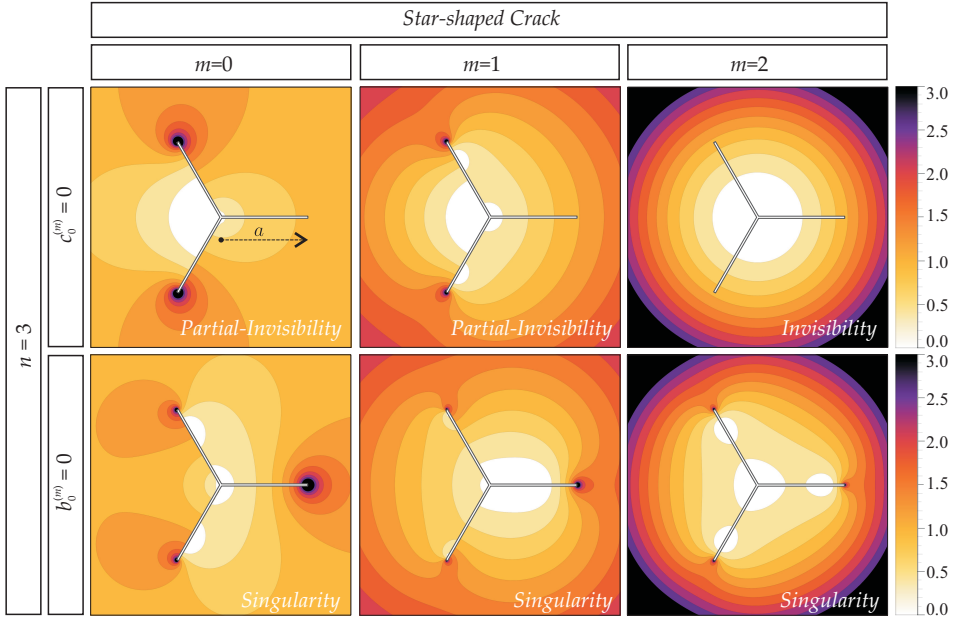


Figure 1.2: Level sets of shear stress modulus $(\tau^{(m)}(x_1, x_2)/\tau^{\infty(m)}(a, 0))$ near 3-pointed star-shaped cracks, for different orders m of the applied remote polynomial antiplane shear loading ($m = 0$ uniform, $m = 1$ linear, and $m = 2$ quadratic shear loading). Some cases of invisibility and partial-invisibility are shown; note that invisibility occurs only for certain combinations of n and m (while for the single crack invisibility is independent of m , see Fig. 5.4).

rigid inclusions, unexpected features may occur for particular geometries and loading conditions. Star-shaped cracks/stiffeners are found not only to be non-singular but even to not perturb the stress field (and therefore to be ‘invisible’), see figure 1.2. Isotoxal star-shaped polygonal inclusion corners are found to may act as stress annihilators (namely, the stress vanishes at inclusion vertex) instead of being singular, see figure 1.3.

Finally, closed-form formulae for Stress Intensity Factors and Notch Stress Intensity factors are derived for star-shaped cracks/stiffeners and for isotoxal star-shaped inclusions. In chapter 6 it is shown that the hypocycloidal-shaped inclusion cusps may act as stress reducers, a situation for which the stress at the cusp tip in presence of the inclusion is

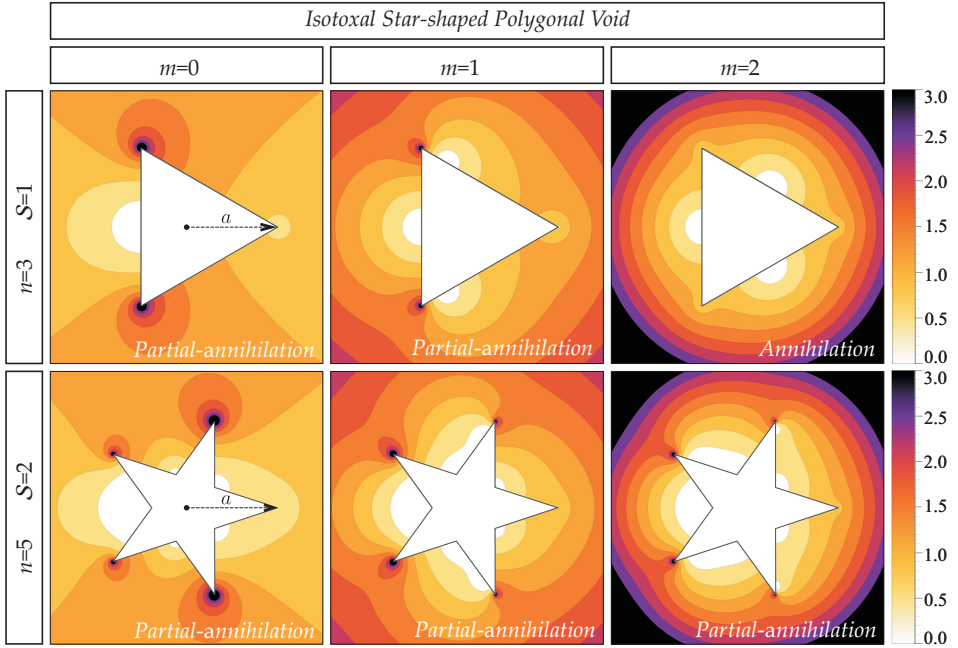


Figure 1.3: Level sets of shear stress modulus $(\tau^{(m)}(x_1, x_2)/\tau^{\infty(m)}(a, 0))$ near n -pointed isotoxal star-shaped voids, for different starriness \mathcal{S} (regular polygonal ($n=3$ and $\mathcal{S} = 1$), regular star-shaped ($n=5$ and $\mathcal{S} = 2$)) and orders m of the applied remote polynomial antiplane shear loading ($m = 0$ uniform, $m = 1$ linear, and $m = 2$ quadratic shear loading) for $c_0^{(m)} = 0$. Some cases of stress annihilation and partial-annihilation are shown, which occur only for certain combinations of n and m .

smaller than in the case when the inclusion is absent, see figure 1.4. Stress Intensity Factors for generic loading and geometry are obtained showing that a hypocycloidal inclusion can lead to a stress intensity factor higher than that corresponding to a star-shaped crack, which, as intuition suggest, usually produces a more severe stress field in the material.

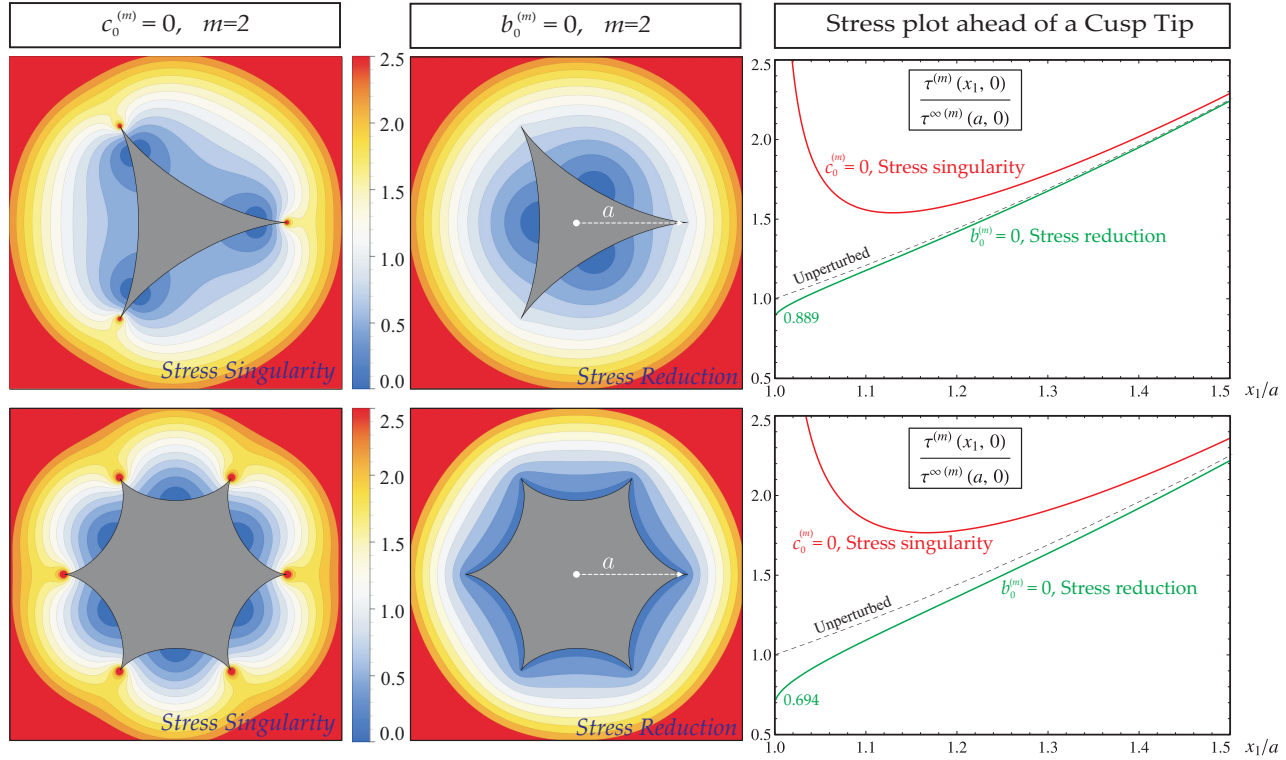


Figure 1.4: Cases of stress singularities and stress annihilation of n -cusped hypocycloidal-shaped rigid inclusions quadratic ($m = 2$) remote out-of-plane shear load ($c_0^{(m)} = 0$, left part) and ($b_0^{(m)} = 0$, central part), for different values of n are shown. Level sets of dimensionless shear stress modulus ($\tau^{(m)}(x_1, x_2)/\tau^{\infty(m)}(a, 0)$) are reported. Moreover, dimensionless shear stress modulus $\tau^{(m)}(a, 0)/\tau^{\infty(m)}(a, 0)$ ahead of the cusp tip (right part) is plotted in function of out-of-plane loading order ($m = 2$) and number of cusps ($n = 3$ and $n = 6$). Green, black, and red curves are showing the stress reduction, unperturbed stress field and the usual stress singular behaviour of the cusp, respectively.

Chapter 2

Method of analytic functions and plane elasticity

Method of analytic functions is an elegant and powerful tool to solve mechanical problems in plane elasticity. The method was originally derived by Russian researcher Kolosov (1909) and then perfected by Muskhelishvili (1953, 1963), Milne-Thomson (1960), Green and Zerna (1968), and England (1971), and is based on the reduction of the boundary value problem in elasticity to a formulation in the complex plane. The method, together with conformal mapping, is presented and used in solving in-plane and out-of-plane problems in linear elasticity.

Plane elasticity is a subcase of the general three-dimensional elasticity for which the displacement components vary only within a plane, while are unaffected by the position along the third direction, orthogonal to the considered plane. With reference to a plane containing the two Cartesian axes x_1 and x_2 , and orthogonal to the axis x_3 , the displacement components (in function of (x_1, x_2)) are expressed as

$$u_1, \quad u_2, \quad u_3. \quad (2.1)$$

The plane problem can be decomposed as the sum of an out-of-plane

problem

$$u_1 = 0, \quad u_2 = 0, \quad u_3 \neq 0, \quad (2.2)$$

while for an in-plane problem the displacement components are given by

$$u_1 \neq 0, \quad u_2 \neq 0, \quad u_3 = 0. \quad (2.3)$$

These two mechanical settings are specifically connected to the deformation and stress tensor components, in particular in out-of-plane elasticity the non-null stress and strain components (in function of (x_1, x_2)) are

$$\sigma_{13}, \quad \sigma_{23}; \quad \varepsilon_{13}, \quad \varepsilon_{23}, \quad (2.4)$$

while for and in-plane elasticity stress and strain components are given as follows

$$\sigma_{11}, \quad \sigma_{22}, \quad \sigma_{12}; \quad \varepsilon_{11}, \quad \varepsilon_{22}, \quad \varepsilon_{12}. \quad (2.5)$$

The two cases of out-of-plane problem and that of in-plane problem are treated separately in the following.

2.1 Out-of-plane problem

When out-of-plane strain conditions prevail in a linear elastic solid, the gradient of the only non-vanishing displacement component, orthogonal to the x_1 - x_2 plane and denoted by [1, 115] $u_3(x_1, x_2)$, defines the shear stress components (through the shear modulus μ) as

$$\sigma_{13}(x_1, x_2) = \mu \frac{\partial u_3(x_1, x_2)}{\partial x_1}, \quad \sigma_{23}(x_1, x_2) = \mu \frac{\partial u_3(x_1, x_2)}{\partial x_2}, \quad (2.6)$$

which are requested to satisfy the equilibrium equation in the absence of body forces,

$$\frac{\partial \sigma_{13}(x_1, x_2)}{\partial x_1} + \frac{\partial \sigma_{23}(x_1, x_2)}{\partial x_2} = 0. \quad (2.7)$$

In addition to the equilibrium equations, compatibility (or, in other words, the Schwarz theorem for function w) requires

$$\frac{\partial \sigma_{13}(x_1, x_2)}{\partial x_2} - \frac{\partial \sigma_{23}(x_1, x_2)}{\partial x_1} = 0. \quad (2.8)$$

Considering the constitutive relation (2.6), equilibrium in the absence of body-forces (2.7) can be expressed in terms of the displacement field u_3 as the Laplace equation

$$\nabla^2 u_3(x_1, x_2) = 0, \quad (2.9)$$

so that, introducing a analytic function (or a complex potential) $f(z)$, function of the complex variable $z = x_1 + i x_2$, such that

$$u_3 = \frac{1}{\mu} \operatorname{Re}[f(z)], \quad (2.10)$$

and, considering the Cauchy-Riemann conditions for analytic functions, the stress-potential relationship can be written as

$$\sigma_{13} - i \sigma_{23} = f'(z), \quad (2.11)$$

so that the out-of-plane resultant shear force $F_{\widehat{BC}}$ along an arc \widehat{BC} is

$$F_{\widehat{BC}} = \int_B^C (\sigma_{13} dx_2 - \sigma_{23} dx_1) = \operatorname{Im} [f(z_C) - f(z_B)]. \quad (2.12)$$

In addition for the antiplane problem, one eigenvalue of the stress tensor is null and the other two have opposite signs. The absolute value of the two non-null eigenvalues is

$$\tau = \sqrt{(\sigma_{13})^2 + (\sigma_{23})^2}. \quad (2.13)$$

Note that the out-of-plane problem being described by the single non-vanishing displacement u_3 , is governed by the single analytic function $f(z)$. For this reason out-of-plane problem is also known as a scalar problem in elasticity. So that the solution for the scalar problem is much simpler than that for an in-plane or vector problem in elasticity, as for the latter integral equations are involved to solve the problem.

2.2 In-plane problem

Considering the two-dimensional case, the small strains¹ in $x_1 - x_2$ plane can be expressed in terms of the displacements are given by [3, 124]

$$\varepsilon_{11} = \frac{\partial u_1}{\partial x_1}, \quad \varepsilon_{22} = \frac{\partial u_2}{\partial x_2}, \quad \varepsilon_{12} = \frac{1}{2} \left(\frac{\partial u_1}{\partial x_2} + \frac{\partial u_2}{\partial x_1} \right), \quad (2.14)$$

while the stress fields which are work-conjugate to the strain fields must satisfy the equilibrium equations (A.3) in $x_1 - x_2$ plane

$$\frac{\partial \sigma_{11}}{\partial x_1} + \frac{\partial \sigma_{12}}{\partial x_2} = 0, \quad \frac{\partial \sigma_{21}}{\partial x_1} + \frac{\partial \sigma_{22}}{\partial x_2} = 0. \quad (2.15)$$

In addition through differentiation of equations (2.14) the compatibility equations are derived as follows

$$\frac{\partial^2 \varepsilon_{11}}{\partial x_1^2} + \frac{\partial^2 \varepsilon_{22}}{\partial x_2^2} - 2 \frac{\partial^2 \varepsilon_{12}}{\partial x_1 \partial x_2} = 0, \quad (2.16)$$

further using equations (A.26) in the subsection A.2.2 the compatibility equation can also be expressed in terms of stress components:

$$\frac{\partial^2}{\partial x_2^2} (\sigma_{11} - \bar{\nu} \sigma_{22}) + \frac{\partial^2}{\partial x_1^2} (\sigma_{22} - \bar{\nu} \sigma_{11}) - 2(1 + \bar{\nu}) \frac{\partial^2 \sigma_{12}}{\partial x_1 \partial x_2} = 0, \quad (2.17)$$

where material constant $\bar{\nu}$ is modified Poisson's ratio in the case of plane strain as summed below

$$\bar{\nu} = \begin{cases} \nu & \text{for plane stress,} \\ \frac{\nu}{1 - \nu} & \text{for plane strain.} \end{cases} \quad (2.18)$$

For further details about ν , plane stress or plane strain please see subsection A.2.2.

¹For the basic equations in plane strain/stress, the reader is addressed to appendix A.

2.2.1 Airy Stress Function

The mechanical fields within a solid satisfy both the equilibrium and the compatibility equations, so that, considering the linear elastic behaviour, Airy introduced a stress function $\Phi(x_1, x_2)$ for plane problem which can be used to describe two dimensional stress fields, as

$$\sigma_{11} = \frac{\partial^2 \Phi}{\partial x_2^2}, \quad \sigma_{22} = \frac{\partial^2 \Phi}{\partial x_1^2}, \quad \sigma_{12} = -\frac{\partial^2 \Phi}{\partial x_1 \partial x_2}. \quad (2.19)$$

These equations guarantee that the two non trivial equilibrium equations (2.15) are satisfied, while compatibility condition can be expressed in terms of the Airy stress function as the following biharmonic equation [13]

$$\nabla^4 \Phi(x_1, x_2) = 0. \quad (2.20)$$

The method of analytic functions (also known as Kolosov-Muskhelishvili complex potential method) is useful in solving boundary value problems governed by equation (2.20) for which general solution can be written in terms of two unknown analytic functions (also known as complex potentials) $\varphi(z)$ and $\psi(z)$, as follows

$$\Phi(z, \bar{z}) = \text{Re} \left[\bar{z} \varphi(z) + \int \psi(z) dz \right]. \quad (2.21)$$

where $z = x_1 + i x_2$ and $\bar{z} = x_1 - i x_2$ represent a complex variable and its conjugate, respectively.

To find the $\varphi(z)$ and $\psi(z)$ certain boundary conditions must be imposed. Let us consider an infinite two-dimensional body containing a void or a rigid inclusion of a generic shape, where the body is subjected to a generic remote stress field. Herein is instrumental to define parameters Θ and χ assuming different values for void and rigid inclusion, given as

$$(\Theta; \chi) = \begin{cases} (1; 1) & \text{for void,} \\ (\kappa; -1) & \text{for rigid inclusion,} \end{cases} \quad (2.22)$$

where κ is a parameter depending on the Poisson's ratio, equation (A.29).

Two fundamental boundary conditions are imposed on the contour of the inclusion. The traction free (for a void inclusion) and displacement (for a rigid inclusion) boundary conditions can be expressed in terms of the complex potentials as

$$\Theta\varphi(z) + \chi z \overline{\varphi'(z)} + \chi \overline{\psi(z)} = (1 - \chi) i \mu \epsilon z, \quad (2.23)$$

where ϵ designate the rotational angle of the rigid inclusion induced by the remote loading. Under non-trivial conditions, this angle can be evaluated by imposing global equilibrium for the rigid inclusion, namely null resultants acting on the inclusion.

The knowledge of the complex potentials lead to full-field solution in terms of stresses and displacements in the complex plane z [11], as

$$\begin{cases} \sigma_{11} + \sigma_{22} = 4\text{Re} [\varphi'(z)], \\ \sigma_{22} - \sigma_{11} + 2i\sigma_{12} = 2 [\bar{z}\varphi''(z) + \psi'(z)], \\ u_1 + iu_2 = \frac{1}{2\mu} [\kappa\varphi(z) - z\overline{\varphi'(z)} - \overline{\psi(z)}]. \end{cases} \quad (2.24)$$

While in polar coordinates (r, θ) the relations (2.24) are modified [4] as

$$\begin{cases} \sigma_{rr} + \sigma_{\theta\theta} = 4\text{Re} [\varphi'(z)], \\ \sigma_{\theta\theta} - \sigma_{rr} + 2i\sigma_{r\theta} = 2 [\bar{z}\varphi''(z) + \psi'(z)] e^{2i\theta}, \\ u_r + iu_\theta = \frac{1}{2\mu} [\kappa\varphi(z) - z\overline{\varphi'(z)} - \overline{\psi(z)}] e^{-i\theta}, \end{cases} \quad (2.25)$$

where apexes ' and '' indicate the first and second derivatives with respect to the variable z , respectively. While $\bar{\psi}(z)$ represents the complex conjugate of the function $\psi(z)$.

2.3 Conformal mapping applied to plane elastic systems

Let's suppose to have a complex z -plane or the physical plane in which a problem is stated and let the complex ζ -plane (defined by one-to-one mapping)

$$z = \omega(\zeta), \quad \zeta = \omega^{-1}(z), \quad (2.26)$$

be a virtual plane into in which the problem is mapped [1, 11]. Let $z = x_1 + ix_2$ and $\zeta = \xi_1 + i\xi_2$ to be complex variables such that, the mapping is the relation between Cartesian (x_1, x_2) and curvilinear (ξ_1, ξ_2) coordinate system. The mapping is conformal at points where $\omega(\zeta)$ and $\omega^{-1}(z)$ are analytic and $\omega'(\zeta)$ and $(\omega^{-1}(z))'$ are nonzero. Then, the complex potentials can be written as

$$\varphi(\omega(\zeta)) = \varphi(\zeta), \quad \psi(\omega(\zeta)) = \psi(\zeta). \quad (2.27)$$

2.3.1 Out-of-plane formulae transformation into conformal plane

For an antiplane strain problem [115, 116] the complex potential

$$g(\zeta) = f(\omega(\zeta)), \quad (2.28)$$

is introduced, so that equations (2.10), (2.11) and (2.12) become

$$u_3 = \frac{1}{\mu} \text{Re}[g(\zeta)], \quad \sigma_{13} - i\sigma_{23} = \frac{g'(\zeta)}{\omega'(\zeta)}, \quad F_{\widehat{BC}} = \text{Im}[g(\zeta_B) - g(\zeta_C)]. \quad (2.29)$$

The displacement and stress fields in the physical domain can be obtained once the complex potential is known and the inclusion shape is specified.

2.3.2 In-plane formulae transformation into conformal plane

The boundary conditions (2.23) are transformed in the ζ -plane as

$$\Theta \varphi(\zeta) + \chi \frac{\omega(\zeta)}{\omega'(\zeta)} \overline{\varphi'(\zeta)} + \chi \overline{\psi(\zeta)} = (1 - \chi) i \mu \epsilon \omega(\zeta). \quad (2.30)$$

Knowing that $z = \omega(\zeta)$ and $dz = \omega'(\zeta)d\zeta$, the first and second derivative of the complex function $\varphi(z)$ are given, as follows

$$\varphi'(z) = \frac{\varphi'(\zeta)}{\omega'(\zeta)}, \quad \varphi''(z) = \frac{1}{[\omega'(\zeta)]^3} [\varphi''(\zeta)\omega'(\zeta) - \varphi'(\zeta)\omega''(\zeta)], \quad (2.31)$$

transformation of $\varphi(z)$ and $\psi(z)$ lead to the stress and displacement fields (2.24) into the following [11]

$$\begin{cases} \sigma_{11} + \sigma_{22} = 4\text{Re} \left[\frac{\varphi'(\zeta)}{\omega'(\zeta)} \right], \\ \sigma_{22} - \sigma_{11} + 2i\sigma_{12} = 2 \left[\frac{\psi'(\zeta)}{\omega'(\zeta)} + \frac{\overline{\omega(\zeta)}}{\omega'(\zeta)^3} [\varphi''(\zeta)\omega'(\zeta) - \varphi'(\zeta)\omega''(\zeta)] \right], \\ u_1 + iu_2 = \frac{1}{2\mu} \left[\kappa\varphi(\zeta) - \frac{\omega(\zeta)}{\omega'(\zeta)}\overline{\varphi'(\zeta)} - \overline{\psi(\zeta)} \right]. \end{cases} \quad (2.32)$$

2.4 Schwarz-Christoffel conformal mapping

According to Schwarz-Christoffel (SC) transformation an infinite plane containing a polygonal inclusion can be conformally mapped into an infinite exterior or finite interior region of the unit circle, see figure 2.1. Moreover a simply connected finite polygonal domain can be conformally transformed into an infinite exterior or finite interior region of the unit circle [4, 5, 11, 72]. In the following, four different ways to map a polygonal contour onto a unit circle are presented, which will be useful for the latter calculations.

2.4.1 Exterior to exterior

SC formula mapping *exterior* region of the unit circle to *exterior* region of the N -sided polygon and is given by the following equation [76]

$$\omega_{ee}(\zeta) = A \int_1^\zeta \left[\frac{1}{\sigma^2} \prod_{j=0}^{N-1} (\sigma - k_j)^{\beta_j - 1} \right] d\sigma + B, \quad (2.33)$$

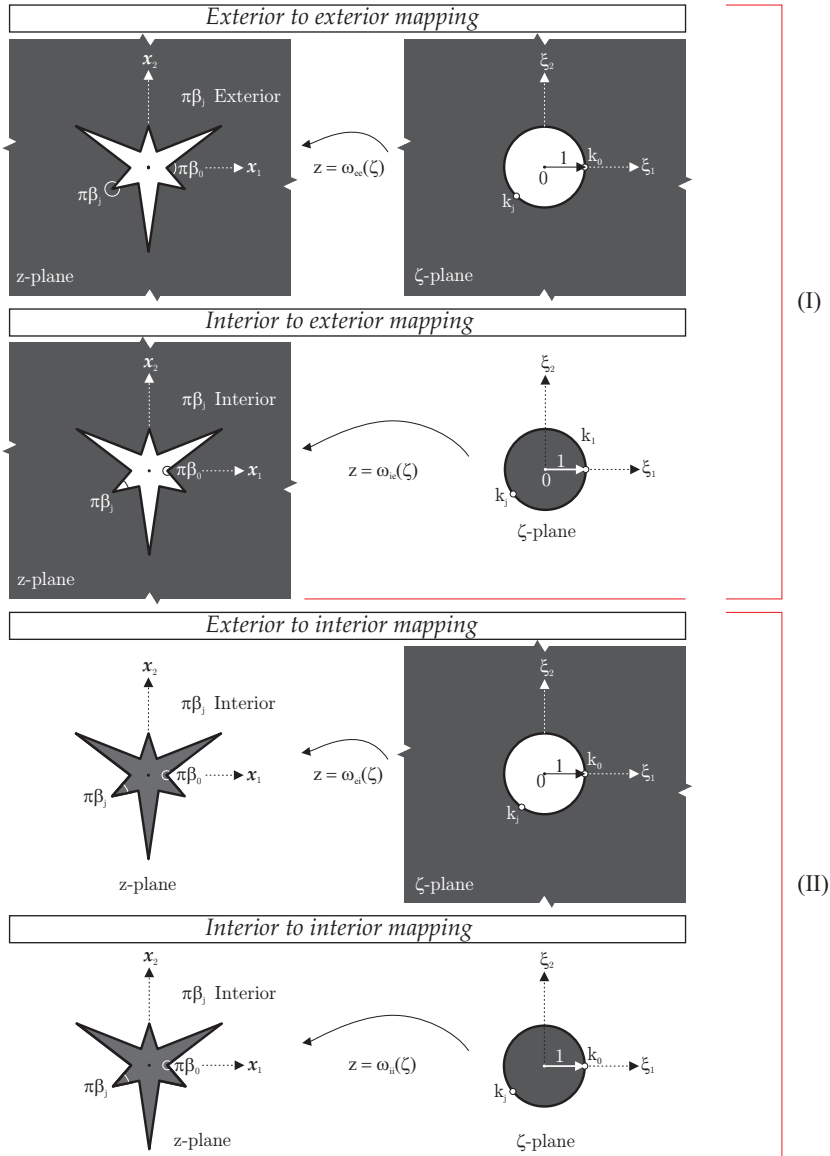


Figure 2.1: Schwarz-Christoffel transformation of an infinite plane containing a polygonal inclusion having N vertices is conformally mapped into an infinite exterior or finite interior region of the unit circle (upper part, I). A simply connected finite N -sided polygonal domain can be conformally transformed into an infinite exterior or finite interior region of the unit circle (lower part, II).

where complex constant A can be represented by

$$A = R e^{i\delta}, \quad (2.34)$$

in which R and δ represent scaling and rotation of the polygon, respectively and B denotes translation of the given polygon. In addition k_j for $(j=0, 1, \dots, N-1)$ are pre-images of j -th vertex in ζ -plane and β_j are fraction of π of the exterior angle of j -th vertex, in z -plane, both in counterclockwise order, see figure 2.1.

Noting that the sum of exterior angles² of the given N -sided polygon is

$$\sum_{j=0}^{N-1} \beta_j = N + 2. \quad (2.36)$$

taking out the integration variable σ as a common factor from the integrand of equation (2.33) one obtains

$$\omega_{ee}(\zeta) = A \int_1^\zeta \left[\frac{1}{\sigma^2} \prod_{j=0}^{N-1} \left(1 - \frac{k_j}{\sigma} \right)^{\beta_j-1} \sigma^{\beta_j-1} \right] d\sigma + B. \quad (2.37)$$

By developing the product $\prod \sigma^{\beta_j-1}$ in equation (2.37) and the knowledge of relationship in equation (2.36) lead to

$$\prod_{j=0}^{N-1} \sigma^{\beta_j-1} = \sigma^2. \quad (2.38)$$

Thus an alternative form of the SC formula (2.33) is obtained and it will be useful in the latter calculations [72], as

$$\omega_{ee}(\zeta) = A \int_1^\zeta \left[\prod_{j=0}^{N-1} \left(1 - \frac{k_j}{\sigma} \right)^{\beta_j-1} \right] d\sigma + B. \quad (2.39)$$

²While the sum of interior angles of the given N -sided polygon is given by the following expression:

$$\sum_{j=0}^{N-1} \beta_j = N - 2. \quad (2.35)$$

Note that integrands of equations (2.33) and (2.39) are not single valued in general, their branch points k_j are given by the vertices of polygon. Therefore closed form expression for the conformal map $\omega_{ee}(\zeta)$ cannot always be achieved, except for some simple geometries. So that in order to obtain approximation of $\omega_{ee}(\zeta)$ it is mandatory to perform series expansion of the integrand around ∞ . Thus the function $\omega_{ee}(\zeta)$ mapping exterior region of the unit circle to exterior region of the polygon can be expressed through Laurent series [11, 129], as

$$\omega_{ee}(\zeta) = A \left(\zeta + \sum_{j=1}^{\infty} \frac{d_j}{\zeta^j} \right) + B, \quad (2.40)$$

where d_j are complex constants obtained by integrating equation (2.33).

2.4.2 Interior to exterior

SC formula for a unit disc which maps the *interior* region of the unit disk to *exterior* region of the N -sided polygon, see figure 2.1, is given by

$$\omega_{ie}(\zeta) = A \int_1^{\zeta} \left[\frac{1}{\sigma^2} \prod_{j=0}^{N-1} \left(1 - \frac{\sigma}{k_j} \right)^{1-\beta_j} \right] d\sigma + B, \quad (2.41)$$

where β_j are fraction of π of the interior angle of j -th vertex, in z - plane.

The series expansion of the integrand of equation (2.41) around the origin of the unit disk i.e. 0. lead to the following approximation of the conformal map $\omega_{ie}(\zeta)$ mapping the interior region of the unit disk to exterior region of the polygon expressed by the Laurent's series

$$\omega_{ie}(\zeta) = A \left(\frac{1}{\zeta} + \sum_{j=1}^{\infty} d_j \zeta^j \right) + B. \quad (2.42)$$

Moreover, one can go back and forth from function $\omega_{ee}(\zeta)$ to function $\omega_{ie}(\zeta)$ using a simple trick [72] of substituting variable ζ with $1/\zeta$.

2.4.3 Exterior to interior

SC formula mapping the *exterior* region of the unit circle to *interior* region of the N -sided polygon is given as follows

$$\omega_{ei}(\zeta) = A \int_1^\zeta \left[\prod_{j=0}^{N-1} (\sigma - k_j)^{\beta_j - 1} \right] d\sigma + B. \quad (2.43)$$

where β_j are fraction of π of the interior angle of j -th vertex, in z - plane.

Approximation of the map (2.43) is obtained by performing series expansion of the integrand around ∞ . Moreover the structure of equation (2.43) is similar with half-plane formula ³.

Function $\omega_{ei}(\zeta)$ which maps exterior region of the unit disk to interior region of the polygon can be expressed by the following Laurent's series

$$\omega_{ei}(\zeta) = A \left(\frac{1}{\zeta} + \sum_{j=1}^{\infty} \frac{d_j}{\zeta^j} \right) + B. \quad (2.45)$$

where d_j are complex constants obtained by integrating equation (2.43).

2.4.4 Interior to interior

At last SC formula mapping the *interior* region of the unit disk to *interior* region of the N -sided polygon, see figure 2.1, is given by

$$\omega_{ii}(\zeta) = A \int_1^\zeta \left[\prod_{j=0}^{N-1} \left(1 - \frac{\sigma}{k_j} \right)^{\beta_j - 1} \right] d\sigma + B. \quad (2.46)$$

³Following Schwarz-Christoffel integral formula transforms interior region of the polygon onto a upper half-plane [76].

$$\omega_{uhi}(\zeta) = A \int_1^\zeta \left[\prod_{j=1}^{N-1} (\sigma - k_j)^{\beta_j - 1} \right] d\sigma + B. \quad (2.44)$$

where subscript *uhi* means transformation from upper half-plane onto interior region of the polygon.

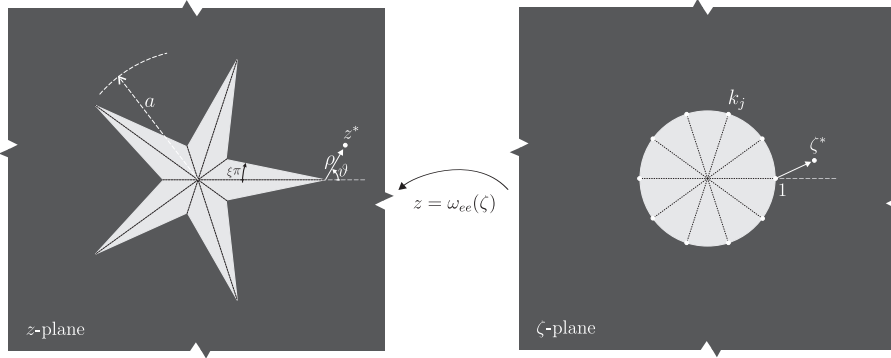


Figure 2.2: Infinite plane containing a n -pointed isotoxal star-shaped polygon inscribed in a circle of radius a . The polygon is defined by the semi-angle $\xi\pi$ at the isotoxal-points (z -plane) and is conformally mapped onto an infinite plane with a circular inclusion of unit radius (ζ -plane) using the Schwarz-Christoffel formula (2.49). Note the local reference systems $z^* = z - a$ and $\zeta^* = \zeta - 1$ defined in the two planes.

where β_j are fraction of π of the interior angle of j -th vertex, in z – plane.

The series expansion of the integrand of equation (2.46) around the origin of the unit disk i.e. 0. lead the following approximation of the conformal function $\omega_{ii}(\zeta)$ mapping the interior region of the unit disk to exterior region of the polygon expressed by the Laurent's series is given by

$$\omega_{ii}(\zeta) = A \left(\zeta + \sum_{j=1}^{\infty} d_j \zeta^j \right) + B. \quad (2.47)$$

In addition, one can go back and forth from function $\omega_{ei}(\zeta)$ to function $\omega_{ii}(\zeta)$ using a simple trick of substituting variable ζ with $1/\zeta$.

2.5 Isotoxal star-shaped polygons: exterior to exterior mapping

An isotoxal polygonal star is defined by the number N of vertices and a number $n = N/2$ of points. Note that $N \geq 4$ is always even, while $n \geq 2$

is an integer, so that a polygon (for instance a triangle, characterized by $N = 6$ and $n = 3$) is viewed as a degenerate star (for instance a three-pointed star, having $N = 6$ and $n = 3$). Introducing β_j as the fraction of the angle π measuring the j -th angle exterior to j -th vertex of the inclusion (for instance an equilateral triangle has $\beta_1 = \beta_3 = \beta_5 = 5/3$ and $\beta_0 = \beta_2 = \beta_4 = 1$), the following property (2.36) holds true

$$\sum_{j=0}^{2n-1} \beta_j = 2(n+1). \quad (2.48)$$

With reference now to a isotoxal polygonal star inclusion defined by n points, and consider that inclusion does not rotate or translate i.e. $\delta = 0$ and $B = 0$, respectively. The Schwarz-Christoffel conformal mapping (2.33) is used to map the exterior region of the inclusion (within the physical z -plane) onto the exterior region of the unit circle (within the conformal ζ -plane), namely

$$\omega_{ee}(\zeta) = a\Omega \int_1^\zeta \left[\frac{1}{\sigma^2} \prod_{j=0}^{2n-1} (\sigma - k_j)^{\beta_j-1} \right] d\sigma, \quad (2.49)$$

where constant $R = a\Omega$ with a denoting the radius of the circle inscribing the inclusion, Ω representing the scaling factor of the inclusion, k_j is the pre-image of the j -th polygon vertex in the ζ plane.

The first derivative of the conformal mapping (2.49) becomes

$$\omega'_{ee}(\zeta) = a\Omega \frac{1}{\zeta^2} \prod_{j=0}^{2n-1} (\zeta - k_j)^{\beta_j-1}. \quad (2.50)$$

Further exploiting the identity (2.48), the first derivative of the conformal mapping (2.50) can be rewritten as

$$\omega'_{ee}(\zeta) = a\Omega \prod_{j=0}^{2n-1} \left(1 - \frac{k_j}{\zeta} \right)^{\beta_j-1}. \quad (2.51)$$

With reference to a n -pointed isotoxal star polygon, see Fig. 2.2, the pre-images and the exterior angles β_j appearing in equation (2.51) are

respectively given by

$$k_j = e^{i \frac{j\pi}{n}} \quad \text{and} \quad \beta_j = \begin{cases} 2(1 - \xi) & \text{if } j \text{ is even} \\ 2(\xi + 1/n) & \text{if } j \text{ is odd} \end{cases} \quad (2.52)$$

where $j = 0, \dots, 2n - 1$ and the ξ is the fraction of π of the semi-angle at the isotoxal-points, restricted to the following set

$$\xi \in \left[0, \frac{1}{2} - \frac{1}{n}\right], \quad (2.53)$$

and that can be used to define the inclusion sharpness, starting from $\xi = 0$, which corresponds to zero-thickness (infinite sharpness) inclusion, ending with $\xi = 1/2 - 1/n$ corresponding to n -sided regular polygonal case.

From the definition (2.52)₁ of the pre-images k_j (as the complex n -th roots of the positive and negative unity), the following identities, which will become useful latter, can be derived

$$\prod_{j=0}^{n-1} (\zeta - k_{2j}) = \zeta^n - 1, \quad \prod_{j=1}^n (\zeta - k_{2j-1}) = \zeta^n + 1, \quad (2.54)$$

which can be written in an equivalent and useful form, for the future calculations, as given below

$$\prod_{j=0}^{n-1} \left(1 - \frac{k_{2j}}{\zeta}\right) = 1 - \frac{1}{\zeta^n}, \quad \prod_{j=1}^n \left(1 - \frac{k_{2j-1}}{\zeta}\right) = 1 + \frac{1}{\zeta^n}. \quad (2.55)$$

The particular case of an n -pointed star polygon is identified through the Schläfli symbol $|n/\mathcal{S}|$ involving the density, or starriness, $\mathcal{S} \in \mathbb{N}_1$, which is subject to the constraint $\mathcal{S} < n/2$, see [52, 57]. Therefore, for star polygons, the following relation

$$\xi = \frac{1}{2} - \frac{\mathcal{S}}{n}, \quad (2.56)$$

holds true, so that a regular n -sided polygon is recovered when $\mathcal{S} = 1$, see equation (2.53). Now \mathcal{S} controls the sharpness, so that the higher is \mathcal{S} ,

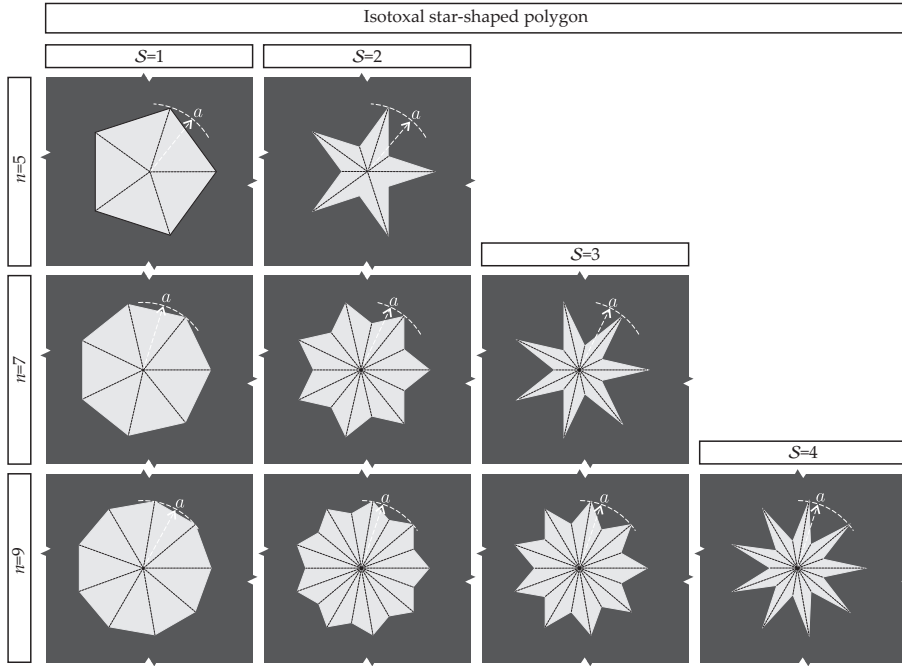


Figure 2.3: n -pointed isotoxal star-shaped polygons ($n = \{5, 7, 9\}$, from the upper part to the lower) inscribed in a circle of radius a can be used to describe inclusions in the form of n -sided regular polygons and n -pointed regular stars with density S ($= \{1, 2, 3, 4\}$, from left to right), within an infinite elastic plane. Note that, for a fixed n , the density parameter S can vary only within a finite range of natural numbers $S < n/2$.

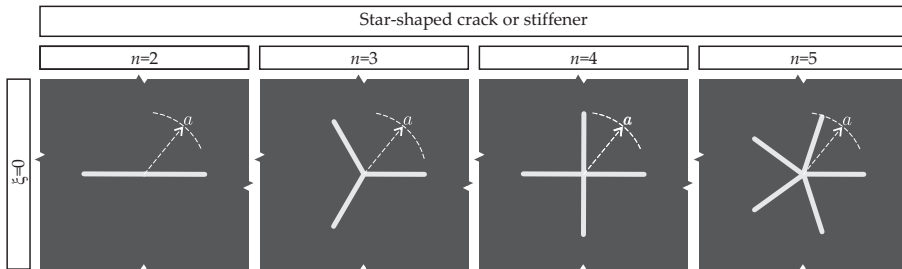


Figure 2.4: n -pointed star-shaped cracks/stiffeners, obtained in the limit of $\xi = 0$ of isotoxal star-shaped polygons.

the sharper is the star, as shown in Fig. 2.3. In the limit case $\xi = 0$ the star-shaped crack or stiffener is obtained (Fig. 2.4).

The generic conformal mapping (2.49) can be expressed through the following Laurent series (2.40)

$$\omega_{ee}(\zeta) = a\Omega \left(\zeta + \sum_{j=1}^{\infty} \frac{d_j}{\zeta^j} \right), \quad (2.57)$$

where d_j are complex constants depending on the inclusion shape.

In the following, the conformal mappings for isotoxal star polygonal voids or rigid inclusions (non-zero thickness, $\xi \neq 0$) and n -pointed star shaped cracks and stiffeners (zero-thickness, $\xi = 0$) will be obtained as special cases of the Laurent series as

$$\omega_{ee}(\zeta, \xi, n) = a\Omega(n, \xi) \sum_{j=0}^{\infty} d_{1-jn}(\xi) \zeta^{1-jn}, \quad (2.58)$$

where the scaling factor $\Omega(n, \xi)$ and the constants $d_{1-jn}(\xi)$ will be given specific expressions. It is noteworthy that ‘ jn ’ denotes the multiplication $j \times n$ between the two indices j and n .

Exploiting equation (2.54), the first derivative of the conformal mapping (2.50) for an n -pointed isotoxal star polygon (in the case of $\xi \neq 0$) is

$$\omega'_{ee}(\zeta, \xi, n) = a\Omega(n, \xi) \frac{(\zeta^n - 1)^{1-2\xi} (\zeta^n + 1)^{2(\xi + \frac{1}{n})-1}}{\zeta^2}, \quad (2.59)$$

where the scaling factor Ω is given by

$$\Omega(n, \xi) = \frac{1}{\sqrt[n]{4}} \frac{\Gamma(1 - \frac{1}{n} - \xi)}{\Gamma(\frac{n-1}{n}) \Gamma(1 - \xi)} \in \left[\frac{1}{2}, 1 \right), \quad (2.60)$$

with the symbol $\Gamma(\cdot)$ standing for Euler gamma function defined via the following convergent improper integral

$$\Gamma(u) = \int_0^{\infty} \sigma^{u-1} e^{-\sigma} d\sigma. \quad (2.61)$$

Note that the lower value of $\Omega(n, \xi)$ in equation (2.60) is attained in the line inclusion case ($n = 2$ and $\xi \rightarrow 0$), while the upper limit is given by circle limit $n \rightarrow \infty$.

Integrating equation (2.59), it is possible to write the mapping function through Appell hypergeometric function F_1 [44], as

$$\omega_{ee}(\zeta, \xi, n) = a\Omega(n, \xi) \zeta F_1 \left(-\frac{1}{n}; 2\xi - 1, 1 - 2\xi - \frac{2}{n}; 1 - \frac{1}{n}; \frac{1}{\zeta^n}, -\frac{1}{\zeta^n} \right), \quad (2.62)$$

which, since $|\zeta| \geq 1$, becomes

$$\begin{aligned} \omega_{ee}(\zeta, \xi, n) &= a\Omega(n, \xi) \sum_{v=0}^{\infty} \sum_{u=0}^{\infty} \frac{\left(-\frac{1}{n}\right)_{u+v} (-1 + 2\xi)_u \left(1 - 2\xi - \frac{2}{n}\right)_v}{\left(1 - \frac{1}{n}\right)_{u+v} u! v!} \\ &\times (-1)^v \zeta^{1-n(u+v)}, \end{aligned} \quad (2.63)$$

where, for $x \in \mathbb{R}$ and $j \in \mathbb{N}$, the symbol $(x)_j$ denotes the Pochhammer symbol expressed through the Euler gamma function, as

$$(x)_j = \frac{\Gamma(x+j)}{\Gamma(x)}. \quad (2.64)$$

Transforming the index $u + v$ of equation (2.63) into a single index leads to

$$\begin{aligned} \omega_{ee}(\zeta, \xi, n) &= a\Omega(n, \xi) \sum_{j=0}^{\infty} \sum_{k=0}^j \frac{(-1)^{j-k}}{k! (j-k)!} \\ &\times \frac{\Gamma\left(1 - \frac{2}{n} - 2\xi + j - k\right) \Gamma(-1 + 2\xi + k)}{(1 - jn) \Gamma\left(1 - \frac{2}{n} - 2\xi\right) \Gamma(-1 + 2\xi)} \zeta^{1-nj}, \end{aligned} \quad (2.65)$$

which is the Laurent series (2.58) with the complex constants $d_{1-jn}(\xi)$ identified as

$$\begin{aligned} d_{1-jn}(\xi) &= \frac{1}{1 - jn} \sum_{k=0}^j \frac{(-1)^{j-k}}{k! (j-k)!} \\ &\times \frac{\Gamma\left(1 - \frac{2}{n} - 2\xi + j - k\right) \Gamma(-1 + 2\xi + k)}{\Gamma\left(1 - \frac{2}{n} - 2\xi\right) \Gamma(-1 + 2\xi)}. \end{aligned} \quad (2.66)$$

The conformal mapping (2.65) simplifies in the following particular cases of n -pointed isotoxal star polygons.

- n -sided regular polygon (so that $\xi = 1/2 - 1/n$, with $n \geq 2$), for which the scaling factor Ω and the constants d_{1-jn} are

$$\Omega(n) = \frac{\sqrt{\pi}}{\sqrt[4]{4} \Gamma\left(\frac{1}{2} + \frac{1}{n}\right) \Gamma\left(1 - \frac{1}{n}\right)} \in \left[\frac{1}{2}, 1\right), \quad (2.67)$$

$$d_{1-jn} = \frac{\Gamma\left(j - \frac{2}{n}\right)}{j! (1 - jn) \Gamma\left(-\frac{2}{n}\right)},$$

- n -pointed regular star polygon with density $\mathcal{S} = 2$ (so that $\xi = 1/2 - 2/n$, with $n \geq 4$; for instance $n = 5$ corresponds to a non-intersecting five-point star), for which the scaling factor Ω is

$$\Omega(n) = \frac{\sin\left(\frac{\pi}{n}\right) \Gamma\left(\frac{2}{n}\right)^2}{\pi \Gamma\left(\frac{4}{n}\right)} \in \left[\frac{1}{\sqrt{2}}, 1\right), \quad (2.68)$$

and the coefficients d_{1-jn} are

$$d_{1-jn} = \frac{1}{1 - jn} \sum_{k=0}^j \frac{(-1)^{j-k} \Gamma\left(\frac{2}{n} + j - k\right) \Gamma\left(-\frac{4}{n} + k\right)}{k! (j - k)! \Gamma\left(\frac{2}{n}\right) \Gamma\left(-\frac{4}{n}\right)}. \quad (2.69)$$

2.5.1 Special cases of star-shaped cracks and stiffeners

An n -pointed star-shaped crack or a star-shaped stiffener can be obtained as the limit case of a isotoxal star polygon with an infinite sharpness i.e. $\xi = 0$, see Fig. 2.4.

Considering now a n -pointed regular star-shaped crack or rigid line inclusion and introducing $\xi = 0$ in the definition (2.52)₂, the first derivative of the conformal mapping (2.51), together with equation (2.55), simplify to

$$\omega'_{ee}(\zeta, n) = a\Omega(n) \left(1 - \frac{1}{\zeta^n}\right) \left(1 + \frac{1}{\zeta^n}\right)^{\frac{2-n}{n}}, \quad (2.70)$$

where $\Omega(n)$ is a function of the number n of star points given as

$$\Omega(n) = \frac{1}{\sqrt[4]{4}} \in \left[\frac{1}{2}, 1\right), \quad (2.71)$$

for which the lower bound is obtained for $n = 2$ (line inclusions, crack or stiffener) while the upper bound corresponds to a circle, $n \rightarrow \infty$.

From the integration of equation (2.70), the mapping function can be obtained as

$$\omega_{ee}(\zeta, n) = \frac{a}{\sqrt[n]{4}} \zeta \left(1 + \frac{1}{\zeta^n} \right)^{\frac{2}{n}}, \quad (2.72)$$

which, using the generalized binomial theorem, can be expressed as

$$\omega_{ee}(\zeta, n) = \frac{a}{\sqrt[n]{4}} \sum_{j=0}^{\infty} \left[\prod_{k=0}^{j-1} \left(\frac{2}{n} - k \right) \right] \frac{\zeta^{1-jn}}{j!}, \quad (2.73)$$

namely, the Laurent series (2.58) with the complex coefficients d_{1-jn} defined as

$$d_{1-jn} = \frac{1}{j!} \prod_{k=0}^{j-1} \left(\frac{2}{n} - k \right). \quad (2.74)$$

In the special case of a simple crack or a rigid line inclusions ($n = 2$), equation (2.72), as well as the Laurent series (2.73), reduces to the well-known conformal mapping function

$$\omega_{ee}(\zeta) = \frac{a}{2} \left(\zeta + \frac{1}{\zeta} \right). \quad (2.75)$$

2.6 Hypocycloidal inclusions: exterior to exterior mapping

In the case of hypocycloidal inclusions, see Fig. 2.5 (upper part), with a number n of cusps ($n \in \mathbb{Z}$, $n \geq 2$), the function $\omega(\zeta)$ mapping the exterior region of the inclusion (within the physical z -plane) onto the exterior region of the unit circle (within the conformal ζ -plane, Fig. 2.5, right) is given by [123]

$$\omega_{ee}(\zeta) = a\Omega \left(\zeta + \frac{1}{n-1} \zeta^{1-n} \right), \quad (2.76)$$

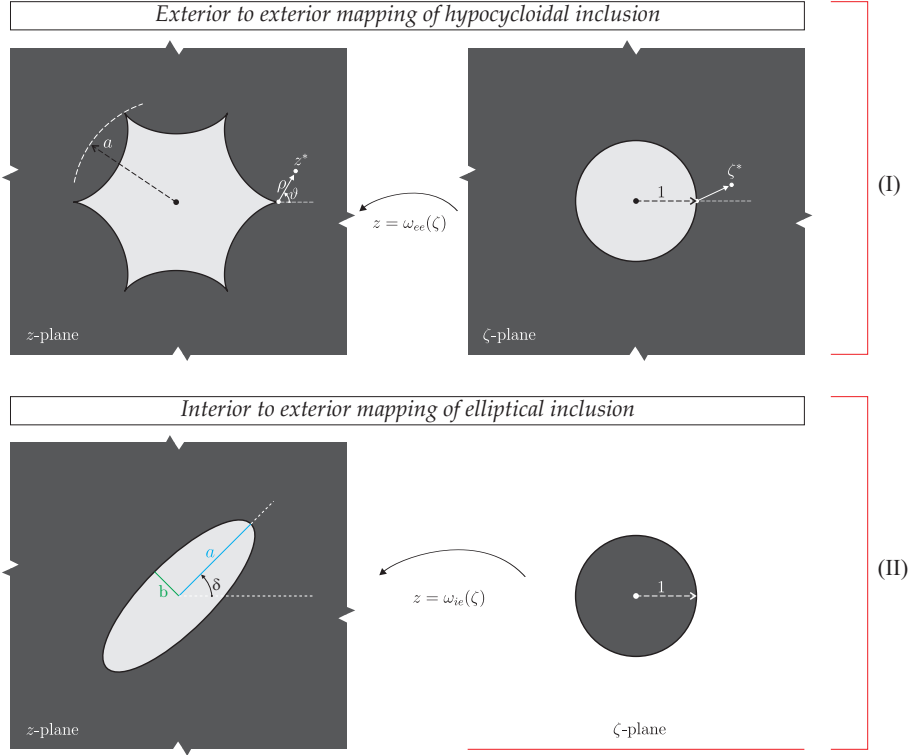


Figure 2.5: A n -cusped hypocycloid inclusion is inscribed in a circle of radius a , which is embedded in an infinite elastic plane. The conformal mapping, eq (2.77), transforms the exterior region of the hypocycloid inclusion into the exterior region of a circular inclusion of unit radius (ζ -plane). Local reference systems $z^* = z - a$ and $\zeta^* = \zeta - 1$ are introduced to define the asymptotics near the cusp with coordinates $x_1 = a$, $x_2 = 0$. Moreover an interior to exterior $\omega_{ie}(\zeta)$ (lower part, II) mapping of an elliptical inclusion is also presented.

where a is the radius of the circle inscribing the inclusion, and Ω is the scaling factor of the inclusion, function of the number n cusps,

$$\Omega(n) = \frac{n-1}{n} \in \left[\frac{1}{2}, 1 \right). \quad (2.77)$$

Note that the conformal mapping for the hypocycloidal inclusion (2.76) provides the well-known conformal mappings for line inclusion (crack or

stiffer) in the case $n = 2$ and for a circle in the limit $n \rightarrow \infty$, which are respectively given by equation (2.75) and by

$$\omega_{ee}(\zeta) = a\zeta. \quad (2.78)$$

2.7 Elliptical inclusions

Exterior region of an ellipse can be transformed into the exterior or interior region of the unit circle by the following formulae [11]

$$\omega_{ee}(\zeta) = C_1 \left(\zeta + \frac{C_2}{\zeta} \right), \quad \omega_{ie}(\zeta) = C_1 \left(\frac{1}{\zeta} + C_2 \zeta \right), \quad (2.79)$$

where constants C_1 and C_2 are given in function of geometric parameters a and b , see Fig. 2.5 (lower part), namely

$$C_1 = \frac{a+b}{2} e^{i\delta} > 0, \quad 0 \leq C_2 = \frac{a-b}{a+b} \leq 1. \quad (2.80)$$

Note that δ is the angle of rotation of the inclusion measured with respect the horizontal axes x_1 . Moreover the lower and upper bound of the parameter C_2 represents the circle of radius a and a single crack of length $2a$, respectively.

Chapter 3

Experimental validation of rigid inclusion model

Photoelasticity is employed to investigate the stress state near stiff rectangular and rhombohedral inclusions embedded in a ‘soft’ elastic plate. Results show that the singular stress field predicted by the linear elastic solution for the rigid inclusion model can be generated in reality, with great accuracy, within a material. In particular, experiments: (i.) agree with the fact that the singularity is lower for obtuse than for acute inclusion angles; (ii.) show that the singularity is stronger in Mode II than in Mode I (differently from a notch); (iii.) validate the model of rigid quadrilateral inclusion; (iv.) for thin inclusions, show the presence of boundary layers deeply influencing the stress field, so that the limit case of rigid line inclusion is obtained in strong dependence on the inclusion’s shape. The introduced experimental methodology opens the possibility of enhancing the design of thin reinforcement and of analyzing complex situations involving interaction between inclusions and defects.

3.1 Introduction

Experimental stress analysis near a crack or a void has been the subject of an intense research effort (see for instance Lim and Ravi-Chandar, 2007; 2009; Schubnel et al. 2011; Templeton et al. 2009), but the stress field near a rigid inclusion embedded in an elastic matrix, a fundamental problem

in the design of composites, has surprisingly been left almost unexplored (Theocaris, 1975; Reedy and Guess, 2001) and has *never* been investigated via photoelasticity¹.

Though the analytical determination of elastic fields around inclusions is a problem in principle solvable with existing methodologies (Movchan and Movchan, 1995; Muskhelishvili, 1953; Savin, 1961), detailed treatments are not available and the existing solutions (Chang and Conway, 1968; Evan-Iwanowski, 1956) lack mechanical interpretation, in the sense that it is not known if these predict stress fields observable in reality².

Moreover, from experimental point of view, questions arise whether the bonding between inclusion and matrix can be realized and can resist loading without detachment (which would introduce a crack) and if self-stresses can be reduced to negligible values. In this chapter we (i.) re-derive asymptotic and full-field solutions for rectangular and rhombohedral rigid inclusions (Section 3.2) and (ii.) compare these with photoelastic experiments (Section 3.3).

Photoelastic fringes obtained with a white circular polariscope are shown in Fig. 1.1 and indicate that the linear elastic solutions provide an excellent description of the elastic fields generated by inclusions up to a distance so close to the edges of the inclusions that fringes result unreadable (even with the aid of an optical microscope). By comparison of the photos shown in Fig. 1.1 with Fig. 1 of Noselli et al. (2010), it can be noted that the stress fields correctly tend to those relative to a rigid line inclusion (*stiffener*) when the aspect ratio of the inclusions grows, and that the stress fields very close to a thin inhomogeneity are substantially affected by boundary layers depending on the (rectangular or rhombohedral) shape.

¹Gdoutos (1982) reports plots of the fields that would result from photoelastic investigation of cusp inclusions, but does not report any experiment. Noselli et al. (2011) (see also Bigoni, 2012; Dal Corso et al. 2008) have only treated the case of a thin line-inclusion.

²The experimental methodology introduced here for rigid inclusions can be of interest for the experimental investigation of the interaction between inclusions and defects, such as for instance cracks, for which analytical solutions are already available (for cracks, see Piccolroaz et al. 2012 a; b; Valentini et al. 1999).

3.2 Theoretical linear elastic fields near rigid polygonal inclusions

The stress/strain fields in a linear isotropic elastic matrix containing a rigid polygonal inclusion are obtained analytically through both an asymptotic approach and a full-field determination. Considering plane stress or strain conditions, the displacement components in the $x_1 - x_2$ plane are

$$u_1 = u_1(x_1, x_2), \quad u_2 = u_2(x_1, x_2), \quad (3.1)$$

corresponding to the following in-plane deformations $\varepsilon_{\alpha\beta}$ ($\alpha, \beta = x_1, x_2$) in equations (2.14) which, for linear elastic isotropic behaviour, are related to the in the in-plane stress components $\sigma_{\alpha\beta}$ ($\alpha, \beta = x_1, x_2$) via equations (A.28). Finally, in the absence of body forces, the in-plane stresses satisfy the two non trivial equilibrium equations (2.15).

3.2.1 Asymptotic fields near the corner of a rigid wedge

Near the corner of a rigid wedge the mechanical fields may be approximated by their asymptotic expansions. With reference to the polar coordinates r, ϑ centered at the wedge corner and such that the elastic matrix occupies the region $\vartheta \in [-\alpha, \alpha]$ (while the semi-infinite rigid wedge lies in the remaining part of plane, Fig. 3.1), the Airy stress function $\Phi(r, \vartheta)$, automatically satisfying the equilibrium equation (A.3), is defined as

$$\sigma_{rr} = \frac{1}{r} \left(\Phi_{,r} + \frac{\Phi_{,\vartheta\vartheta}}{r} \right), \quad \sigma_{\vartheta\vartheta} = \Phi_{,rr}, \quad \sigma_{r\vartheta} = - \left(\frac{\Phi_{,\vartheta}}{r} \right)_{,r}. \quad (3.2)$$

The following power-law form of the Airy function satisfies the kinematic compatibility conditions [Barber, 1993, his eqn (11.35)]

$$\Phi(r, \vartheta) = r^{\gamma+2} [A_1 \cos(\gamma + 2)\vartheta + A_2 \sin(\gamma + 2)\vartheta + A_3 \cos \gamma\vartheta + A_4 \sin \gamma\vartheta], \quad (3.3)$$

and provides the in-plane stress components as

$$\begin{aligned}
\sigma_{rr} &= -(\gamma + 1)r^\gamma [A_1(\gamma + 2) \cos(\gamma + 2)\vartheta + A_2(\gamma + 2) \\
&\quad \times \sin(\gamma + 2)\vartheta + A_3(\gamma - 2) \cos \gamma\vartheta + A_4(\gamma - 2) \sin \gamma\vartheta], \\
\sigma_{\vartheta\vartheta} &= (\gamma + 2)(\gamma + 1)r^\gamma [A_1 \cos(\gamma + 2)\vartheta + A_2 \sin(\gamma + 2)\vartheta \\
&\quad + A_3 \cos \gamma\vartheta + A_4 \sin \gamma\vartheta], \\
\sigma_{r\vartheta} &= (\gamma + 1)r^\gamma [A_1(\gamma + 2) \sin(\gamma + 2)\vartheta - A_2(\gamma + 2) \\
&\quad \times \cos(\gamma + 2)\vartheta + A_3\gamma \sin \gamma\vartheta - A_4\gamma \cos \gamma\vartheta],
\end{aligned} \tag{3.4}$$

where A_1, A_2 and A_3, A_4 are unknown constants defining the symmetric (Mode I) and antisymmetric (Mode II) contributions, respectively, while γ represents the unknown power of r for the stress and strain asymptotic fields, $\{\sigma_{\alpha\beta}, \varepsilon_{\alpha\beta}\} \sim r^\gamma$, with $\gamma \geq -1/2$.

Imposing the boundary displacement conditions $u_r(r, \pm\alpha) = u_\vartheta(r, \pm\alpha) = 0$ leads to two decoupled homogeneous systems, one for each Mode symmetry condition, so that non-trivial asymptotic fields are obtained when determinant of coefficient matrix is null, namely (Seweryn and Molski, 1996)

$$\begin{aligned}
(\gamma + 1) \sin(2\alpha) - \kappa \sin(2\alpha(\gamma + 1)) &= 0, \quad \text{Mode I;} \\
(\gamma + 1) \sin(2\alpha) + \kappa \sin(2\alpha(\gamma + 1)) &= 0, \quad \text{Mode II.}
\end{aligned} \tag{3.5}$$

Note that, in the limit $\kappa = 1$ (incompressible material under plane strain conditions), equations (3.5) are the same as those obtained for a notch, except that the loading Modes are switched. Furthermore, according to the so-called ‘Dundurs correspondence’ (Dundurs, 1989), when $\kappa = -1$ eqns (3.5) coincide with those corresponding to a notch.

The smallest negative value of the power $\gamma \geq -1/2$ for each loading Mode, satisfying eqn (3.5)₁ and (3.5)₂, represents the leading order term of the asymptotic expansion. These two values (one for Mode I and another for Mode II) are reported in Fig. 3.1 (left), for different values of κ , as functions of the semi-angle α and compared with the respective values for a void wedge, Fig. 3.1 (right).

For the rigid wedge, *similarly to the notch problem*:

- the singularity appears only when $\alpha > \pi/2$ and increases with the increase of α ;

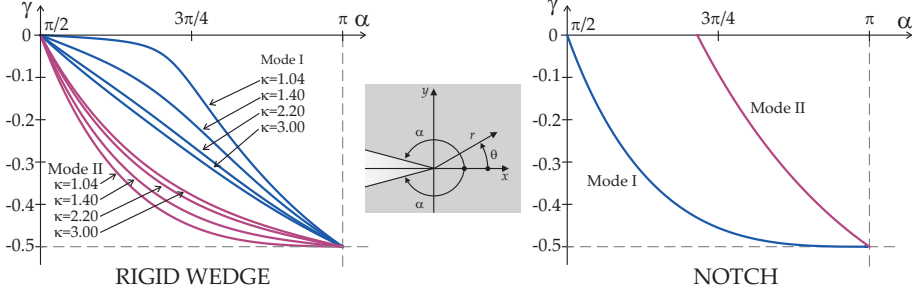


Figure 3.1: The higher singularity power γ for a rigid wedge (left, angle α is the semi-angle in the matrix enclosing the wedge) and for a notch (right, angle α is the semi-angle in the matrix enclosing the notch) under Mode I and Mode II loading and different values of κ .

- a square root singularity ($\sigma_{\alpha\beta} \sim 1/\sqrt{r}$) appears for both mode I and II when α approaches π (corresponding to the rigid line inclusion model, see Noselli et al. 2010);

while, *differently from the notch problem*:

- the singularity depends on the Poisson's ratio ν through the parameter κ ;
- the singularity under Mode II condition is stronger than that under Mode I; in particular, a weak singularity is developed under Mode I when, for plane strain deformation, a quasi-incompressible material (ν close to $1/2$) contains a rigid wedge with $\alpha \in [\frac{1}{2}, \frac{3}{4}]\pi$.

Since the intensity of singularity near a corner is strongly affected by the value of the angle α , it follows that the stress field close to a rectangular inclusion is substantially different to that close to a rhombohedral one. Therefore, strongly different boundary layers arise when a rectangular or a rhombohedral inclusion approaches the limit of line inclusion.

3.2.2 Full-field solution for a matrix containing a polygonal rigid inclusion

Solutions in 2D isotropic elasticity can be obtained using the method of complex potentials (Muskhelishvili, 1953), where the generic point (x_1, x_2)

is referred to the complex variable $z = x_1 + i x_2$ (where i is the imaginary unit) and the mechanical fields are given in terms of complex potentials $\varphi(z)$ and $\psi(z)$ which can be computed from the boundary conditions.

In the case of non-circular inclusions, it is instrumental to introduce the complex variable ζ , related to the physical plane through $z = \omega(\zeta)$ with the conformal mapping function ω (such that the inclusion boundary becomes a unit circle in the ζ -plane, $\zeta = e^{i\theta}$), so that the stress and displacement components are given by equations (2.32). The complex potentials are the sum of the unperturbed (homogeneous) solution and the perturbed (introduced by the inclusion) solution, so that, considering boundary conditions at infinity of constant stress at infinity with the only non-null component σ_{xx}^∞ , we may write

$$\varphi(\zeta) = \frac{\sigma_{11}^\infty}{4} \omega_{ie}(\zeta) + \varphi^{(p)}(\zeta), \quad \psi(\zeta) = -\frac{\sigma_{11}^\infty}{2} \omega_{ie}(\zeta) + \psi^{(p)}(\zeta), \quad (3.6)$$

where the perturbed potentials $\varphi^{(p)}(\zeta)$ and $\psi^{(p)}(\zeta)$ can be obtained by imposing the conditions (2.30) (with $\epsilon = 0$ due to the symmetry of the problem) on the inclusion boundary, which are defined on a unit circle and for a rigid inclusion³ ($\chi = -1$ and $\Theta = \kappa$) are

$$\kappa \varphi^{(p)}(\zeta) - \frac{\omega_{ie}(\zeta)}{\omega'_{ie}(\zeta)} \overline{\varphi^{(p)'}(\zeta)} - \overline{\psi^{(p)}(\zeta)} = \frac{\sigma_{11}^\infty}{2} \left(\frac{1-\kappa}{2} \omega_{ie}(\zeta) - \overline{\omega_{ie}(\zeta)} \right),$$

for $\zeta = e^{i\theta}$, $\theta \in [0, 2\pi]$.
(3.7)

In the case of n -polygonal shape inclusions the conformal mapping $\omega_{ie}(\zeta)$ which maps the interior of the unit disk onto the region exterior to the inclusion is given by the Schwarz-Christoffel integral (2.41). Assuming that the perturbed potentials are holomorphic inside the unit circle in the ζ -plane, $\varphi^{(p)}(\zeta)$ can be expressed through Laurent series

$$\varphi^{(p)}(\zeta) = R \sigma_{11}^\infty \sum_{j=1}^{\infty} a_j \zeta^j, \quad (3.8)$$

where a_j ($j=1,2,3,\dots$) are unknown complex constants. Furthermore, since the integral expression in eqn (2.41) cannot be computed as closed form

³ equation (3.7) holds when rigid-body displacements are excluded.

for generic polygon, it is expedient to represent the conformal mapping (2.42), considering $B = \delta = 0$ and $A = R$.

In order to obtain an approximation for the solution, the series expansions for $\omega_{ie}(\zeta)$ and $\varphi^{(p)}(\zeta)$ are truncated at the M -th term. Through Cauchy integral theorem (B.14), integration over the inclusion boundary of eqn (3.7) yields a linear system for the M unknown complex constants a_j , functions of the M constants d_j , obtained through series expansion of eqn. (2.41). Once the expression for $\varphi^{(p)}(\zeta)$ is obtained, the integral over the inclusion boundary of the conjugate version of the boundary condition (3.7) is used to approximate $\psi^{(p)}(\zeta)$, resulting as

$$\psi^{(p)}(\zeta) = R \sigma_{11}^{\infty} \zeta \left[\left(\sum_{j=1}^{M+2} b_j \zeta^{j-1} \right) / \left(\sum_{j=1}^{M+2} c_j \zeta^{j-1} \right) \right]. \quad (3.9)$$

Rectangle In this case the angle fractions are $\beta_j = 1/2$ ($j=1, \dots, 4$) while the pre-images are

$$k_1 = e^{\eta\pi i}, \quad k_2 = e^{-\eta\pi i}, \quad k_3 = e^{(1+\eta)\pi i}, \quad k_4 = e^{(1-\eta)\pi i}, \quad (3.10)$$

where η (likewise R) is a parameter function of the rectangle aspect ratio l_2/l_1 , with the inclusion edges l_1 and l_2 . Parameters η and R are given in Tab. 3.2.2 for the aspect ratios considered here.

l_2/l_1	1	1/2	1/4
η	0.2500	0.2003	0.1548
R/l_1	0.5902	0.4374	0.3539

Table 3.1: Parameters η and R for the considered aspect ratios l_2/l_1 of rectangular rigid inclusions.

The conformal mapping function and perturbed potentials obtained in

the case of rectangle with $l_2/l_1 = 1/4$ are reported for $M=15$:

$$\begin{aligned}
 \omega_{ie}(\zeta) &= R \left(\frac{1}{\zeta} + 0.5633\zeta - 0.1138\zeta^3 - 0.0385\zeta^5 - 0.0071\zeta^7 \right. \\
 &\quad \left. + 0.0042\zeta^9 + 0.0052\zeta^{11} + 0.0022\zeta^{13} - .0006\zeta^{15} \right), \\
 \varphi^{(p)}(\zeta) &= R \sigma_{11}^{\infty} \left(-0.2420\zeta - 0.0264\zeta^3 - 0.0071\zeta^5 + 0.0003\zeta^7 \right. \\
 &\quad \left. + 0.0020\zeta^9 + 0.0012\zeta^{11} + 0.0002\zeta^{13} - 0.0001\zeta^{15} \right), \\
 \psi^{(p)}(\zeta) &= R \sigma_{11}^{\infty} \left(-2.4454\zeta - 54.9115\zeta^3 + 6.4081\zeta^5 + 5.5545\zeta^7 \right. \\
 &\quad \left. + 3.4073\zeta^9 + 0.6051\zeta^{11} - 1.3007\zeta^{13} - 1.0545\zeta^{15} \right. \\
 &\quad \left. + 0.2727\zeta^{17} \right) / \left(109.8986 - 61.9012\zeta^2 + 37.5162\zeta^4 \right. \\
 &\quad \left. + 21.1312\zeta^6 + 5.4989\zeta^8 - 4.1163\zeta^{10} - 6.2272\zeta^{12} \right. \\
 &\quad \left. - 3.1597\zeta^{14} + \zeta^{16} \right). \tag{3.11}
 \end{aligned}$$

Rhombus In this case the pre-images are

$$k_1 = 1, \quad k_2 = i, \quad k_3 = -1, \quad k_4 = -i, \tag{3.12}$$

while the angle fractions are

$$\beta_1 = \beta_3 = \frac{2}{\pi} \arctan(l_2/l_1), \quad \beta_2 = \beta_4 = 1 - \beta_1. \tag{3.13}$$

The scaling parameter R is reported in Tab. 3.2.2 for the rhombus aspect ratios l_2/l_1 considered here, where l_1 and l_2 are the inclusion axis.

The conformal mapping function and perturbed potentials obtained in the case of rhombus with $l_2/l_1 = 2/15$ are reported for $M=15$:

l_2/l_1	9/15	4/15	2/15
R/l_1	0.3389	0.2841	0.2659

Table 3.2: Parameter R for the considered aspect ratios l_2/l_1 of rhombohedral rigid inclusions.

$$\begin{aligned}
\omega_{ie}(\zeta) &= R \left(\frac{1}{\zeta} + 0.8312\zeta + 0.0515\zeta^3 - 0.0086\zeta^5 + 0.0068\zeta^7 \right. \\
&\quad \left. - 0.0028\zeta^9 + 0.0025\zeta^{11} - 0.0013\zeta^{13} + 0.0013\zeta^{15} \right), \\
\varphi^{(p)}(\zeta) &= R \sigma_{11}^{\infty} \left(-0.1628\zeta + 0.0071\zeta^3 + 0.0001\zeta^5 + 0.0009\zeta^7 \right. \\
&\quad \left. + 0.0001\zeta^9 + 0.0003\zeta^{11} + 0.0001\zeta^{13} + 0.0002\zeta^{15} \right), \\
\psi^{(p)}(\zeta) &= R \sigma_{11}^{\infty} \left(8.1122\zeta + 28.1115\zeta^3 + 1.8150\zeta^5 - 0.6928\zeta^7 \right. \\
&\quad \left. + 0.4105\zeta^9 - 0.4451\zeta^{11} + 0.1665\zeta^{13} - 0.3417\zeta^{15} \right. \\
&\quad \left. + 0.2727\zeta^{17} \right) / \left(-53.0727 + 44.1156\zeta^2 + 8.2012\zeta^4 \right. \\
&\quad \left. - 2.2724\zeta^6 + 2.5225\zeta^8 - 1.3283\zeta^{10} + 1.4453\zeta^{12} \right. \\
&\quad \left. - 0.9307\zeta^{14} + \zeta^{16} \right). \tag{3.14}
\end{aligned}$$

3.3 Photoelastic elastic fields near rigid polygonal inclusions

Photoelastic experiments with linear and circular polariscope (with quarterwave retarders for 560nm) at white and monochromatic light⁴

⁴ The polariscope (dark field arrangement and equipped with a white and sodium vapor lightbox at $\lambda = 589.3\text{nm}$, purchased from Tiedemann & Betz) has been designed by us and manufactured at the University of Trento, see <http://ssmg.unitn.it/> for a

have been performed on twelve two-component resin (Translux D180 from Axon; mixing ratio by weight: hardener 95, resin 100, accelerator 1.5; the elastic modulus of the resulting matrix has been measured by us to be 22 MPa, while the Poisson's ratio has been indirectly estimated equal to 0.49) samples containing stiff inclusions, obtained with a solid polycarbonate 3 mm thick sheet (clear 2099 Makrolon UV) from Bayer with elastic modulus equal to 2350 MPa, approximatively 100 times stiffer than the matrix.

Samples have been prepared by pouring the resin (after deaeration, obtained through a 30 minutes exposition at a pressure of -1 bar) into a teflon mold (340 mm \times 120 mm \times 10 mm) to obtain 3 ± 0.05 mm thick samples. The resin has been kept for 36 hours at constant temperature of 29 °C and humidity of 48%. After mold extraction, samples have been cut to be 320 mm \times 110 mm \times 3 mm, containing rectangular inclusions with wedges 20 mm \times {20; 10; 5} mm and rhombohedral inclusions with axis 30 mm \times {18; 8; 4} mm.

Photos have been taken with a Nikon D200 digital camera, equipped with a AF-S micro Nikkor (105 mm, 1:2.8G ED) lens and with a AF-S micro Nikkor (70180 mm, 1:4.55.6 D) lens for details. Monitoring with a thermocouple connected to a Xplorer GLX Pasco[®], temperature near the samples during experiments has been found to lie around 22.5° C, without sensible oscillations. Near-tip fringes have been captured with a Nikon SMZ800 stereozoom microscope equipped with Nikon Plan Apo 0.5x objective and a Nikon DS-Fi1 high-definition color camera head.

The uniaxial stress experiments have been performed at controlled vertical load applied in discrete steps, increasing from 0 to a maximum load of 90 N, except for thin rectangular and rhombohedral inclusions, where the maximum load has been 70 N and 78 N, respectively (loads have been reduced for thin inclusions to prevent failure at the vertex tips). In all cases an additional load of 3.4N has been applied, corresponding to the grasp weight, so that maximum nominal far-field stress of 0.28 MPa has been applied (0.22 MPa and 0.25 MPa for the thin inclusions).

Data have been acquired after 5 minutes from the load application time in order to damp down the largest amount of viscous deformation, noticed as a settlement of the fringes, which follows displacement stabilization.

detailed description of the apparatus.

Releasing the applied load after the maximum amount, all the samples at rest showed no perceivably residual stresses in the whole specimen.

Comparison between analytical solutions and experiments is possible through matching of the isochromatic fringe order N , which (in linear photoelasticity)⁵ is given by (Frocht, 1965)

$$N = \frac{t}{f_\sigma} \Delta\sigma, \quad (3.15)$$

where t is the sample thickness, $\Delta\sigma = \sigma_I - \sigma_{II}$ is the in-plane principal stress difference, and f_σ is the material fringe constant, measured by us to be equal to 0.203 N/mm (using the so-called ‘Tardy compensation procedure’, see Dally and Riley, 1965). These comparisons are reported in Figs. 3.2 and 3.3, where the full-field solution obtained in Section 3.2.2 has been used under plane stress assumption and $\nu = 0.49$. This assumption is consistent with the reduced thickness of the employed samples, much thinner than the thickness of the samples employed by Noselli et al. (2010), who have compared photoelastic experiments considering plane strain.

The results show an excellent agreement between theoretical predictions and photoelastic measures, with some discrepancies near the contact with the inclusions where, the plane stress assumption becomes questionable due to the out-of-plane constraint imposed by the contact with the rigid phase. Moreover, some microscopical view (at 31.5 \times) near the vertices of inclusion, shown in the insets of Figs. 3.2 and 3.3, reveals that the stress fields are in good agreement even close to the corners, where a strong stress magnification is evidenced near acute corners, while no singularity is observed near obtuse corners.

The near-corner stress magnifications and comparisons with the full field solution (evaluated with $M = 15$) are provided in Fig. 3.4, where the in-plane stress difference (divided by the far field stress) is plotted along the major axis of the thin and thick rhombohedral inclusions (Fig. 3.4, upper and central parts, respectively) and along a line tangent to the corner (and inclined at an angle $\pi/6$) of the rectangular thin inclusion. In particular, magnification factors of 5.3 (upper part, $\alpha = 23\pi/24$), 3.8

⁵ Differently from Noselli et al. (2010), a constant value for the fringe material parameter f_σ has been considered here since non constant values were found not to introduce significant improvements.

(central part, $\alpha = 5\pi/6$), and 2.7 (lower part, $\alpha = 3\pi/4$) have been measured.

It is interesting to note that according to the theoretical prediction (Section 3.2.1, Fig. 3.1), the singularity is stronger for acute than for obtuse inclusion's angles and that the stress fields tend to those corresponding to a zero-thickness rigid inclusion (a 'stiffener', see Noselli et al. 2010), when the rectangular (Fig. 3.2) and the rhombohedral (Fig. 3.3) inclusions become narrow (from the upper part to the lower part of the figures).

According to results shown in Fig. 3.1, we observe from Figs. 3.2, 3.3, and 3.4 the following.

- For Mode I loading the stress concentration becomes weak for angles α within $[\pi/2, 3\pi/4]$, see Fig. 3.3 (compare the fields near the two different vertices).
- For Mode II loading the stress concentration is much stronger than for Mode I. Stress concentrations generated for mixed-mode at an angle $\alpha = 3\pi/4$ are visible in Fig. 3.2 near the corners of rectangular inclusions. These concentrations are visibly stronger than those near the wider corner in Fig. 3.3 (upper part), which is subject to Mode I;
- The stress fields evidence boundary layers close to the inhomogeneity, see lower part of Figs. 3.2 and 3.3: These boundary layers are crucial in defining detachment mechanisms and failure modes. Therefore, the shape of a thin inclusion has an evident impact in limiting the working stress of a mechanical piece in which it is embedded. This conclusion has implications in the design of material with thin and stiff reinforcements, which can be enhanced through an optimization of the inclusion shape.

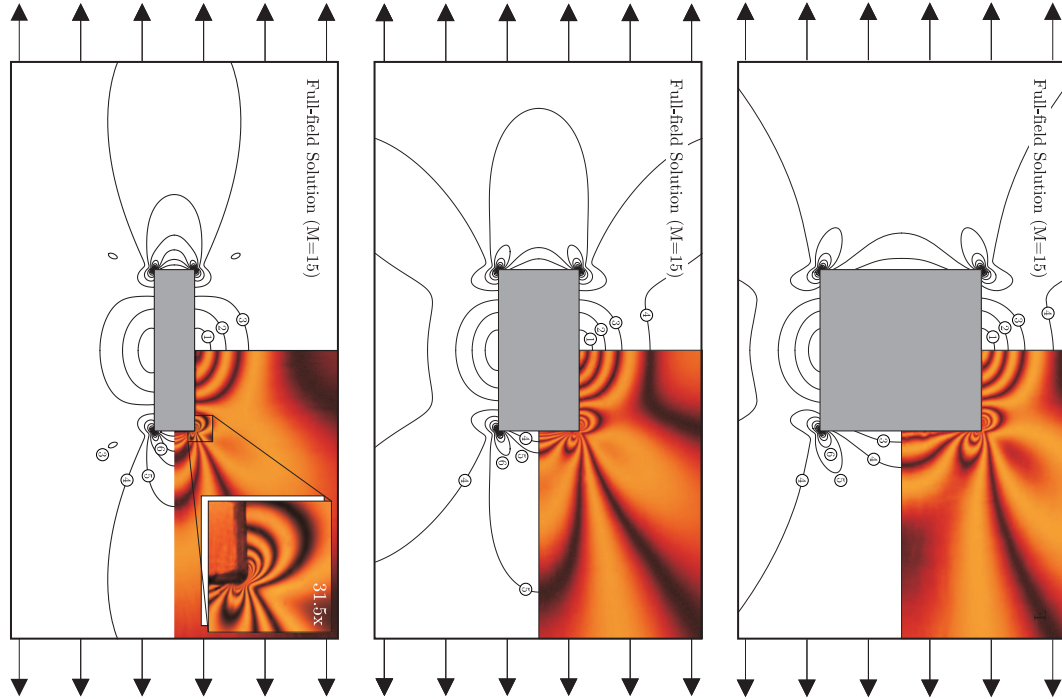


Figure 3.2: Monochromatic photoelastic fringes (with order number enclosed in a circle) revealing the in-plane principal stress difference field near stiff rectangular inclusions (made up of polycarbonate, with large edge $l_1 = 20$ mm and aspect ratios $\{1; 1/2; 1/4\}$) embedded in an elastic matrix (a two-component ‘soft’ epoxy resin, approximately 100 times less stiff than the inclusion) compared to the elastic solution for rigid inclusions (in plane stress, with Poisson’s ratio equal to 0.49), at uniaxial stress $\sigma_{11}^\infty = 0.28$ MPa (0.22 MPa for the lower part).

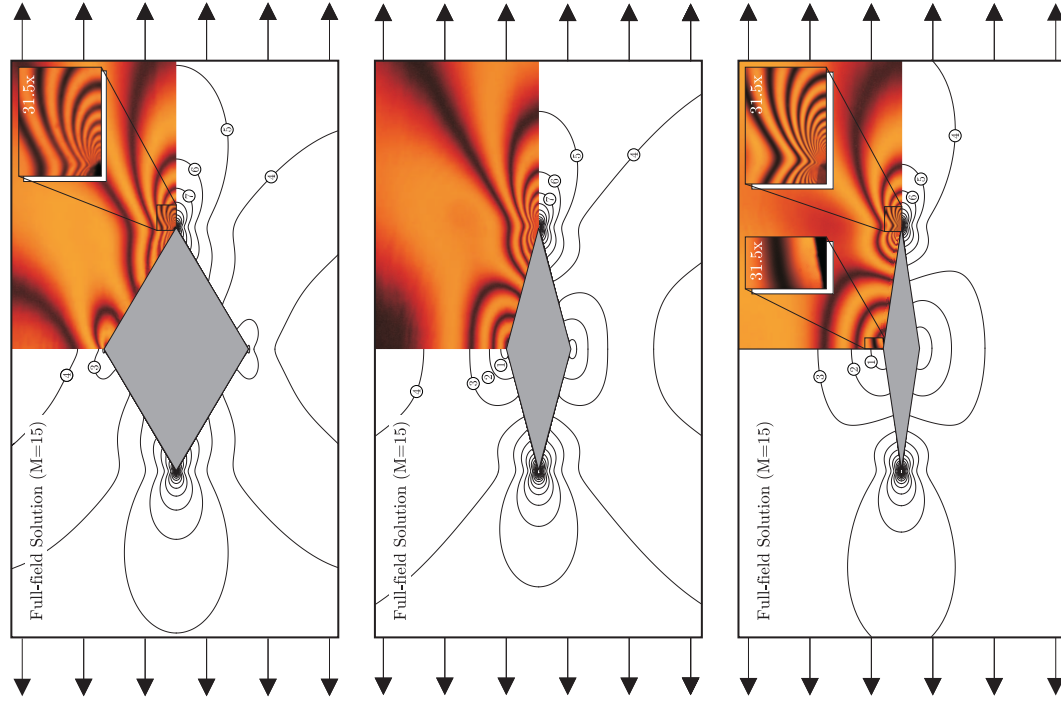


Figure 3.3: Monochromatic photoelastic fringes (with order number enclosed in a circle) revealing the in-plane principal stress difference field near stiff rhombohedral inclusions (made up of polycarbonate, with large axes 30 mm and axis aspect ratios $\{9/15; 4/15; 2/15\}$) embedded in an elastic matrix (a two-component ‘soft’ epoxy resin, approximately 100 times less stiff than the inclusion) compared to the elastic solution for rigid inclusions (in plane stress, with Poisson’s ratio equal to 0.49), at uniaxial stress $\sigma_{11}^{\infty} = 0.28$ MPa (0.25 MPa for the lower part).

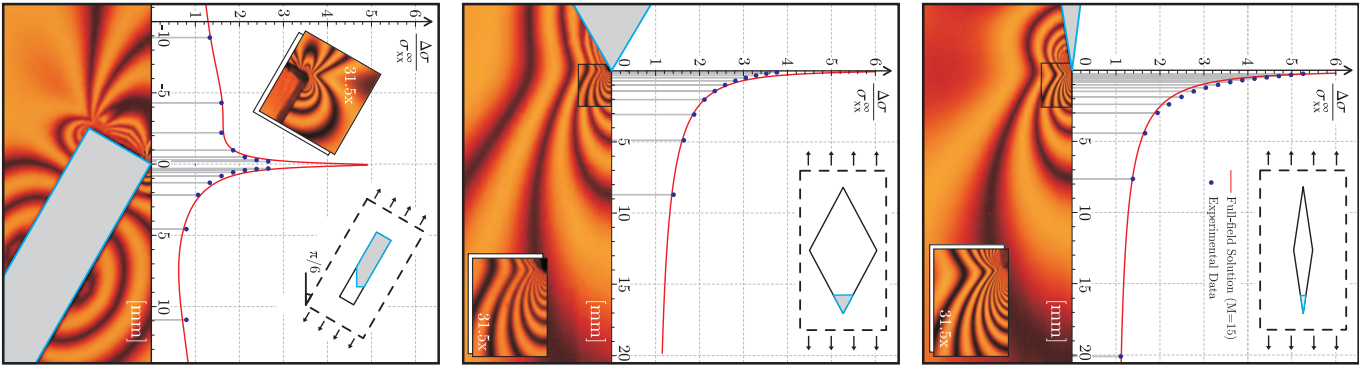


Figure 3.4: Near-corner stress magnification (in-plane stress difference divided by the far field stress) for rhombohedral (upper and central parts, respectively $\alpha = 23\pi/24$ and $\alpha = 5\pi/6$) and rectangular (lower part, $\alpha = 3\pi/4$) rigid inclusions. Experimental results are compared with the full-field elastic solution, evaluated with $M = 15$. Magnification factors of 5.3 (upper part), 3.8 (central part), and 2.7 (lower part) are visible.

Chapter 4

Formulation and analytical solution for nonuniform out-of-plane problem

An infinite class of nonuniform antiplane shear fields is considered for a linear elastic isotropic space and (non-intersecting) isotoxal star-shaped polygonal voids and rigid inclusions perturbing these fields are solved. Through the use of the complex potential technique together with the generalized binomial and the multinomial theorems, full-field closed-form solutions are obtained in the conformal plane. The particular (and important) cases of star-shaped cracks and rigid-line inclusions (stiffeners) are also derived. Except for special cases (addressed in Part II), the obtained solutions show singularities at the inclusion corners and at the crack and stiffener ends, where the stress blows-up to infinity, and is therefore detrimental to strength. It is for this reason that the closed-form determination of the stress field near a sharp inclusion or void is crucial for the design of ultra-resistant composites.

4.1 Introduction

The investigation of the perturbation induced by an inclusion (a void, or a crack, or a stiff insert) in an ambient stress field loading a linear elastic infinite space is a fundamental problem in solid mechanics, whose

importance need not be emphasized. Usually this problem is analyzed with respect to uniform ambient stress fields [11, 43, 107, 54, 128, 110], although inhomogeneous, self-equilibrated stresses have also been considered [106, 47, 53, 139, 73, 78, 141]. The interplay between stress inhomogeneities and singularities generated at inclusion corners is important in the design of ultra-resistant composites, as stress singularities are known to be detrimental to strength. In fact, an extreme stress concentration, leading to material failure, has been shown by experiments to represent the counterpart of the mathematical concept of singularity [124, 131, ?]. The determination of the conditions leading to stress relief around inclusions may introduce new perspectives in the development of composite materials.

The present article addresses the analytical, closed-form solution of isotaxal star-shaped polygonal voids and rigid inclusions in an elastic isotropic matrix loaded by inhomogeneous (but self-equilibrated) antiplane shear fields (which are introduced as polynomial in an explicit mechanical setting). The solution is obtained using the complex potential technique, with conformal mapping [11, 128, 129], which leads to a full-field determination of the stress field. The particular cases of infinitely thin star corners are also addressed, corresponding to star-shaped cracks and stiffeners (the latter also referred to as rigid-line inclusions). These patterns of multiple cracks are quite common, as three and four point star-shaped cracks are induced by triangular and Vickers pyramidal indenters [50, 51, 109] and can emerge during drying of colloidal suspensions in capillary tubes [55, 58]. Multiple radial crack patterns are generated after low speed impacts¹ on brittle plates [77]. In Section 4.2, using the multinomial (and the generalized binomial) theorem, the full-field closed-form solutions for isotaxal star-shaped polygonal voids and rigid inclusions (and for star-shaped cracks and stiffeners) perturbing an inhomogeneous antiplane shear field are obtained, after the problem is posed and solved in its asymptotic form in Section 2.1. These results open the way to issues related to inclusion neutrality and in particular allows the discovery of ‘quasi-static invisibility’ and ‘stress annihilations’, whose treatment is deferred to Part II of this study [116], together with considerations of irregularities in the shape of the inclusions and the finiteness of the domain containing the inclusion.

¹High speed generates circumferential fractures in addition to radial.

The presented results, obtained in out-of-plane elasticity, provide also a solution for problems in thermal conductivity and electrostatics, due to the common governing equations expressed by the Laplacian.

4.1.1 An infinite class of antiplane shear fields

A class of remote anti-plane loadings is considered for an infinite elastic solid containing an inclusion, as defined by the following polynomial stress field of m -th order ($m \in \mathbb{N}$)

$$\sigma_{13}^{\infty(m)}(x_1, x_2) = \sum_{j=0}^m b_j^{(m)} x_1^{m-j} x_2^j, \quad \sigma_{23}^{\infty(m)}(x_1, x_2) = \sum_{j=0}^m c_j^{(m)} x_1^{m-j} x_2^j, \quad (4.1)$$

where $b_j^{(m)}$ and $c_j^{(m)}$ are constants ($j = 0, \dots, m$). Because the polynomial stress field (4.1) has to satisfy both the equilibrium equation (2.7) and the compatibility equation (2.8), all the constants $b_j^{(m)}$ and $c_j^{(m)}$ are linearly dependent on $b_0^{(m)}$ and $c_0^{(m)}$ as follows

$$\begin{aligned} & \forall \text{ even } j \in [0; m] \\ & b_j^{(m)} = (-1)^{\frac{j}{2}} \frac{m!}{j!(m-j)!} b_0^{(m)}, \quad c_j^{(m)} = (-1)^{\frac{j}{2}} \frac{m!}{j!(m-j)!} c_0^{(m)}, \\ & \forall \text{ odd } j \in [0; m] \\ & b_j^{(m)} = (-1)^{\frac{j-1}{2}} \frac{m!}{j!(m-j)!} c_0^{(m)}, \quad c_j^{(m)} = (-1)^{\frac{j+1}{2}} \frac{m!}{j!(m-j)!} b_0^{(m)}. \end{aligned} \quad (4.2)$$

Note that the constants $b_0^{(m)}$ and $c_0^{(m)}$ represent a measure of the remote (or, in the inclusion problem, the ‘unperturbed’) stress state along the x_1 axis,

$$\sigma_{13}^{\infty(m)}(x_1, 0) = b_0^{(m)} x_1^m, \quad \sigma_{23}^{\infty(m)}(x_1, 0) = c_0^{(m)} x_1^m, \quad (4.3)$$

so that $b_0^{(0)}$ and $c_0^{(0)}$ are the loading constants defining the usual uniform Mode III, Fig. 4.1 (upper part),

$$\sigma_{13}^{\infty(0)}(x_1, 0) = b_0^{(0)}, \quad \sigma_{23}^{\infty(0)}(x_1, 0) = c_0^{(0)}. \quad (4.4)$$

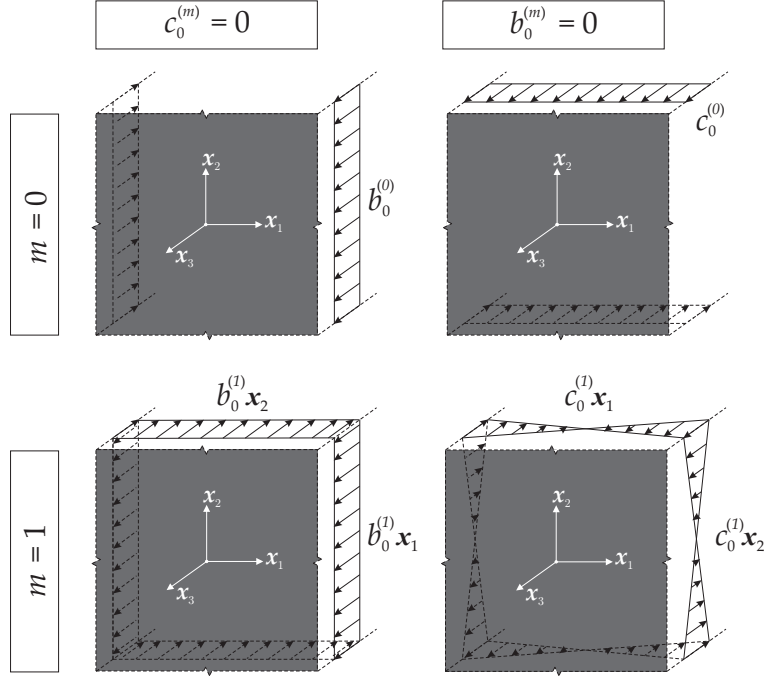


Figure 4.1: The cases of uniform ($m = 0$, upper part) and linear ($m = 1$, lower part) remote (self-equilibrated) loading conditions described by the constant $b_0^{(m)}$ (left) and $c_0^{(m)}$ (right), eqn (4.1).

With the only exception of the case $m = 0$, the two remote shear stress components are affected by both constants $b_0^{(m)}$ and $c_0^{(m)}$. For example, in the case of linear remote loading ($m=1$), Fig. 4.1 (lower part), the remote field is defined by

$$\sigma_{13}^{\infty(1)}(x_1, x_2) = b_0^{(1)}x_1 + c_0^{(1)}x_2, \quad \sigma_{23}^{\infty(1)}(x_1, x_2) = c_0^{(1)}x_1 - b_0^{(1)}x_2. \quad (4.5)$$

Note that the introduced polynomial fields can be used to reconstruct through series a general self-equilibrated remote loading. Therefore, due to the superposition principle, the solution obtained in the next sections also describes the mechanical fields under general Mode III remote loadings.

It is instrumental to express the polynomial stress field (4.1) in two further reference systems, one Cartesian and the other polar. In particular,

with reference to a \hat{x}_1 - \hat{x}_2 Cartesian coordinate system obtained through a rotation of an angle γ of a x_1 - x_2 system, the polynomial stress field can be expressed as

$$\hat{\sigma}_{13}^{\infty(m)}(\hat{x}_1, \hat{x}_2) = \sum_{j=0}^m \hat{b}_j^{(m)} \hat{x}_1^{m-j} \hat{x}_2^j, \quad \hat{\sigma}_{23}^{\infty(m)}(\hat{x}_1, \hat{x}_2) = \sum_{j=0}^m \hat{c}_j^{(m)} \hat{x}_1^{m-j} \hat{x}_2^j, \quad (4.6)$$

where the loading constants $\hat{b}_0^{(m)}$ and $\hat{c}_0^{(m)}$ are linearly dependent on the constants $b_0^{(m)}$ and $c_0^{(m)}$ as follows

$$\begin{aligned} \hat{b}_0^{(m)} &= b_0^{(m)} \cos((m+1)\gamma) + c_0^{(m)} \sin((m+1)\gamma), \\ \hat{c}_0^{(m)} &= c_0^{(m)} \cos((m+1)\gamma) - b_0^{(m)} \sin((m+1)\gamma). \end{aligned} \quad (4.7)$$

With reference to a polar coordinate system (r, θ) centered at the origin of the x_1 - x_2 axes, the polynomial stress field (4.1) can be rewritten as

$$\begin{cases} \sigma_{r3}^{\infty(m)}(r, \theta) &= r^m \left[b_0^{(m)} \cos((m+1)\theta) + c_0^{(m)} \sin((m+1)\theta) \right], \\ \sigma_{\theta 3}^{\infty(m)}(r, \theta) &= r^m \left[c_0^{(m)} \cos((m+1)\theta) - b_0^{(m)} \sin((m+1)\theta) \right], \end{cases} \quad (4.8)$$

corresponding to the displacement

$$u_3^{\infty(m)}(r, \theta) = \frac{r^{m+1}}{\mu(m+1)} \left[b_0^{(m)} \cos((m+1)\theta) + c_0^{(m)} \sin((m+1)\theta) \right]. \quad (4.9)$$

Finally, it can be noted that the modulus of the principal stress (2.13) is independent of the circumferential angle θ

$$\tau^{\infty(m)}(r) = r^m \sqrt{\left[b_0^{(m)} \right]^2 + \left[c_0^{(m)} \right]^2}, \quad (4.10)$$

so that the level sets of the modulus of the (unperturbed) shear stress are concentric circles centered at the origin of the axes.

4.1.2 Asymptotic expansion near the vertex of a void or a rigid inclusion

A vertex of a void or a rigid inclusion is considered (defined by the semi-angle α exterior to the inclusion, Fig. 4.2, right), with reference to a polar coordinate system (ρ, ϑ) centered at the inclusion corner, where $\vartheta \in (-\alpha, \alpha)$ measures the angle from the symmetry axis. Following [66]–[70], the solution of the general out-of-plane problem can be decomposed in its symmetric $u_3^S(\rho, \vartheta) = u_3^S(\rho, -\vartheta)$ and antisymmetric $u_3^A(\rho, \vartheta) = -u_3^A(\rho, -\vartheta)$ terms,

$$u_3(\rho, \vartheta) = u_3^S(\rho, \vartheta) + u_3^A(\rho, \vartheta), \quad (4.11)$$

which, considering equations (2.6)–(2.8), assume the following expressions in polar coordinates,

$$\begin{aligned} u_3^S(\rho, \vartheta) &= D^S \rho^{1+\lambda^S} \cos [(1 + \lambda^S) \vartheta], \\ u_3^A(\rho, \vartheta) &= D^A \rho^{1+\lambda^A} \sin [(1 + \lambda^A) \vartheta], \end{aligned} \quad (4.12)$$

and, through the isotropic elastic constitutive relation (2.6), the following stress field representations are obtained as

$$\begin{aligned} \sigma_{\rho 3}^S(\rho, \vartheta) &= \mu D^S (1 + \lambda^S) \rho^{\lambda^S} \cos [(1 + \lambda^S) \vartheta], \\ \sigma_{\vartheta 3}^S(\rho, \vartheta) &= -\mu D^S (1 + \lambda^S) \rho^{\lambda^S} \sin [(1 + \lambda^S) \vartheta], \\ \sigma_{\rho 3}^A(\rho, \vartheta) &= \mu D^A (1 + \lambda^A) \rho^{\lambda^A} \sin [(1 + \lambda^A) \vartheta], \\ \sigma_{\vartheta 3}^A(\rho, \vartheta) &= \mu D^A (1 + \lambda^A) \rho^{\lambda^A} \cos [(1 + \lambda^A) \vartheta], \end{aligned} \quad (4.13)$$

where D^S and D^A are constants (to be defined in relation to the remote loading), while λ^S and λ^A are the eigenvalues of the characteristic equations for the symmetric and antisymmetric problem, respectively, with $\{\lambda^S, \lambda^A\} > -1$, to satisfy the requirement of finiteness of the local elastic strain energy. These eigenvalues can be defined through the boundary condition imposed at the inclusion boundary and are crucial to the asymptotic description of stress fields around the inclusion vertex.

The apexes \star and \star will be used to distinguish between values assigned to voids and to rigid inclusions, respectively. The null traction or null displacement boundary conditions at $\theta = \pm\alpha$, holding respectively for the former and the latter problem, can be expressed as [75]

$$\sigma_{\theta 3}^{\star}(\rho, \pm\alpha) = 0, \quad u_3^{\star}(\rho, \pm\alpha) = 0, \quad (4.14)$$

leading to the following characteristic equations

$$\begin{aligned} \sin[\alpha(1 + \lambda^{\star S})] = 0, \quad \cos[\alpha(1 + \lambda^{\star A})] = 0, \\ \cos[\alpha(1 + \lambda^{\star S})] = 0, \quad \sin[\alpha(1 + \lambda^{\star A})] = 0, \end{aligned} \quad j \in \mathbb{N}, \quad (4.15)$$

and from which two countably infinite set of eigenvalues $\lambda_j^{\star A}$, $\lambda_j^{\star A}$, $\lambda_j^{\star S}$ and $\lambda_j^{\star S}$ are obtained as

$$\begin{cases} \lambda_j^{\star S}(\alpha) = \lambda_j^{\star A}(\alpha) = -1 + \frac{j\pi}{\alpha}, \\ \lambda_j^{\star A}(\alpha) = \lambda_j^{\star S}(\alpha) = -1 + \frac{(2j-1)\pi}{2\alpha}, \end{cases} \quad j \in \mathbb{N}. \quad (4.16)$$

The mechanical fields at small distances from the inclusion are ruled by the leading-order term in the symmetric and antisymmetric asymptotic expansions (4.12), which correspond to $j = 1$

$$\begin{cases} \lambda_1^{\star S}(\alpha) = \lambda_1^{\star A}(\alpha) = -1 + \frac{\pi}{\alpha} \geq 0, \\ \lambda_1^{\star A}(\alpha) = \lambda_1^{\star S}(\alpha) = -1 + \frac{\pi}{2\alpha} \geq -\frac{1}{2}, \end{cases} \quad (4.17)$$

and are reported in Fig. 4.2 (left) as a function of exterior semi-angle α . Note that the following property holds true

$$\lambda_1^{\star S}(\alpha) = \lambda_1^{\star A}(\alpha) > \lambda_1^{\star A}(\alpha) = \lambda_1^{\star S}(\alpha). \quad (4.18)$$

The range of variation of the values λ_1 for different values of the exterior semi-angle α is summarized in Tab. 1 and reported in Fig. 4.2 (left), from which it can be noted that the stress field has:

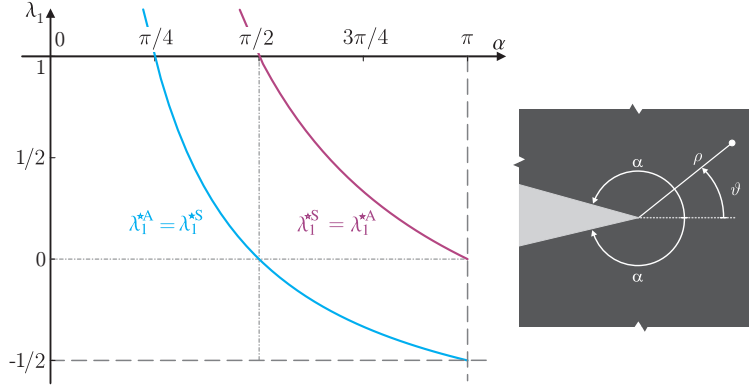


Figure 4.2: (left) First eigenvalue λ_1 , guiding the leading-order term in the asymptotic description of symmetric and antisymmetric parts of mechanical fields (4.12) in the neighborhood of the inclusion vertex, as a function of the semi-angle α exterior to the inclusion (right).

- a singular leading-order term for antisymmetric notch/symmetric wedge problems when $\alpha \in (\pi/2, \pi]$ (in particular a square-root singularity is attained for $\alpha = \pi$, corresponding to antisymmetric crack/symmetric stiffener problems);
- a constant (zeroth-order) term for antisymmetric notch/symmetric wedge problems when $\alpha = \pi/2$ and for symmetric notch/antisymmetric wedge problems when $\alpha = \pi$. Such a constant is usually called T-stress in in-plane and S-stress in out-of-plane [56, 127, 137] crack problems;
- a non-singular leading-order term for symmetric notch/antisymmetric wedge problems when $\alpha < \pi$ and for antisymmetric notch/symmetric wedge problems when $\alpha < \pi/2$.

The above-listed observations are crucial for the understanding of the occurrence of stress singularity or of stress annihilation at the vertices of polygonal void and rigid inclusions, as shown in Part II.

α	$\in \left(0, \frac{\pi}{2}\right)$	$\frac{\pi}{2}$	$\in \left(\frac{\pi}{2}, \pi\right)$	π
$\lambda_1^{*S}(\alpha) = \lambda_1^{\star A}(\alpha)$	> 1	1	$\in (0, 1)$	0
$\lambda_1^{*A}(\alpha) = \lambda_1^{\star S}(\alpha)$	> 0	0	$\in \left(-\frac{1}{2}, 0\right)$	$-\frac{1}{2}$

Table 4.1: Ranges of the first eigenvalue λ_1 , defining the leading-order term in the description of symmetric and antisymmetric parts of the displacement field u_3 , eqn (4.12)₁, for different ranges of exterior semi-angle α (Fig 4.2, right).

4.2 Full-field solution

The full-field solution for non-intersecting isotoxal star polygonal voids and rigid inclusions embedded in an isotropic elastic material subject to the generalized anti-plane remote polynomial stress field (4.1) is solved through the complex potential technique generalizing the solution obtained in [122]. The out-of-plane problem formulation is presented in section 2.1 in which the Laplace equation (2.9) governing the problem, a single analytic function $f(z)$ (2.10), the stress-potential relationship (2.11) and the out-of-plane resultant shear force (2.12) are reported.

The complex potential $f(z)$ can be considered as the sum of the unperturbed potential $f^\infty(z)$, which is the solution in the absence of the inclusion, and the perturbed one, $f^p(z)$, introduced to recover the boundary condition along the inclusion boundary,

$$f(z) = f^\infty(z) + f^p(z). \quad (4.19)$$

Using the polynomial description (4.1) for the self-equilibrated remote stress field $\sigma_{13}^{\infty(m)}$ and $\sigma_{23}^{\infty(m)}$, the unperturbed potential is given as

$$f^\infty(z, m) = T^{(m)} z^{m+1}, \quad (4.20)$$

where

$$T^{(m)} = \frac{b_0^{(m)} - i c_0^{(m)}}{m + 1}, \quad (4.21)$$

which in the particular case of uniform antiplane shear load, $m = 0$, reduces to [122] (their equation (20)).

Considering now the presence of the inclusion, it is instrumental to define the conformal mapping $z = \omega(\zeta)$, which transforms the boundary of the inclusion in the physical plane into a circle of unit radius within the conformal plane. Also the mechanical fields (2.29) reported in the subsection 2.3.1 are transformed into the conformal plane.

Isotoxal star-shaped polygonal voids and rigid inclusions are considered, see Fig. 2.2 (left), embedded in an infinite elastic matrix. In the following subsections, solution for star-shaped crack or stiffener and isotoxal star-shaped polygonal inclusion is derived separately.

4.2.1 Closed-form solution for star-shaped cracks or stiffeners

To derive the complex potential (2.28) for star-shaped cracks and stiffeners, it is instrumental to introduce t and q , functions of m and n as

$$t = \frac{2(m + 1)}{n}, \quad q = \left\lfloor \frac{m + 1}{n} \right\rfloor, \quad (4.22)$$

where the dependence on m and n is omitted for simplicity and the symbol $\lfloor \cdot \rfloor$ stands for the integer part of the relevant argument. By means of the generalized binomial theorem, equations (4.20) and (2.72), help us to obtain the unperturbed potential which can be expressed as

$$g^\infty(\zeta, n, m) = \frac{a^{m+1} T^{(m)}}{2^t} \sum_{j=0}^{\infty} \left(\prod_{l=0}^{j-1} t - l \right) \frac{\zeta^{m+1-jn}}{j!}. \quad (4.23)$$

By imposing the null traction resultant condition $F_{BC}^{\widehat{}} = 0$ for a crack ($\chi = 1$), or the rigid-body displacement condition $u_{3B} = u_{3C}$ for a rigid line inclusion ($\chi = -1$), for every pairs of points B and C along the boundary of the unit circle in the conformal plane, the perturbed complex

potential $g^p(m)$ is obtained as

$$g^p(\zeta, n, m) = \frac{a^{m+1}}{2^t} \left\{ \overline{\chi T^{(m)}} \left[-\frac{\delta_{m+1,qn}}{q!} \prod_{l=0}^{q-1} (t-l) \right. \right. \\ \left. \left. + \sum_{j=0}^q \left(\prod_{l=0}^{j-1} (t-l) \right) \frac{1}{j! \zeta^{m+1-jn}} \right] \right. \\ \left. - T^{(m)} \sum_{j=q+1}^{\infty} \left(\prod_{l=0}^{j-1} (t-l) \right) \frac{1}{j! \zeta^{jn-m-1}} \right\}, \quad (4.24)$$

where $\delta_{m+1,qn}$ is Kronecker delta, so that ‘ qn ’ is a single index corresponding to the multiplication $q \times n$ between the two indices q and n .

The complex potential follows from the sum of the perturbed and unperturbed potentials as

$$g(\zeta, n, m) = \frac{a^{m+1}}{2^t} \left\{ -\frac{\overline{\chi T^{(m)}}}{q!} \delta_{m+1,qn} \prod_{l=0}^{q-1} (t-l) \right. \\ \left. + \sum_{j=0}^q \frac{1}{j!} \left(\prod_{l=0}^{j-1} (t-l) \right) \left[T^{(m)} \zeta^{m+1-jn} + \frac{\overline{\chi T^{(m)}}}{\zeta^{m+1-jn}} \right] \right\}. \quad (4.25)$$

Note that in the particular case when $t = 2(m+1)/n \in \mathbb{N}$, the binomial theorem can be exploited and the complex potentials (6.1), (4.24) and (4.25) reduce to

$$g^\infty(\zeta, n, m) = \frac{a^{m+1} T^{(m)}}{2^t} \sum_{j=0}^t \frac{t!}{j! (t-j)!} \zeta^{m+1-nj}, \quad (4.26a)$$

$$g^p(\zeta, n, m) = \frac{a^{m+1} \left(\overline{\chi T^{(m)}} - T^{(m)} \right)}{2^t} \left[-\frac{t!}{q! q!} \delta_{m+1,qn} \right. \\ \left. + \sum_{j=0}^q \frac{t!}{j! (t-j)!} \frac{1}{\zeta^{m+1-jn}} \right], \quad (4.26b)$$

$$g(\zeta, n, m) = \frac{a^{m+1}}{2^t} \left[-\frac{t!}{q! q!} \chi \overline{T^{(m)}} \delta_{m+1, 2q} + \sum_{j=0}^q \frac{t!}{j! (t-j)!} \left(T^{(m)} \zeta^{m+1-nj} + \frac{\chi \overline{T^{(m)}}}{\zeta^{m+1-nj}} \right) \right]. \quad (4.26c)$$

In addition to the particular case (4.26), the complex potential (4.25) also simplifies in some other special cases, which are listed below.

- $n > m + 1$ (corresponding to the case $q = 0$)

$$g(\zeta, n, m) = \frac{a^{m+1}}{2^t} \left[T^{(m)} \zeta^{m+1} + \frac{\chi \overline{T^{(m)}}}{\zeta^{m+1}} \right], \quad (4.27)$$

a simple expression representing an infinite set of solutions, such as that for a cruciform crack ($n = 4$, Fig. 2.4) subject to uniform, linear and quadratic remote antiplane shear loads ($m = 0, 1, 2$);

- $n = 2$ (corresponding to the case of line stiffener or crack)

$$g(\zeta, n, m) = \frac{(m+1)! a^{m+1}}{2^{m+1}} \left[-\frac{\chi \overline{T^{(m)}}}{q! q!} \delta_{m+1, 2q} + \sum_{j=0}^q \frac{T^{(m)} \zeta^{m+1-2j} + \frac{\chi \overline{T^{(m)}}}{\zeta^{m+1-2j}}}{j! (m+1-j)!} \right]; \quad (4.28)$$

- $m = 0$ (corresponding to the case of uniform antiplane shear [140])

$$g(\zeta, n) = \frac{a}{\sqrt[n]{4}} \left[T^{(0)} \zeta + \frac{\chi \overline{T^{(0)}}}{\zeta} \right], \quad (4.29)$$

where the constant $T^{(0)}$ and its complex conjugate $\overline{T^{(0)}}$ represent the remote uniform antiplane shear loading given by the equation (4.21).

4.2.2 Closed-form solution for isotoxal star-shaped polygonal inclusions

Considering the Laurent series of the mapping function (2.58) for the case $\xi \neq 0$ with the coefficients (2.66) to represent the unperturbed stress (4.8), the corresponding unperturbed complex potential in the conformal plane can be obtained through the multinomial theorem [65] as

$$g^\infty(\zeta, \xi, n, m) = (a\Omega(n, \xi))^{m+1} T^{(m)} \sum_{j=0}^{\infty} L_{m+1-jn} \zeta^{m+1-jn}, \quad (4.30)$$

where the coefficients L_{m+1-jn} are given in the form

$$L_{m+1-jn} = \sum_{\mathcal{C}_j(l_0, l_1, \dots, l_\infty)} \binom{m+1}{l_0, l_1, \dots, l_\infty} \prod_{k=0}^{\infty} (d_{1-kn})^{l_k}, \quad (4.31)$$

with $\mathcal{C}_j(l_0, l_1, \dots, l_\infty)$ representing the double conditions applied on the sum, as

$$\mathcal{C}_j(l_0, l_1, \dots, l_\infty) : \left\{ \sum_{k=0}^{\infty} l_k = m+1 \quad \cap \quad \sum_{k=1}^{\infty} k l_k = j \right\}, \quad (4.32)$$

where $l_k \in \mathbb{N}$. Note that the symbol in brackets in equation (4.31) represents the multinomial coefficient defined through the factorial function, as

$$\binom{m+1}{l_0, l_1, \dots, l_\infty} = \frac{(m+1)!}{l_0! l_1! \dots l_\infty!}. \quad (4.33)$$

Introduction of the boundary conditions expressing either null traction along the boundary of the star-shaped void ($\chi = 1$) or allowing only for a rigid body-displacement of the rigid inclusion along its boundary ($\chi = -1$), the perturbed complex potential $g^{p(m)}(\zeta, \xi, n)$ is obtained as

$$g^p(\zeta, \xi, n, m) = (a\Omega(n, \xi))^{m+1} \left[\overline{\chi T^{(m)}} \left(-L_{m+1-qn} \delta_{m+1,qn} + \sum_{j=0}^q \frac{L_{m+1-jn}}{\zeta^{m+1-jn}} \right) - T^{(m)} \sum_{j=q+1}^{\infty} \frac{L_{m+1-jn}}{\zeta^{jn-m-1}} \right], \quad (4.34)$$

so that the complex potential, solution of the isotoxal star-shaped polygonal voids and rigid inclusions, follows in a closed-form solution

$$g(\zeta, \xi, n, m) = (a\Omega(n, \xi))^{m+1} \left[-\chi \overline{T^{(m)}} L_{m+1-qn} \delta_{m+1,qn} + \sum_{j=0}^q L_{m+1-jn} \left(T^{(m)} \zeta^{m+1-jn} + \frac{\chi \overline{T^{(m)}}}{\zeta^{m+1-jn}} \right) \right], \quad (4.35)$$

as the sum of a finite number of terms.

Note that the complex potential (4.35) displays a rigid-body motion component for both the rigid inclusion and the void when $q = (m + 1)/n$. Furthermore, the complex potential (4.35) simplifies in the following particular cases

- $n > m + 1$ (equivalent to $q = 0$),

$$g(\zeta, \xi, n, m) = (a\Omega(n, \xi))^{m+1} \left[T^{(m)} \zeta^{m+1} + \frac{\chi \overline{T^{(m)}}}{\zeta^{m+1}} \right]. \quad (4.36)$$

This case embraces an infinite set of solutions, for instance a 5-pointed isotoxal star subject to uniform, linear, quadratic and cubic remote antiplane shear load ($m = 0, 1, 2, 3$);

- $m = 0$ (remote uniform antiplane shear)

$$g(\zeta, \xi, n) = a\Omega(n, \xi) \left[T^{(0)} \zeta + \frac{\chi \overline{T^{(0)}}}{\zeta} \right], \quad (4.37)$$

corresponding to the solution for regular polygonal inclusions [122]).

4.2.3 Shear stress analogies between rigid inclusions and voids

The purpose of this section is to highlight some special cases in which the stress fields generated within a matrix by a rigid inclusion are analogous to those generated when a void (of the same shape) is present.

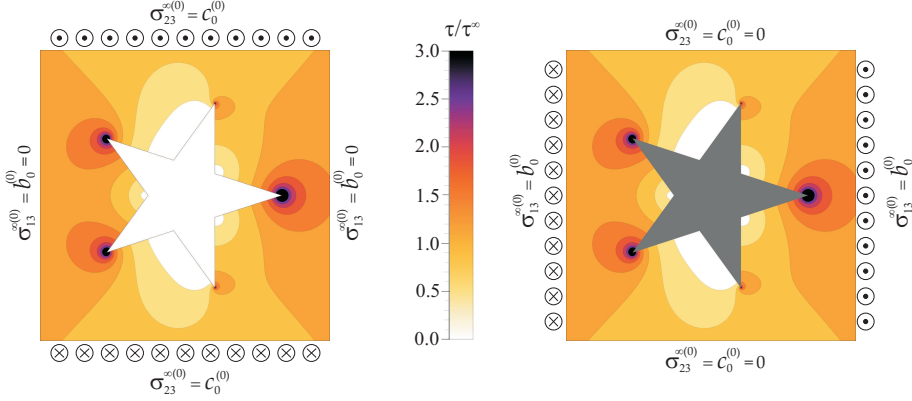


Figure 4.3: A five point star ($n = 5$, $\xi = 1/10$) polygonal void (left) is subject to a remote uniform antiplane shear (characterized by $c_0^{\star(0)}$ and $b_0^{\star(0)}=0$), while a rigid inclusion (right) is subject to the same remote shear field but rotated of $\pi/2$ (so that the remote stress field is characterized by $b_0^{\star(0)} = c_0^{\star(0)}$ and $c_0^{\star(0)} = 0$). Under these conditions, the dimensionless shear stress fields ($\tau^{(0)}(x_1, x_2)/\tau^{\infty(0)}$) are identical for both the void and the rigid inclusion.

Let us consider two remote stress fields of order m , equation (4.8), remotely applied to a matrix containing a void and a rigid inclusion (with the same shape) and which are defined respectively by the loading constants $b_0^{\star(m)}$, $c_0^{\star(m)}$ and $b_0^{\star(m)}$, $c_0^{\star(m)}$. From the obtained solution (4.35), if these constants satisfy the conditions

$$b_0^{\star(m)} = c_0^{\star(m)}, \quad b_0^{\star(m)} = -c_0^{\star(m)}, \quad (4.38)$$

then the following shear stress analogy occurs

$$\sigma_{13}^{\star(m)} \equiv \sigma_{23}^{\star(m)}, \quad \sigma_{23}^{\star(m)} \equiv -\sigma_{13}^{\star(m)}, \quad (4.39)$$

while, if the loading constants satisfy

$$b_0^{\star(m)} = -c_0^{\star(m)}, \quad b_0^{\star(m)} = c_0^{\star(m)}, \quad (4.40)$$

then another shear stress analogy occurs

$$\sigma_{13}^{\star(m)} \equiv -\sigma_{23}^{\star(m)}, \quad \sigma_{23}^{\star(m)} \equiv \sigma_{13}^{\star(m)}. \quad (4.41)$$

Considering the above analogies, whenever the loading constants satisfy the conditions

$$\left| b_0^{\star(m)} \right| = \left| c_0^{\star(m)} \right|, \quad \left| b_0^{\star(m)} \right| = \left| c_0^{\star(m)} \right|, \quad b_0^{\star(m)} c_0^{\star(m)} = -b_0^{\star(m)} c_0^{\star(m)}, \quad (4.42)$$

the modulus of the shear stress, equation (2.13), within the matrix generated by the void or by the inclusion are the same

$$\tau^{\star(m)} \equiv \tau^{\star(m)}. \quad (4.43)$$

An example of the identity of the fields of shear stress modulus generated by a void and a rigid inclusion under the conditions (4.42) is shown in Fig. 4.3 in the particular case of uniform remote stress, $m = 0$.

Chapter 5

Stress singularities, invisibilities and stress annihilations

Notch stress intensity factors and stress intensity factors are obtained analytically for isotaxal star-shaped polygonal voids and rigid inclusions (and also for the corresponding limit cases of star-shaped cracks and stiffeners), when loaded through remote inhomogeneous (self-equilibrated, polynomial) antiplane shear stress in an infinite linear elastic matrix. Usually these solutions show stress singularities at the inclusion corners. It is shown that an infinite set of geometries and loading conditions exist for which not only the singularity is absent, but the stress vanishes ('annihilates') at the corners. Thus the material, which even without the inclusion corners would have a finite stress, remains unstressed at these points in spite of the applied remote load. Moreover, similar conditions are determined in which a star-shaped crack or stiffener leaves the ambient stress completely unperturbed, thus reaching a condition of 'quasi-static invisibility'. Stress annihilation and invisibility define optimal loading modes for the overall strength of a composite and are useful for designing ultra-resistant materials.

5.1 Introduction

The knowledge of the stress intensity factor (SIF) and of the notch stress intensity factor (NSIF), respectively, for star-shaped cracks/stiffeners and isotaxal star-shaped polygonal voids/rigid-inclusions is crucial as they represent failure criteria in the design of brittle-matrix composites [80]. Therefore, results presented in Part I [115] of this study are complemented with the analytical, closed-form determination of SIF and NSIF. In this way, a full characterization of the stress fields near star-shaped cracks/stiffeners and polygonal voids/rigid-inclusions is reached. This allows for the analysis of the conditions of inclusion neutrality that occur when the ambient field is left unperturbed outside the inclusion. The neutrality condition has been thoroughly analyzed [81, 83, 91, 94, 95, 141, 96, 144] because it provides a criterion for the introduction of an inclusion in a composite without a loss of strength and because it is a problem linked to homogenization techniques for composites [86].

Recently, elastic cloaking in metamaterials has demonstrated wave invisibility [84, 85, 87, 88, 89, 92, 93] and is, in a sense, a dynamic counterpart to neutrality. Both neutrality and invisibility are strong conditions that cannot be achieved in an exact sense for a perfectly bonded inclusion [85, 94]. So neutrality, in statics, has been relaxed with the introduction of ‘quasi-neutrality’ [82], which allows rapidly decaying stress singularities at the inclusion boundary to be neglected. In fact, considering a problem of inclusion involving singularities (as for instance at an inclusion vertex) it seems at a first glance impossible to achieve neutrality or invisibility. Nevertheless, it will be demonstrated in this article that two special cases exist for an infinite class of geometries and modes of loading in which the ‘usual’ stress singularity is absent. One of these situations occurs at the vertex of a star-shaped void or rigid inclusion and will be termed ‘stress annihilation’, while the other, occurring for a star-shaped crack or stiffener, will be termed ‘quasi-static invisibility’ (or full neutrality). In the former case, the stress *vanishes* at the corner of the void/inclusion, instead of displaying the singularity which would be usually expected at a sharp corner, while, in the latter case, the star-shaped crack or star-shaped inclusion leaves the ambient stress field *completely unperturbed*, so that the inclusion becomes ‘invisible’ or ‘fully neutral’ (the word ‘neutrality’ is weak, because in the case analyzed in this article the stress remains completely

undisturbed everywhere in the matrix, so that the inclusion simply ‘disappears’). Note that the conditions of stress annihilation and invisibility imply that the material does not fail at the void/inclusion/crack/stiffener points, but far from them and only when the material would break in the unperturbed problem. It is also shown that there are specific situations in which a partial invisibility and a partial stress annihilation is reached. In these cases invisibility or stress annihilation are verified at some but not all of the points of the star-shaped crack/stiffener or void/inclusion, so that in these cases failure of the material occurs at the points where the stress remains singular.

The results obtained in the present article (and in Part I) refer to regular shapes of inclusions/cracks and to an infinite elastic domain, so that it is natural to address the question on how these two idealizations affect the results, particularly for quasi-static invisibility and stress annihilation. It is therefore shown that these situations can also be met for irregular star-shaped voids and cracks. Moreover, a numerical (finite elements) analysis shows that the features are present also for finite domains.

The present article is organized as follows. In Section 5.2 the SIFs and NSIFs, respectively for star-shaped cracks and stiffeners and for isotaxal star-shaped void and rigid inclusions will be determined. Note that the determination is in a closed-form, so that the solution does not involve infinite series. In section 5.3 results will be presented in terms of stress fields around voids and cracks. Also in Section 5.3 the conditions for quasi-static invisibility and stress annihilation will be explained in detail, together with the situations of partial invisibility and partial stress annihilation. Generalizations to irregular star-shaped voids/inclusions (and cracks/stiffeners) and inclusions in a finite domain will be covered in Section 5.3.3.

5.2 Stress and Notch Intensity Factors

A measure of the stress intensification at an inclusion vertex can be obtained through the evaluation of the Stress Intensity Factor (SIF) for a star-shaped crack or a stiffener and of the Notch Stress Intensity Factor (NSIF), in the case of a polygonal void or rigid inclusion. The definition of these factors is given in relation to the specific form of remote shear stress ($\tau_{\rho 3}$ and $\tau_{\theta 3}$ in a polar coordinate system ρ , θ , and x_3), in a way that

the asymptotic singular fields are represented by a constant depending only on the boundary conditions [137]. In particular, with reference to the decomposition (considered in Part I) of the displacement field u_3 in its symmetric and antisymmetric parts,

$$\sigma_{\rho 3}^A(\rho, 0) = \sigma_{\vartheta 3}^S(\rho, 0) = 0, \quad (5.1)$$

the definition of SIF is introduced for star-shaped crack or stiffener

$$K_{\text{III}}^S = \lim_{\rho \rightarrow 0} \sqrt{2\pi\rho} \sigma_{\rho 3}(\rho, 0), \quad K_{\text{III}}^A = \lim_{\rho \rightarrow 0} \sqrt{2\pi\rho} \sigma_{\vartheta 3}(\rho, 0), \quad (5.2)$$

while, for star-shaped void or rigid inclusion, the definition of NSIF is introduced as

$$K_{\text{III}}^S = \lim_{\rho \rightarrow 0} \sqrt{2\pi} \rho^{-\lambda_1^S} \sigma_{\rho 3}(\rho, 0), \quad K_{\text{III}}^A = \lim_{\rho \rightarrow 0} \sqrt{2\pi} \rho^{-\lambda_1^A} \sigma_{\vartheta 3}(\rho, 0). \quad (5.3)$$

Note that, differently from the definition of SIF, the definition of NSIF provides non-null values even in the case of non-singular leading-order terms, corresponding to the case of a non-negative smaller eigenvalue, $\lambda_1 \geq 0$ (see Table 1 in Part I of this study).

Following the procedure proposed in [122], a closed-form expression for $K_{\text{III}}^{(m)}$ is obtained, by considering isotaxal star-shaped voids or star-shaped cracks and rigid-inclusions within an isotropic matrix subject to a remote generic polynomial stress condition of order m (as introduced in Part I). The SIF and NSIF, obtained with reference to the situation in which an inclusion vertex lies on the positive part of x_1 axis (see Fig.2 in Part I), are crucial to predict fracture initiation (or propagation), via energy release rate, [98, 99, 100].

5.2.1 Closed-form formulae of SIFs for star-shaped cracks or stiffeners

Using the complex potential obtained in Part I for the case of n -pointed star-shaped crack or stiffener (equation (51) of Part I), the stress field can

be expressed in the transformed plane as

$$\begin{aligned} \sigma_{13}^{(m)} - i\sigma_{23}^{(m)} &= \frac{a^m 2^{\frac{2}{n}-t}}{(1 - \zeta^{-n})(1 + \zeta^{-n})^{\frac{2-n}{n}}} \sum_{j=0}^q \frac{(m+1-jn)}{j!} \\ &\times \left(T^{(m)} \zeta^{m-jn} - \chi \overline{T^{(m)}} \frac{1}{\zeta^{m+2-jn}} \right) \prod_{l=0}^{j-1} (t-l), \end{aligned} \quad (5.4)$$

where $\chi = 1$ ($\chi = -1$) for a void (for a rigid inclusion). Equation (6.6) can be expanded about the vertex of the inclusion (at $x_1 = a$ and $x_2 = 0$), by introducing $\zeta = 1 + \zeta^*$ with $|\zeta^*| \rightarrow 0$ (corresponding to $z = a + z^*$ with $|z^*| \rightarrow 0$, see Fig. 2 in Part I), as

$$\begin{aligned} \sigma_{13}^{(m)} - i\sigma_{23}^{(m)} &\simeq \frac{a^m \left[b_0^{(m)}(1 - \chi) - i c_0^{(m)}(1 + \chi) \right]}{2^{t-1} n(m+1) \zeta^*} \\ &\times \sum_{j=0}^q \frac{(m+1-jn)}{j!} \prod_{l=0}^{j-1} (t-l). \end{aligned} \quad (5.5)$$

Considering now the conformal mapping [equation (42) of Part I], the relationship between the physical coordinate $z^* = \rho e^{i\vartheta}$ and its conformal counterpart ζ^* can be expanded as

$$\zeta^* \simeq 2\sqrt{\frac{\rho}{na}} e^{\frac{i\vartheta}{2}}, \quad (5.6)$$

so that the following asymptotic expansion in the physical plane is obtained

$$\begin{aligned} \sigma_{13}^{(m)} - i\sigma_{23}^{(m)} &\simeq \frac{a^m \sqrt{a} \left[b_0^{(m)}(1 - \chi) - \beta c_0^{(m)}(1 + \chi) \right]}{2^t (m+1) \sqrt{n\rho}} \left(\cos \frac{\vartheta}{2} \right. \\ &\left. - i \sin \frac{\vartheta}{2} \right) \sum_{j=0}^q \frac{(m+1-jn)}{j!} \prod_{l=0}^{j-1} (t-l), \end{aligned} \quad (5.7)$$

from which, according to the asymptotic description (Sect.2.2 in Part I), the square root stress singularity at the star point is evident. Using definition (6.10), the SIF can be evaluated as

$$\begin{aligned} \begin{bmatrix} K_{\text{III}}^{\text{S}}(n, m) \\ K_{\text{III}}^{\text{A}}(n, m) \end{bmatrix} &= \frac{2^{\frac{n-4(m+1)}{2n}} a^m}{m+1} \sqrt{\frac{\pi a}{n}} \\ &\times \left[\sum_{j=0}^q \frac{(m+1-jn)}{j!} \prod_{l=0}^{j-1} (t-l) \right] \begin{bmatrix} (1-\chi)b_0^{(m)} \\ (1+\chi)c_0^{(m)} \end{bmatrix}, \end{aligned} \quad (5.8)$$

so that the SIFs for a star-shaped crack $K_{\text{III}}^{\star\text{S}}(n, m)$ or a star-shaped stiffener $K_{\text{III}}^{\star\text{A}}(n, m)$ are

$$\begin{aligned} \begin{bmatrix} K_{\text{III}}^{\star\text{S}}(n, m) \\ K_{\text{III}}^{\star\text{A}}(n, m) \end{bmatrix} &= \frac{2^{\frac{3n-4(m+1)}{2n}} a^m}{m+1} \sqrt{\frac{\pi a}{n}} \times \left[\sum_{j=0}^q \frac{(m+1-jn)}{j!} \prod_{l=0}^{j-1} (t-l) \right] \begin{bmatrix} b_0^{(m)} \\ c_0^{(m)} \end{bmatrix}, \end{aligned} \quad (5.9)$$

and $K_{\text{III}}^{\star\text{A}}(n, m) = K_{\text{III}}^{\star\text{S}}(n, m) = 0$.

Taking into account the definition of remote applied shear stress τ_{13}^{∞} and τ_{23}^{∞} [see equation (7) of Part I], which provides the unperturbed stress components as a function of the loading parameters $b_0^{(m)}$, $c_0^{(m)}$, the Stress Intensity Factors (5.9) can be rewritten as

$$\begin{aligned} \begin{bmatrix} K_{\text{III}}^{\star\text{S}}(n, m) \\ K_{\text{III}}^{\star\text{A}}(n, m) \end{bmatrix} &= \frac{2^{\frac{3n-4(m+1)}{2n}}}{(m+1)\sqrt{n}} \times \left[\sum_{j=0}^q \frac{(m+1-jn)}{j!} \prod_{l=0}^{j-1} (t \right. \\ &\left. - l) \right] \sqrt{\pi a} \begin{bmatrix} \sigma_{13}^{\infty(m)}(a, 0) \\ \sigma_{23}^{\infty(m)}(a, 0) \end{bmatrix}. \end{aligned} \quad (5.10)$$

The SIFs are reported in Fig. 5.1 as functions of the number n of the tips and for different orders m of the applied remote polynomial antiplane shear loading. Expression (6.18) for the SIFs simplifies in the special cases listed below.

- $t = 2(m + 1)/n \in \mathbb{N}$,

$$\begin{bmatrix} K_{\text{III}}^{\star\text{S}}(n, m) \\ K_{\text{III}}^{\star\text{A}}(n, m) \end{bmatrix} = \frac{2^{\frac{3n-4(m+1)}{2n}}}{(m+1)\sqrt{n}} \sum_{j=0}^q \frac{t!(m+1-jn)}{j!(t-j)!} \sqrt{\pi a} \begin{bmatrix} \sigma_{13}^{\infty(m)}(a, 0) \\ \sigma_{23}^{\infty(m)}(a, 0) \end{bmatrix}. \quad (5.11)$$

- $n > m + 1$ (and therefore $q = 0$),

$$\begin{bmatrix} K_{\text{III}}^{\star\text{S}}(n, m) \\ K_{\text{III}}^{\star\text{A}}(n, m) \end{bmatrix} = \frac{2^{\frac{3n-4(m+1)}{2n}}}{\sqrt{n}} \sqrt{\pi a} \begin{bmatrix} \sigma_{13}^{\infty(m)}(a, 0) \\ \sigma_{23}^{\infty(m)}(a, 0) \end{bmatrix}. \quad (5.12)$$

This case embraces an infinite set of solutions, one such solution is that for a cruciform crack ($n = 4$, Fig.4 of Part I) subject to uniform, linear and quadratic remote antiplane shear load ($m = 0, 1, 2$).

- $n = 2$ (crack or stiffener inclusions),

$$\begin{bmatrix} K_{\text{III}}^{\star\text{S}}(n, m) \\ K_{\text{III}}^{\star\text{A}}(n, m) \end{bmatrix} = \frac{\sqrt{\pi a}}{2^m(m+1)} \sum_{j=0}^q \frac{(m+1)!(m+1-2j)}{j!(m+1-j)!} \begin{bmatrix} \sigma_{13}^{\infty(m)}(a, 0) \\ \sigma_{23}^{\infty(m)}(a, 0) \end{bmatrix}. \quad (5.13)$$

Note that, in the particular case of uniform antiplane shear ($m = 0$), equation (6.15) provides the same result as equation (32) in [140].

5.2.2 Closed-form formulae of NSIFs for isotoxal star-shaped voids and rigid inclusions

For the derivation of SIFs and NSIFs, different methods (FE analysis, BE analysis, Singular integral equations etc.) are involved [137, 101, 102, 103, 104, 105], so that closed-form expressions of SIFs and NSIFs using full-field information, to the best of authors' knowledge, have only been provided for the case of polygonal voids and rigid inclusions inclusions

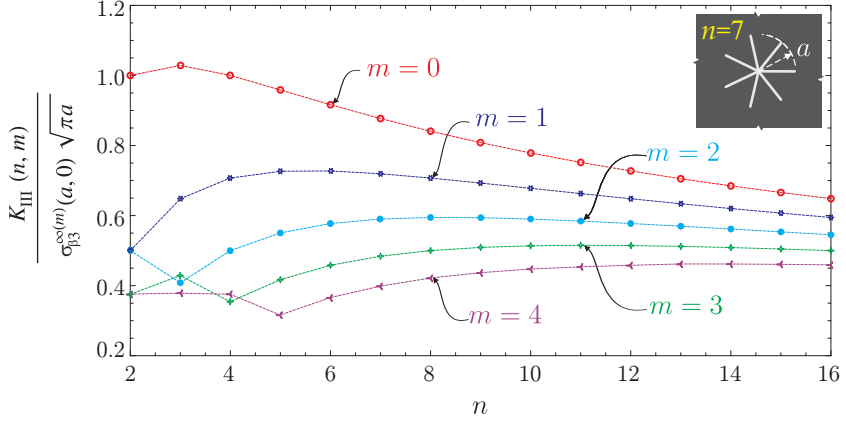


Figure 5.1: Stress intensity factors for both star-shaped cracks K_{III}^{\star} and star-shaped stiffeners K_{III}^{\star} as functions of the number n of crack or stiffener tips, for different orders m of the applied remote polynomial antiplane shear loading. Note that, due to the division by the unperturbed stress $\sigma_{\beta 3}^{\infty}$ evaluated at the inclusion vertex $(a, 0)$, cracks ($\beta = 1$) and stiffeners ($\beta = 2$) display the same SIF, independently of the loading parameters $b_0^{(m)}$ and $c_0^{(m)}$. A single crack or stiffener corresponds to $n = 2$, which in all cases does not correspond to the maximum SIF.

under uniform anti-plane condition ($m = 0$) [122]. The NSIFs at the vertex of an n -pointed isotaxal star void or rigid inclusion within an elastic material subject to remote polynomial loading are analytically evaluated. For the considered n -pointed isotaxal star polygon, the external semi-angle at each vertex is $\alpha = \pi(1 - \xi)$, so assuming that the angle parameter ξ ranges within $[0, 1/2 - 1/n]$, the leading-order terms in the asymptotic expansion of the stress fields about a vertex are associated to the following eigenvalues

$$\begin{cases} \lambda_1^{\star S}(\xi) = \lambda_1^{\star A}(\xi) = \frac{\xi}{1 - \xi} \geq 0, \\ \lambda_1^{\star A}(\xi) = \lambda_1^{\star S}(\xi) = -\frac{1 - 2\xi}{2(1 - \xi)} < 0. \end{cases} \quad (5.14)$$

Using the complex potential obtained in Part I, eqn (72), and the derivative of the conformal mapping (56), the stress field in the trans-

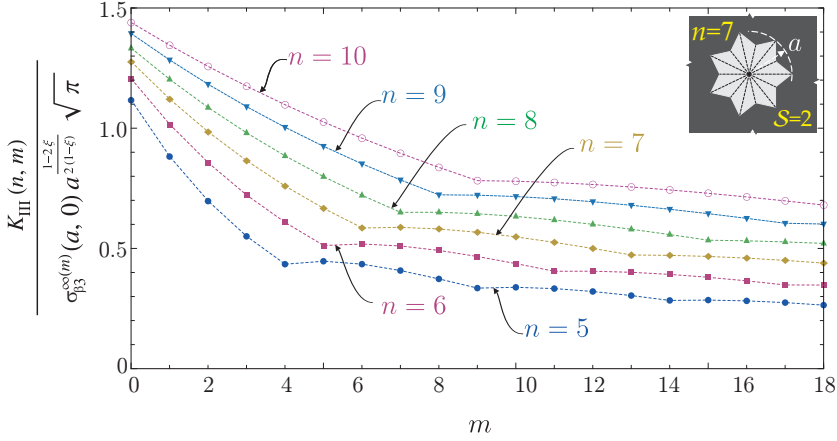


Figure 5.2: Notch stress intensity factors for both isotaxal star-shaped polygonal voids K_{III}^{\star} and rigid inclusions K_{III}^{\star} for $\mathcal{S} = 2$, functions of the order m of the applied remote polynomial antiplane shear loading. Note that, due to the division by the unperturbed stress $\sigma_{\beta 3}^{\infty}$ evaluated at the inclusion vertex $(a, 0)$, voids ($\beta = 1$) and rigid inclusions ($\beta = 2$) display the same NSIF, independently of the loading parameters $b_0^{(m)}$ and $c_0^{(m)}$. A uniform remote shear stress field corresponds to $m = 0$, which in all cases corresponds to the maximum NSIF.

formed plane can be obtained from equation (30)₂ as

$$\sigma_{13}^{(m)} - i\sigma_{23}^{(m)} = \frac{(a\Omega(n, \xi))^m \zeta^2 \sum_{j=0}^q (m+1-jn)L_{m+1-jn} \left(T^{(m)}\zeta^{m-jn} - \chi \overline{T^{(m)}} \frac{1}{\zeta^{m+2-jn}} \right)}{(\zeta^n - 1)^{1-2\xi} (\zeta^n + 1)^{2(\xi + \frac{1}{n}) - 1}}, \quad (5.15)$$

which can be expanded about the neighborhood of the vertex (at $x_1 = a$ and $x_2 = 0$) by introducing $\zeta = 1 + \zeta^*$ with $|\zeta^*| \rightarrow 0$ (corresponding to $z = a + z^*$ with $|z^*| \rightarrow 0$) as

$$\sigma_{13}^{(m)} - i\sigma_{23}^{(m)} \simeq \frac{(a\Omega(n, \xi))^m \left[(1 - \chi)b_0^{(m)} - i(1 + \chi)c_0^{(m)} \right]}{m+1} \frac{2^{1-2\xi - \frac{2}{n}} \sum_{j=0}^q (m+1-jn)L_{m+1-jn}}{n^{1-2\xi} (\zeta^*)^{1-2\xi}}. \quad (5.16)$$

A further exploitation of the first derivative of the conformal mapping (56) discloses the asymptotic relation between the physical coordinate $z^* = \rho e^{B\vartheta}$ and its conformal counterpart ζ^*

$$\zeta^* \simeq 2^{\frac{n(1-\xi)-1}{n(1-\xi)}} n^{\frac{2\xi-1}{2(1-\xi)}} \left(\frac{1-\xi}{a\Omega(n,\xi)} \rho e^{B\vartheta} \right)^{\frac{1}{2(1-\xi)}}, \quad (5.17)$$

which leads to the following asymptotic expansion in the physical plane

$$\begin{aligned} \sigma_{13}^{(m)} - i\sigma_{23}^{(m)} &\simeq \frac{(a\Omega(n,\xi))^m}{(m+1)2^{\frac{1}{n(1-\xi)}}} \left(\frac{a\Omega(n,\xi)}{n(1-\xi)\rho} \right)^{\frac{1-2\xi}{2(1-\xi)}} \\ &\times \left[(1-\chi)b_0^{(m)} - i(1+\chi)c_0^{(m)} \right] \left[\cos \left(\frac{1-2\xi}{2(1-\xi)}\vartheta \right) \right] \\ &- i \sin \left(\frac{1-2\xi}{2(1-\xi)}\vartheta \right) \left] \sum_{j=0}^q (m+1-jn)L_{m+1-jn}. \end{aligned} \quad (5.18)$$

From the asymptotic expansion of the stress field (5.18), the NSIFs associated to the (singular or non-singular) leading-order term can be evaluated using definition (5.3) as

$$\begin{aligned} \begin{bmatrix} K_{\text{III}}^{\star\text{S}}(n,m) \\ K_{\text{III}}^{\star\text{A}}(n,m) \end{bmatrix} &= \frac{2\sqrt{2\pi} (a\Omega(n,\xi))^m}{(m+1)2^{\frac{1}{n(1-\xi)}}} \left(\frac{a\Omega(n,\xi)}{n(1-\xi)} \right)^{\frac{1-2\xi}{2(1-\xi)}} \\ &\times \sum_{j=0}^q (m+1-jn)L_{m+1-jn} \begin{bmatrix} b_0^{(m)} \\ c_0^{(m)} \end{bmatrix}, \end{aligned} \quad (5.19)$$

which, considering the value of the unperturbed stress components τ_{13}^∞ and τ_{23}^∞ [see equation (7) of Part I] at the void/inclusion vertex ($x_1 = a, x_2 = 0$), can be rewritten as

$$\begin{aligned} \begin{bmatrix} K_{\text{III}}^{\star\text{S}}(n,m) \\ K_{\text{III}}^{\star\text{A}}(n,m) \end{bmatrix} &= \frac{2\sqrt{2\pi} (\Omega(n,\xi))^m}{(m+1)2^{\frac{1}{n(1-\xi)}}} \left(\frac{a\Omega(n,\xi)}{n(1-\xi)} \right)^{\frac{1-2\xi}{2(1-\xi)}} \\ &\times \sum_{j=0}^q (m+1-jn)L_{m+1-jn} \begin{bmatrix} \sigma_{13}^{\infty(m)}(a,0) \\ \sigma_{23}^{\infty(m)}(a,0) \end{bmatrix}. \end{aligned} \quad (5.20)$$

The Notch Stress Intensity Factors (5.20) simplify in the special cases listed below.

- n -sided regular polygon

$$\begin{aligned} \begin{bmatrix} K_{\text{III}}^{\star\text{S}}(n, m) \\ K_{\text{III}}^{\star\text{A}}(n, m) \end{bmatrix} &= \frac{2\sqrt{2\pi} (\Omega(n))^m}{m+1} \left(\frac{a\Omega(n)}{n+2} \right)^{\frac{2}{n+2}} \\ &\times \sum_{j=0}^q (m+1-jn) L_{m+1-jn} \begin{bmatrix} \sigma_{13}^{\infty(m)}(a, 0) \\ \sigma_{23}^{\infty(m)}(a, 0) \end{bmatrix}. \end{aligned} \quad (5.21)$$

- n -pointed regular star polygon with density $\mathcal{S} = 2$ (with $n \geq 4$),

$$\begin{aligned} \begin{bmatrix} K_{\text{III}}^{\star\text{S}}(n, m) \\ K_{\text{III}}^{\star\text{A}}(n, m) \end{bmatrix} &= \frac{2^{\frac{n+6}{n+4}} \sqrt{2\pi} (\Omega(n))^m}{m+1} \left(\frac{a\Omega(n)}{n+4} \right)^{\frac{4}{n+4}} \\ &\times \sum_{j=0}^q (m+1-jn) L_{m+1-jn} \begin{bmatrix} \sigma_{13}^{\infty(m)}(a, 0) \\ \sigma_{23}^{\infty(m)}(a, 0) \end{bmatrix}. \end{aligned} \quad (5.22)$$

Moreover, in the case that $m+1 < n$ (so that $q = 0$) the following identity holds

$$\sum_{j=0}^q (m+1-jn) L_{m+1-jn} = m+1. \quad (5.23)$$

This case embraces an infinite set of solutions, one such solution is that for a 5-pointed isotoxal star-shaped void or rigid inclusion subject to uniform, linear, quadratic and cubic remote antiplane shear load ($m = 0, 1, 2, 3$). Therefore, the Notch Stress Intensity Factors (5.20) for the generic n -pointed isotoxal star polygon reduces to

$$\begin{aligned} \begin{bmatrix} K_{\text{III}}^{\star\text{S}}(n, m) \\ K_{\text{III}}^{\star\text{A}}(n, m) \end{bmatrix} &= \frac{2\sqrt{2\pi} (\Omega(n, \xi))^m}{2^{\frac{1}{n(1-\xi)}}} \times \left(\frac{a\Omega(n, \xi)}{n(1-\xi)} \right)^{\frac{1-2\xi}{2(1-\xi)}} \begin{bmatrix} \sigma_{13}^{\infty(m)}(a, 0) \\ \sigma_{23}^{\infty(m)}(a, 0) \end{bmatrix}, \end{aligned} \quad (5.24)$$

which simplifies in the following special cases to

- n -sided regular polygon

$$\begin{bmatrix} K_{\text{III}}^{\star\text{S}}(n, m) \\ K_{\text{III}}^{\star\text{A}}(n, m) \end{bmatrix} = 2\sqrt{2\pi} (\Omega(n))^m \left(\frac{a\Omega(n)}{n+2} \right)^{\frac{2}{n+2}} \begin{bmatrix} \sigma_{13}^{\infty(m)}(a, 0) \\ \sigma_{23}^{\infty(m)}(a, 0) \end{bmatrix}. \quad (5.25)$$

- n -pointed regular star polygon with density $\mathcal{S} = 2$ (with $n \geq 4$),

$$\begin{bmatrix} K_{\text{III}}^{\star\text{S}}(n, m) \\ K_{\text{III}}^{\star\text{A}}(n, m) \end{bmatrix} = 2^{\frac{n+6}{n+4}} \sqrt{2\pi} (\Omega(n))^m \left(\frac{a\Omega(n)}{n+4} \right)^{\frac{4}{n+4}} \begin{bmatrix} \sigma_{13}^{\infty(m)}(a, 0) \\ \sigma_{23}^{\infty(m)}(a, 0) \end{bmatrix}. \quad (5.26)$$

5.3 Stress fields, annihilation and invisibility

Results obtained in terms of the full-field solution (Part I of this study) allows for the complete determination of the stress field near an isotoxal star-shaped polygonal void or rigid inclusion, including the limits of star-shaped cracks and stiffeners. The purpose of this section is to present the determination of stress fields and give full evidence for the important cases when invisibility or stress annihilation occurs, two situations in which the solution does not display a singular behaviour, so that the material is in an optimal situation with respect to failure.

The stress fields that are presented in Figs. 5.3 – 5.9 refer for simplicity to cracks and voids, but it is known from Section 3.3 of Part I that a stress analogy holds for a void and a rigid inclusion of identical shape, so that the presented results are also valid for rigid inclusions and stiffeners, with the proper interchange between constants $b_0^{(m)}$ and $c_0^{(m)}$ as indicated in Section 3.3 of Part I.

Level sets of the modulus of the shear stress are reported in Fig. 5.3 for three and four pointed ($n=3, 4$) star-shaped cracks with uniform ($m=0$), linear ($m=1$), and quadratic ($m=2$) remote stress field. Note that ‘normally’ the crack strongly perturbs the stress field and induces a square-root

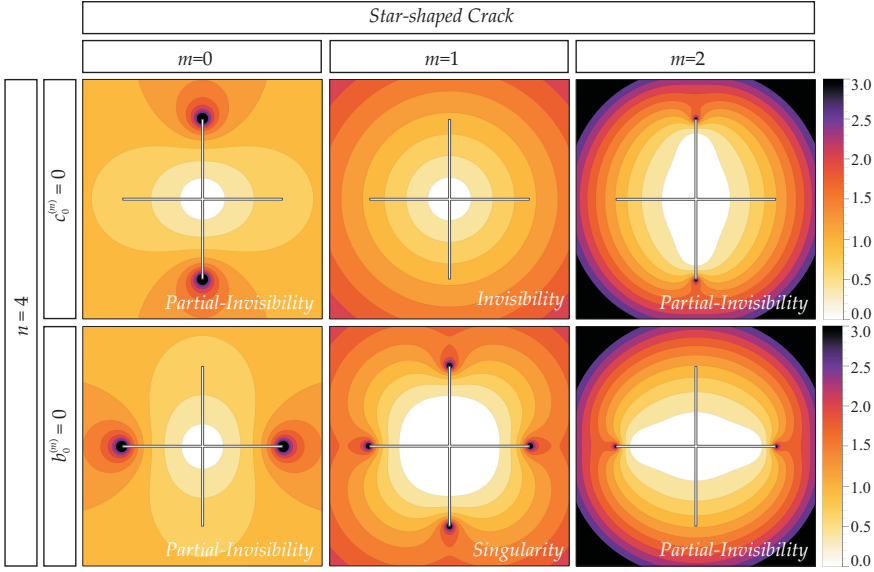


Figure 5.3: Level sets of shear stress modulus $(\tau^{(m)}(x_1, x_2)/\tau^{\infty(m)}(a, 0))$ near 4-pointed star-shaped cracks (cruciform crack), for different orders m of the applied remote polynomial antiplane shear loading ($m = 0$ uniform, $m = 1$ linear, and $m = 2$ quadratic shear loading). Some cases of invisibility and partial-invisibility are shown; note that invisibility occurs only for certain combinations of n and m (while for the single crack invisibility is independent of m , see Fig. 5.4).

singularity at each point of the star. In special cases ($\{m, n\} = \{2, 3\}$ and $\{m, n\} = \{1, 4\}$ marked in the figure), however, the solution remains completely unperturbed (so that the level sets of the modulus of shear stress displays a concentric circular structure). In these cases the star-shaped crack (or stiffener, with the due changes in the loading coefficients, see Section 3.3 of Part I) remains ‘completely neutral’ or ‘invisible’.

The single crack or stiffener is the only example of inclusion which can remain invisible at every loading order m . This invisibility occurs for $c_0^{(m)} = 0$ and is shown (for $m = 0, 1, 2$) in the middle part of Fig. 5.4, while in the upper part the ‘usual’ cases of stress singularity are reported, for $b_0^{(m)} = 0$. The situation of a single crack (or stiffener) is also detailed in the lower part of Fig. 5.4, where the modulus of the shear stress is

Figure 5.4: Usual cases of stress singularity ($b_0^{(m)} = 0$, upper part), versus invisibility ($c_0^{(m)} = 0$, middle part) for a single crack evidenced by the field of dimensionless modulus of shear stress ($\tau^{(m)}(x_1, x_2)/\tau^{\infty(m)}(a, 0)$). In addition, shear stress modulus ($\tau^{(m)}(x_1, 0)/\tau^{\infty(m)}(a, 0)$, lower part) ahead of the crack tip is also detailed (lower part). Different orders m of the applied remote polynomial antiplane shear loading are considered ($m = 0$ uniform, $m = 1$ linear, and $m = 2$ quadratic shear loading). The single crack (or the single stiffener), $n = 2$, is the only case for which the invisibility holds at every order of applied remote shear loading, $m = 0, 1, 2, \dots \in \mathbb{N}$.

reported ahead of the crack (or stiffener) tip and the difference between singularity and invisibility can be further appreciated.

Results for isotoxal star-shaped polygonal voids are reported in Fig. 5.5 in terms of level sets of the modulus of the shear stress for regular polygonal ($n=4$ and $\mathcal{S} = 1$) and regular star-shaped ($n=6$ and $\mathcal{S} = 2$) polygonal voids at uniform ($m=0$), linear ($m=1$), and quadratic ($m=2$) remote stress field.

Fig. 5.6 shows the modulus of the shear stress ahead of the star-shaped polygonal void ($n=5, 6$ and $\mathcal{S} = 2$) and star-shaped crack ($n=5, 6$), at different values of m ($=2,4,5,9$), and the difference between singularity, annihilation and invisibility can be observed.

Two cases of stress singularity and stress annihilation along the perimeter of a pentagonal void and a pentagram-shaped void are reported in Fig. 5.7.

An isotoxal star-shaped polygonal void tends to a star-shaped crack when the semi-angle at the inclusion vertex ($\xi\pi$) decreases and tends to zero. It is therefore expected that the stress field generated near an isotoxal star-shaped void tends to that corresponding to a star-shaped crack. This tendency is confirmed by the results shown in Fig. 5.8, where the modulus of the shear stress ahead of a void vertex for different values of ξ is presented. Note that in the right part of Fig. 5.8 the conditions have been selected ($n = 4, m = 1$) for which the star-shaped crack becomes invisible and the polygonal void exhibits the stress annihilation.

The same situation of a polygonal and star-shaped void for which the stress annihilation is verified and the parameter ξ is decreased is also reported in Fig. 5.9, where the level sets of the shear stress modulus

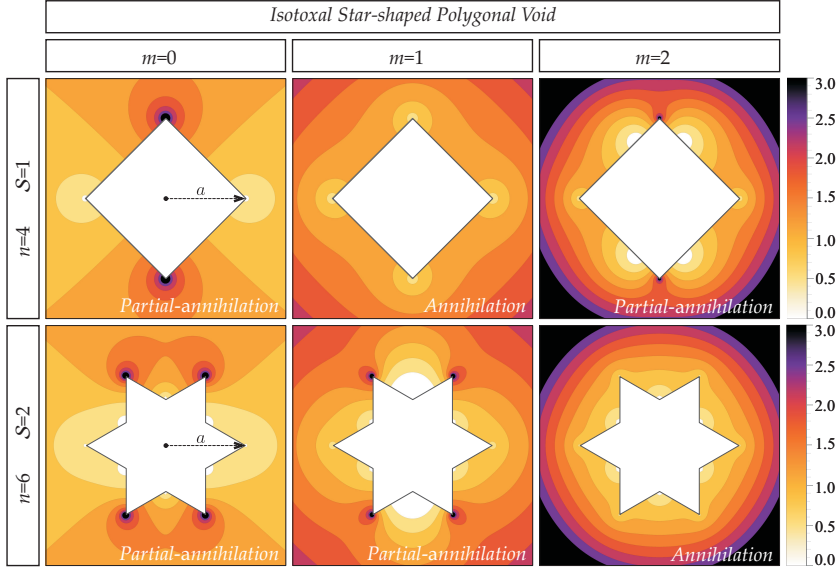


Figure 5.5: Level sets of shear stress modulus $(\tau^{(m)}(x_1, x_2)/\tau^{\infty(m)}(a, 0))$ near n -pointed isotoxal star-shaped voids, for different starriness \mathcal{S} (regular polygonal ($n=4$ and $\mathcal{S} = 1$), regular star-shaped ($n=6$ and $\mathcal{S} = 2$)) and orders m of the applied remote polynomial antiplane shear loading ($m = 0$ uniform, $m = 1$ linear, and $m = 2$ quadratic shear loading) for $c_0^{(m)} = 0$. Some cases of stress annihilation and partial-annihilation are shown, which occur only for certain combinations of n and m .

$\tau^{(m)}(x_1, x_2)/\tau^{\infty(m)}(a, 0)$ for $n = 3, 6$ and $m = 2$ are plotted. It may be concluded from this figure that, for decreasing values of the semi-angle at the inclusion vertex ($\pi\xi$), a transition can be observed from stress annihilation to a sort of ‘quasi-invisibility’, obtained in the proximity of the limit of star-shaped crack, where the stress field is only slightly perturbed.

An interesting situation can be envisaged in the limit when the number of points of a star-shaped crack grow and tend to infinity. This is explored in Fig. 5.10, where the modulus of shear stress ahead of the crack tip located on the x_1 -axis is reported. The stress field tends with increasing n to the stress distribution corresponding to a circular void with radius equal to the crack length.

5.3.1 The rules of invisibility and annihilation

In the previous figures several cases of star-shaped crack (or stiffener) invisibility and stress annihilation at the points of an isotoxal star-shaped void (or rigid inclusion) have been presented. It is therefore now convenient to establish the rules governing these two important situations.

The formulae of SIFs and NSIFs (5.9) and (5.19), respectively, highlight that the loading coefficients $b_0^{(m)}$ and $c_0^{(m)}$ control the stress singularity, which can be deactivated at the vertex aligned on the x_1 axis in the following two cases

- for a crack or a void $\chi = 1$ when $c_0^{(m)} = 0$,
- for a stiffener or a rigid inclusion $\chi = -1$ when $b_0^{(m)} = 0$.

The stress singularity can simultaneously be deactivated at all vertices of the void or rigid inclusion, when the above conditions are verified together with the following constraints between the loading order m and number of the star points n

$$m = \begin{cases} nj - 1 & \text{if } n \text{ is odd,} \\ \frac{n}{2}j - 1 & \text{if } n \text{ is even,} \end{cases} \quad (5.27)$$

where $j \in \mathbb{N}_1$. Note that eqn (6.31) is equivalent to $2(m+1)/n \in \mathbb{N}_1$.

In the case of star-shaped cracks or stiffeners, conditions (6.31) imply that the perturbed potential, eqn (52)₂ of Part I, is pointwise null $g^p = 0$, so that the deactivation of the singularity corresponds to ‘invisibility’ or ‘full neutrality’. In the case of isotoxal star-shaped voids or rigid inclusions, setting $\gamma = 2\pi/n$ in eqns (10) of Part I, conditions (6.31) imply that the loading coefficients satisfy the conditions $\hat{b}_0^{(m)} = b_0^{(m)}$ and $\hat{c}_0^{(m)} = c_0^{(m)}$, so that the deactivation of the singularity corresponds to ‘stress annihilation’. Note that the stress annihilation follows not only from the lack of stress singularity, but also from the fact that the leading-order term in the stress asymptotic expansion is a positive power of the radial distance from the vertex (Section 2.2 of Part I).

5.3.2 Partial-invisibility and Partial-annihilation

Partial invisibility or partial stress annihilation occurs respectively when some of the crack/stiffener tips are invisible or when some of the points of the star-shaped void/inclusion are stress-free. In these situations, which are more frequent than the cases of full annihilation and invisibility, the material fails at one of the points where the stress remains singular.

Cases of partial invisibility are reported in Fig. 5.3. In particular, the horizontal crack is invisible for $n = 3$, $m = 1$, and $c_0^{(m)} = 0$ and for $n = 4$, $m = 0, 2$, and $c_0^{(m)} = 0$; the vertical crack is invisible for $n = 4$, $m = 0, 2$, and $b_0^{(m)} = 0$. All examples reported in Fig. 5.5 present at least partial stress annihilation, which occurs at all vertices located along the horizontal x_1 -axis.

5.3.3 Beyond the hypotheses of infinite matrix and regular shape inclusion

Inclusion invisibility and stress annihilation have been demonstrated under the assumptions that the inclusions have a *regular* shape and that the matrix is *infinite*. It is suggested in this Section that these two hypotheses can be relaxed, so that the two concepts of invisibility and stress annihilation are more general than it has been demonstrated analytically.

A finite portion of an elastic body is considered ideally ‘cut’ from the infinite elastic space subjected to the m -th order polynomial field considered in Part I of this study [equations (11) and (12)]. Therefore, the boundary of the cut body is assumed subject to the traction conditions transmitted by the rest of the elastic space. In this way, polynomial displacement and stress fields are realized within the body in the absence of any inclusion. When invisibility is achieved for the infinite body (as related to the presence of zero-traction or zero-displacements lines, inclined at $\hat{\theta}_j = j\pi/(m+1)$, $j \in [0, \dots, 2m+1]$), it will also hold for the body ‘cut’ from the infinite body. This is shown in Fig. 5.11 (lower part), where invisibility is achieved for a finite elastic body and irregular star-shaped crack.

If now the cut body has an external boundary with the shape of a regular polygonal shape, symmetric with respect to all the inclinations $\hat{\theta}_j$,

the introduction of a n -sided regular polygonal void (or a rigid inclusion) satisfying eqn (6.31), realizes a stress field which annihilates at the inclusion vertices, as Fig. 5.11 (upper and central parts) shows for polygonal voids.

The results presented in Fig. 5.11, in terms of modulus of shear stress level sets near polygonal voids, have been obtained numerically (using the finite element software Comsol Multiphysics[©] version 4.2a, by exploiting the analogy between the antiplane problem and the 2-dimensional heat transfer equation under stationary conditions), by imposing traction boundary conditions at the external contour of the body. To avoid the presence of a rigid-body motion, the open boundary condition available in the software has been selected.

In the simulations, the domains have been discretized at two levels by the free triangular user-controlled custom mesh. At the first level, the entire domains are meshed with maximum and minimum element sizes equal to $10^{-2}R$ and $10^{-5}R$, respectively, where R denotes the unit radius of the circle inscribing the domain. At the second level, the inclusion boundaries have been meshed with maximum and minimum element sizes equal to $10^{-3}R$ and $10^{-5}R$, respectively.

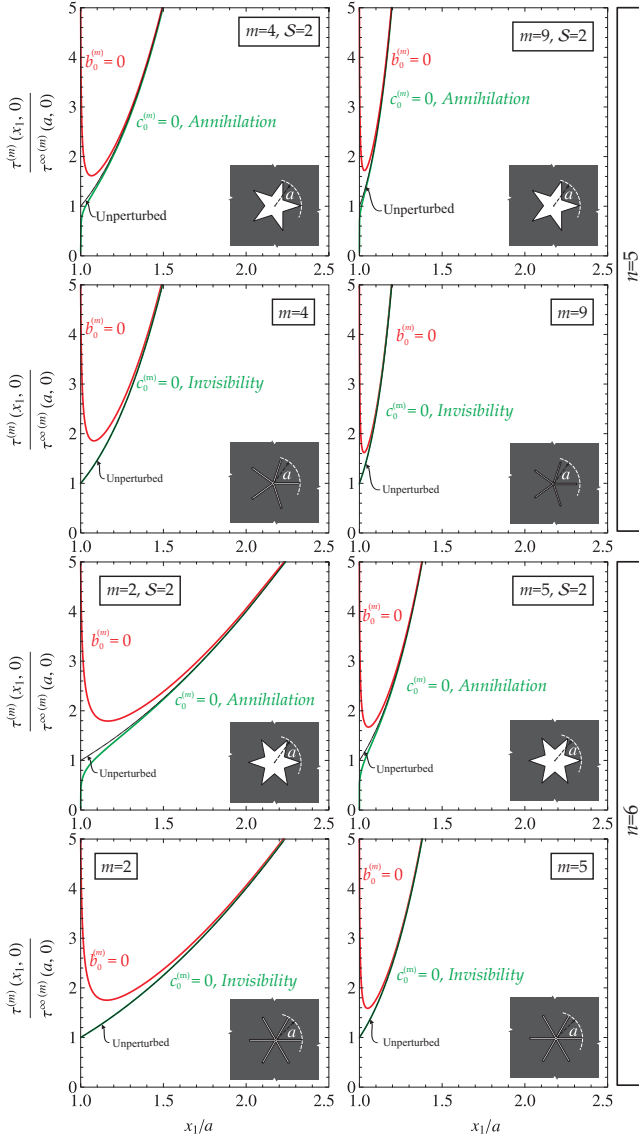


Figure 5.6: Cases of stress annihilation of a star-shaped isotaxal polygonal void and star-shaped crack, for different values of m and n . The shear stress modulus ahead of one of void vertex ($\tau^{(m)}(x_1, 0)/\tau^{\infty(m)}(a, 0)$) is reported for the cases $b_0^{(m)} = 0$ (red), $c_0^{(m)} = 0$ (green), and unperturbed (black). Note that the green curve coincides with the black curve when inclusion invisibility occurs.

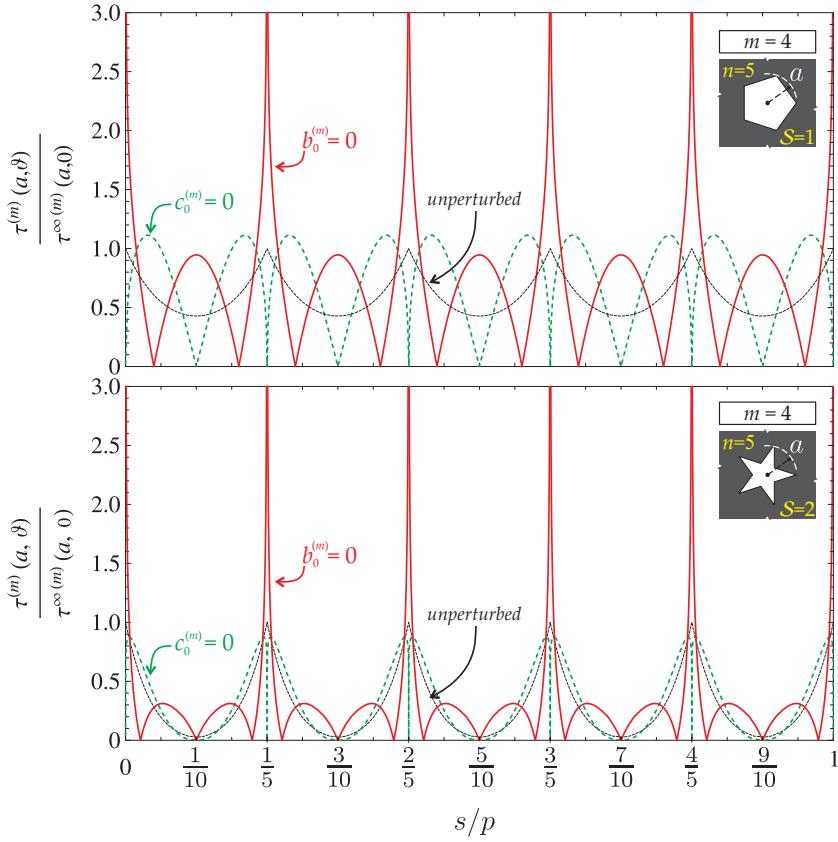


Figure 5.7: Stress singularity ($b_0^{(m)} = 0$, reported in red) and stress annihilation ($c_0^{(m)} = 0$, reported in green) for a regular pentagon-shaped ($n = 5$, $\mathcal{S} = 1$, upper part) and regular pentagram-shaped ($n = 5$, $\mathcal{S} = 2$, lower part) void for the case of fourth-order remote shear field $m = 4$. The modulus of the shear stress is reported along the perimeter of the figures, measured by the coordinate s (made dimensionless through division by the length of the perimeter p), so that $s/p = j$ corresponds to the j -th vertex. Note that the singularity produced by the pentagram-shaped void is stronger than that produced by the pentagonal void, because the angles at the vertex of the pentagram are sharper than that of the curvilinear coordinates along the inclusion perimeter the pentagon.

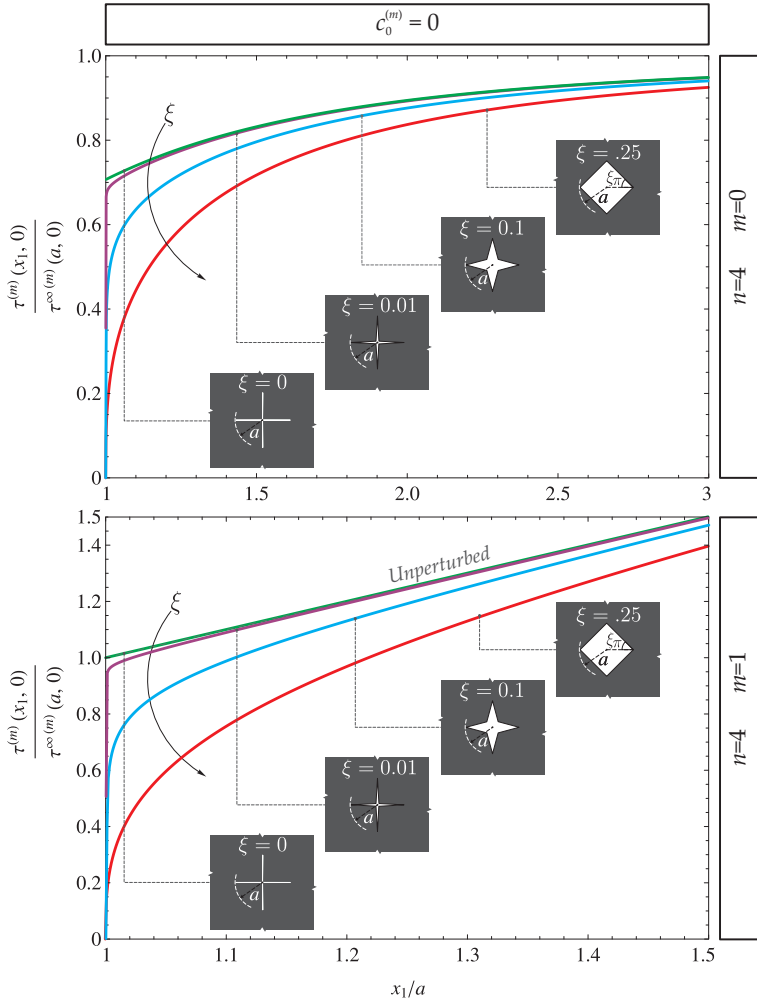


Figure 5.8: Effect of the reduction in the semi-angle of an inclusion vertex ($\xi\pi$) on the modulus of the shear stress ahead of the vertex. The shear stress distribution tends to that corresponding to a star-shaped crack when ξ tends to zero (note the boundary layer). A uniform remote stress field ($m = 0$, $c_0^{(0)} = 0$) is considered on the left for a four-pointed star, while a case corresponding to stress annihilation and invisibility is considered on the right ($m = 1$, $c_0^{(1)} = 0$).

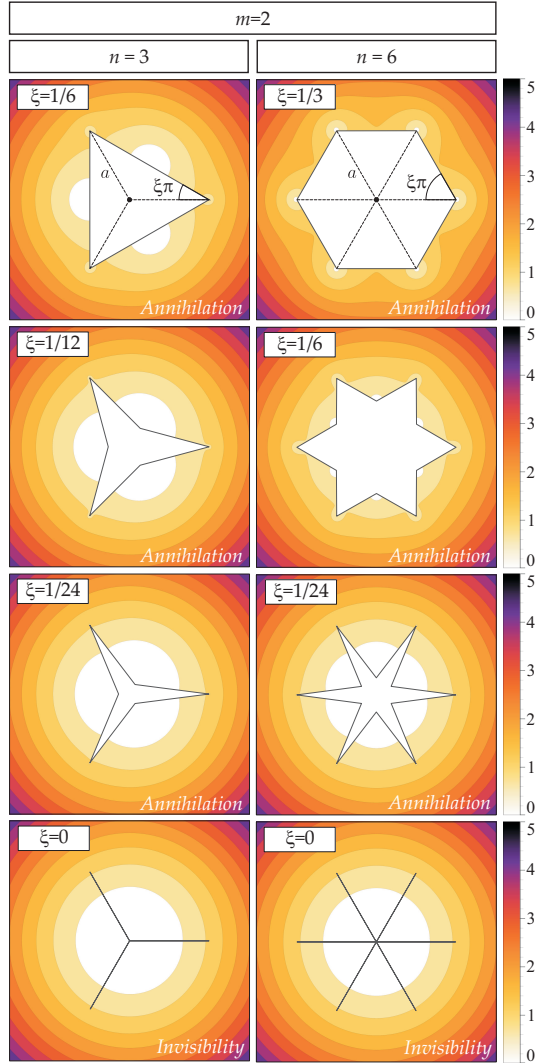


Figure 5.9: Cases of stress annihilation of n -pointed isotoxal polygonal voids of star-shaped cracks subject to a quadratic remote antiplane shear load ($c_0^{(m)} = 0$) are shown for different values of ξ . Level sets of shear stress modulus ($\tau^{(m)}(x_1, x_2)/\tau^{\infty(m)}(a, 0)$) are reported, in particular the transition from stress annihilation to the invisibility occurs when ξ tends to zero.

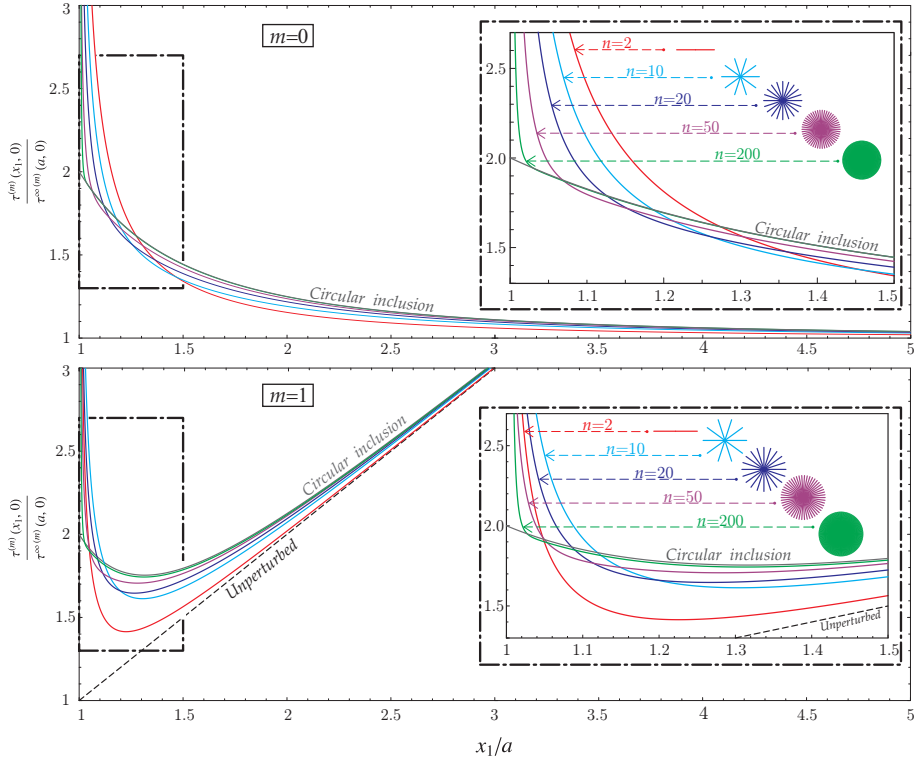


Figure 5.10: Shear stress modulus ($\tau^{(m)}(x_1, 0)/\tau^{\infty(m)}(a, 0)$) ahead of the crack lying on the x_1 -axis of a star-shaped crack, subject to uniform ($m = 0$, upper part) and linear ($m = 1$, lower part) antiplane shear. Several values of points n are considered, so that it can be noted that the stress field correctly tends to the solution of a circular void (obtained at $n \rightarrow \infty$), which exhibits the well-known value of stress concentration factor (SCF=2), independent of the loading order m .

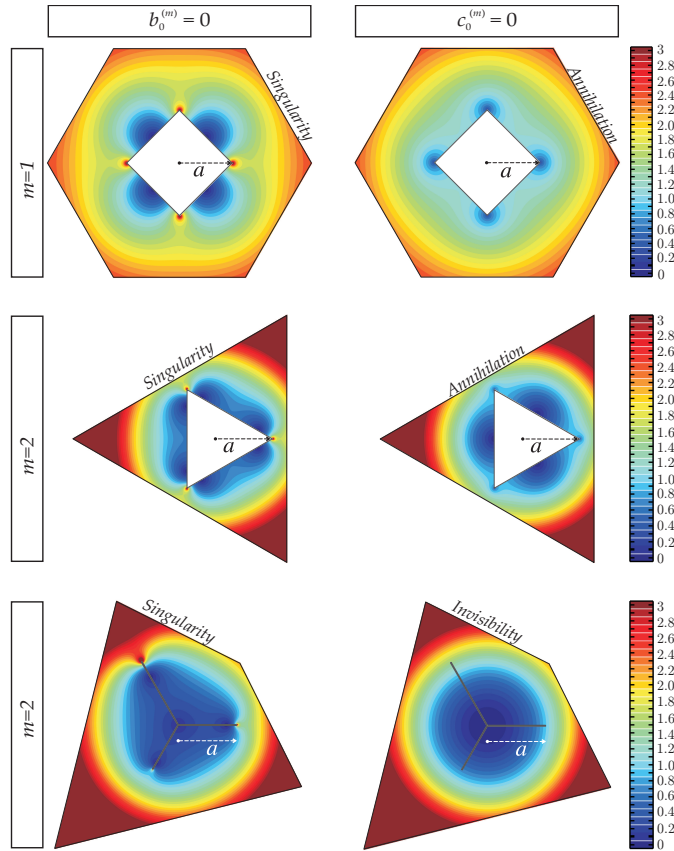


Figure 5.11: Effect of finiteness of the domain in which a polygonal void is embedded, evidenced through the level sets of shear stress modulus $\tau^{(m)}(x_1, x_2)$ (made dimensionless through division by $\tau^{\infty(m)}(a, 0)$) obtained numerically for three different geometries: (upper part) a regular hexagonal matrix containing a concentric square void, (central part) a regular triangular matrix containing a concentric triangular void, and (lower part) a quadrilateral containing a three-pointed irregular star-shaped crack. Stress singularity is obtained for $b_0^{(m)} = 0$ (left), while stress annihilation (for star-shaped polygonal void) and invisibility (for star-shaped crack) occurs for $c_0^{(m)} = 0$ (right).

Chapter 6

Stress singularities vs stress reductions

Stress field solutions and Stress Intensity Factors (SIFs) are found for n -cusped hypocycloidal shaped voids and rigid inclusions in an infinite linear elastic plane subject to nonuniform remote antiplane loading, using complex potential and conformal mapping. It is shown that a void with hypocycloidal shape can lead to a higher SIF than that induced by a corresponding star-shaped crack; this is counter intuitive as the latter usually produces a more severe stress field in the material. Moreover, it is observed that when the order m of the polynomial governing the remote loading grows, the stress fields generated by the hypocycloidal-shaped void and the star-shaped crack tend to coincide, so that they become equivalent from the point of view of a failure analysis. Finally, special geometries and loading conditions are discovered for which there is no stress singularity at the inclusion cusps and where the stress is even reduced with respect to the case of the absence of the inclusion. The concept of Stress Reduction Factor (SRF) in the presence of a sharp wedge is therefore introduced, contrasting with the well-known definition of Stress Concentration Factor (SCF) in the presence of inclusions with smooth boundary. The results presented in this paper provide criteria that will help in the design of ultra strong composite materials, where stress singularities always promote failure. Furthermore, they will facilitate finding the special conditions where resistance can be optimized in the presence of inclusions with non-smooth boundary.

6.1 Introduction

The determination of the stress field near a crack, a stiffener, an inclusion, or a defect in an elastic matrix material is a key problem in the design of composites [107, 111, 121, 119, 136, 138], as such stress fields exhibit strong stress concentrations that can impose severe limitations on the strength of composites.

In the present article a rigid inclusion or a void is analyzed with a *hypocycloidal* shape of order n embedded in an elastic-isotropic plane subject to a remote loading condition of *nonuniform* antiplane shear represented as a polynomial of order m . For uniform remote load ($m = 0$), this problem has been thoroughly investigated, for both the cases of rigid inclusions and voids, when plane [109, 110, 112, 113, 117, 118, 128, 133, 134, 135] or antiplane [129, 130, 142, 143] conditions prevail; a case of non-linear elastic behaviour has also been recently considered [144]. However, the disuniformity in the applied load ($m \neq 0$), analyzed here for the first time, yields unexpected and counter intuitive results, which are important to understand the complexity arising from the highly-varying fields that can develop in composite materials deformed in extreme conditions. In particular, in the present work polynomial *shear* loading at infinity is prescribed (as in [115, 116, 141]) to an elastic-isotropic plane, containing a void or a rigid inclusion with an n -cusped hypocycloidal shape. This problem is solved in an analytical form both for the stress full-field and for the stress intensity factor, solutions which reveal several phenomena of interplay between stress singularities and stress reduction, which remain undetected for uniform applied loads. The most important of these phenomena are the following.

(i.) Under uniform stress conditions the stress intensity factor at a cusp of an hypocycloidal void is always smaller than that at a tip of a star-shaped crack, so that a crack tip is more detrimental to strength than a cusp, the same is not true for certain orders m of polynomial fields of remote loading. In these cases, a hypocycloidal void leads a material to failure more easily than a star-shaped crack.

(ii.) While for uniform loading a stress singularity is always present at a cusp, for certain orders m of polynomial fields of remote loading, this singularity can disappear, so that the stress can lie below the value corresponding to the unperturbed field. This effect has been quantified

by introducing the notion of ‘Stress Reduction Factor’ (SRF), which is shown to increase with the number n of cusps and to decrease with the order m of the polynomial load. Note that the concept of SRF contrasts with the well-known definition of Stress Concentration Factor, introduced in the presence of inclusions with smooth boundaries and representing the increase of the stress state at the inclusion boundary with respect to the case when the inclusion is absent.

(iii.) For orders of polynomial loading m much greater than the number n of cusps of the hypocycloidal inclusion, the stress state generated in the matrix tends to coincide with that generated by an n -pointed star-shaped crack or rigid inclusion.

Some of the above concepts are elucidated in Fig. 6.1, where the level sets of the modulus of the shear stress are plotted from the closed form solution (obtained in Section 6.2) near three- and six- cusped rigid hypocycloidal inclusions, for quadratic ($m = 2$) loadings. The ‘red spots’ visible near the inclusion cusps in Fig. 6.1 (left column) are the signature of stress singularity generated when the loading is defined by $c_0^{(m)} = 0$. When the loading is defined by $b_0^{(m)} = 0$ stress singularities disappear, so that stress reduction occurs at all the vertices of the inclusion (Fig. 6.1, right column), where the stress falls below the value that would be present if the inclusion was absent (see also Fig. 6.6).

Photoelastic investigations [124, 131] confirm the severe stress fields theoretically predicted for materials containing stiff inclusions and show that these fields may yield failure instead of reinforcement for composite materials [114, 120, 126, 132]. Therefore, the results given in the present article show possibilities of greatly enhancing the strength of composites through the careful design of the inclusion shapes careful design of the inclusion shape, thus opening the way to the realization of ultra-strong materials.

6.2 Closed-form solution for hypocycloidal-shaped inclusion

In this Section, the closed-form solution is obtained for the out-of-plane problem of a n -cusped hypocycloidal void or rigid inclusion embedded in

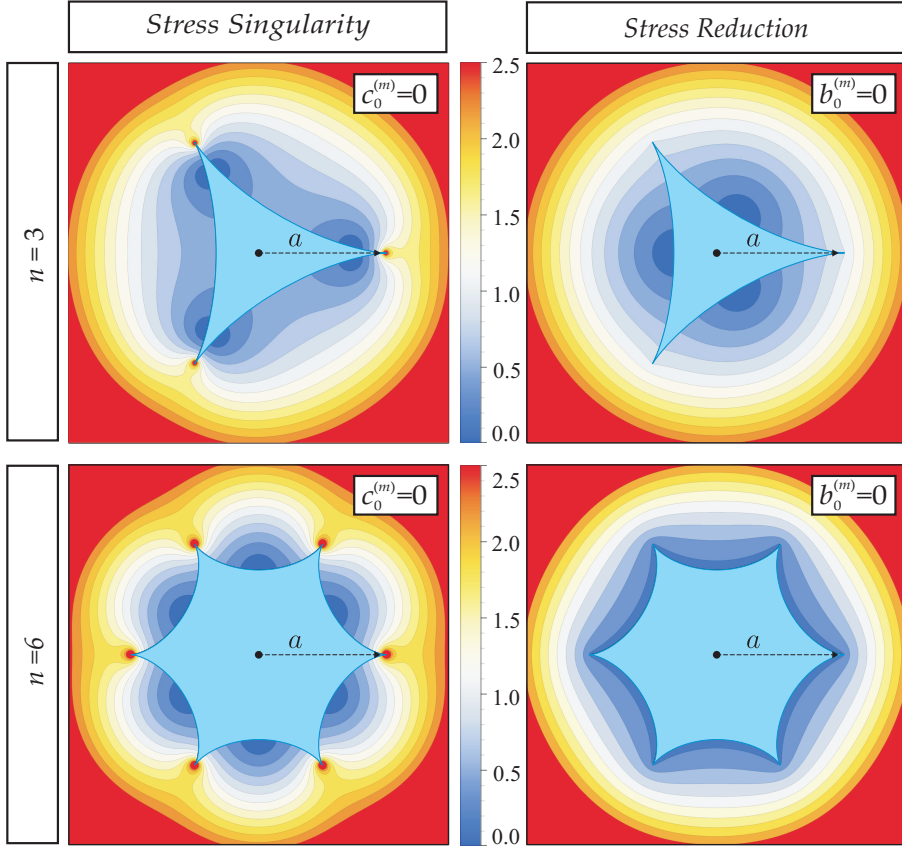


Figure 6.1: Level sets of dimensionless shear stress modulus $\tau^{(m)}(x_1, x_2)/\tau^{\infty(m)}(a, 0)$ near n -cusped rigid inclusions ($n = 3$ and $n = 6$), subject to quadratic ($m = 2$) remote out-of-plane shearing, showing stress singularity (left column, $c_0^{(m)} = 0$) and stress reduction (right column, $b_0^{(m)} = 0$). In the figures a stress singularity corresponds to the appearance of a ‘red spot’ at the inclusion cusp. In the cases showing stress reduction, the stress singularity is absent and the stress at all the cusps is smaller than that which would be attained without the inclusion.

an infinite elastic material with remote boundary conditions expressed by the polynomial (4.9). The two-dimensional Laplace equation (2.9) for the displacement field w can be solved through the complex potential technique. The boundary of an inclusion in an infinite plane can be mapped

into a circle of unit radius in the conformal plane (where the position is given by the variable ζ) by means of a conformal mapping $z = \omega(\zeta)$. The elastic out-of-plane problem can therefore be solved through a complex potential $g(\zeta)$, related to the displacement u_3 , stresses σ_{13} , σ_{23} , and shear force resultant $F_{\widehat{BC}}$ (along the arc \widehat{BC}) given by the equations (2.29).

In the case of hypocycloidal inclusions, see Fig. 2.5 (upper part (I)), with a number n of cusps ($n \in \mathbb{Z}$, $n \geq 2$), the function $\omega(\zeta)$ mapping the exterior region of the inclusion (within the physical z – plane) onto the exterior region of the unit circle (within the conformal ζ – plane, Fig. 2.5, (upper part (I))) is given by [123] equation (2.76).

Considering the superposition principle, the complex potential $g(z)$ can be decomposed as the sum of the unperturbed $g^\infty(z)$ and perturbed $g^p(z)$ potentials, the former describing the solution in the case that the inclusion is absent while the latter defining the perturbation introduced by the presence of the inclusion also mentioned in the previous chapters. With reference to the polynomial expression (4.1) for the remote displacement boundary condition, and taking into account equation (2.76) and (4.20), by means of the generalized binomial theorem, the unperturbed potential can be expressed as

$$g^\infty(\zeta) = (a\Omega(n))^{m+1} T^{(m)} \sum_{j=0}^{m+1} \binom{m+1}{j} \frac{\zeta^{m+1-jn}}{(n-1)^j}, \quad (6.1)$$

where $\binom{.}{.}$ is the binomial coefficient.

Considering that the null traction resultant condition $F_{\widehat{BC}} = 0$ holds for the hypocycloidal void ($\chi = 1$), and the rigid-body displacement condition $u_{3B} = u_{3C}$ holds for (every pairs of points B and C along the boundary of) the hypocycloidal rigid inclusion ($\chi = -1$), the perturbed

complex potential g^p is obtained in the form

$$g^p(\zeta) = (a\Omega(n))^{m+1} \left\{ \overline{\chi T^{(m)}} \left[-\frac{(qn)!}{q! [q(n-1)]! (n-1)^q} \delta_{m+1,qn} + \sum_{j=0}^q \binom{m+1}{j} \frac{1}{(n-1)^j \zeta^{m+1-jn}} \right] - T^{(m)} \sum_{j=q+1}^{m+1} \binom{m+1}{j} \frac{1}{(n-1)^j \zeta^{jn-m-1}} \right\}, \quad (6.2)$$

where the integer parameter $q = \lfloor (m+1)/n \rfloor$ is introduced, with the symbol $\lfloor \cdot \rfloor$ standing for the integer part of the relevant argument, so that the complex potential $g(\zeta)$ follows from the sum of unperturbed and perturbed complex potentials as

$$g(\zeta) = (a\Omega(n))^{m+1} \left[-\frac{(qn)!}{q! [q(n-1)]! (n-1)^q} \overline{\chi T^{(m)}} \delta_{m+1,qn} + \sum_{j=0}^q \binom{m+1}{j} \frac{1}{(n-1)^j} \left(T^{(m)} \zeta^{m+1-jn} + \frac{\overline{\chi T^{(m)}}}{\zeta^{m+1-jn}} \right) \right]. \quad (6.3)$$

It is worth noting that solution (6.3) simplifies in some special cases, as

- $n > m + 1$ (or, equivalently, $q = 0$)

$$g(\zeta) = (a\Omega(n))^{m+1} \left[T^{(m)} \zeta^{m+1} + \frac{\overline{\chi T^{(m)}}}{\zeta^{m+1}} \right], \quad (6.4)$$

which is similar to the solution in the conformal plane for the circular and polygonal inclusions;

- $m = 0$ (corresponding to the case of uniform antiplane shear [112])

$$g(\zeta) = a\Omega(n) \left[T^{(0)} \zeta + \frac{\overline{\chi T^{(0)}}}{\zeta} \right]. \quad (6.5)$$

As in the cases of cracks and rigid line inclusions [115, 116, 122, 140], a square root stress singularity at the cusps of an hypocycloidal void or rigid inclusion is predicted in the theory of elasticity [112, 130, 117, 133]. In this section the Stress Intensity Factors are derived as functions of the cusp number n and of the polynomial order m of the load. Moreover, conditions for which stress singularities disappear are defined and a special feature is observed, namely, the stress reduction, which corresponds to the fact that the stress measured at the cusp is smaller than that present at the same point in the absence of the inclusion.

From the solution (6.3) obtained in the previous Section, the stress field near a n -cusped hypocycloidal void and rigid inclusion is given by

$$\tau_{13}^{(m)} - i\tau_{23}^{(m)} = \frac{(a\Omega(n))^m}{(1-\zeta^{-n})} \sum_{j=0}^q \binom{m+1}{j} \frac{m+1-nj}{(n-1)^j} \left(T^{(m)} \zeta^{m-jn} - \frac{\chi \overline{T^{(m)}}}{\zeta^{m+2-jn}} \right). \quad (6.6)$$

Focusing the attention on the inclusion cusp located at the point $(x_1 = a, x_2 = 0)$ and introducing a local reference system centered in the mapped cusp $(\zeta^* = \zeta - 1)$, the stress fields (6.6) can be expanded about the cusp in the limit of $|\zeta^*| \rightarrow 0$ (corresponding to the limit $z \rightarrow a$) as

$$\tau_{13}^{(m)} - i\tau_{23}^{(m)} \approx \frac{(a\Omega(n))^m}{n(m+1)\zeta^*} \left[b_0^{(m)}(1-\chi) - i c_0^{(m)}(1+\chi) \right] \sum_{j=0}^q \binom{m+1}{j} \frac{(m+1-jn)}{(n-1)^j}. \quad (6.7)$$

Expansion of the conformal mapping (2.76) leads to the asymptotics between the relative coordinate $z^* = \rho e^{i\vartheta}$ and the conformal relative coordinate ζ^* in the form

$$\zeta^* \simeq \sqrt{\frac{2\rho}{a(n-1)}} e^{\frac{i\vartheta}{2}}, \quad (6.8)$$

so that the shear stress components can be approximated around the cusp as

$$\begin{aligned} \tau_{13}^{(m)} - i \tau_{23}^{(m)} \simeq \frac{1}{\sqrt{2\rho}} \frac{[a(n-1)]^{m+\frac{1}{2}}}{(m+1)n^{m+1}} \left[b_0^{(m)}(1-\chi) - i c_0^{(m)}(1+\chi) \right] \left(\cos \frac{\vartheta}{2} \right. \\ \left. - i \sin \frac{\vartheta}{2} \right) \sum_{j=0}^q \binom{m+1}{j} \frac{(m+1-jn)}{(n-1)^j}, \end{aligned} \quad (6.9)$$

highlighting the square root singularity in the stress field at the cusp, as predicted by the asymptotics around sharp notch [128].

6.2.1 Stress Intensity Factors

Stress Intensity Factors (SIFs) for the symmetric and the anti-symmetric out-of-plane problem are defined, respectively, as follows [137]

$$K_{\text{III}}^{\text{S}} = \lim_{\rho \rightarrow 0} \sqrt{2\pi\rho} \tau_{13}(\rho, 0), \quad K_{\text{III}}^{\text{A}} = \lim_{\rho \rightarrow 0} \sqrt{2\pi\rho} \tau_{23}(\rho, 0), \quad (6.10)$$

so that, considering the asymptotic stress field (6.9), the expression of the SIFs for a n -cusped hypocycloidal inclusion can be analytically obtained in the following closed-form expression

$$\begin{aligned} & \begin{bmatrix} K_{\text{III}}^{\text{S}}(n, m) \\ K_{\text{III}}^{\text{A}}(n, m) \end{bmatrix} \\ &= \frac{\sqrt{\pi a}(n-1)^{m+\frac{1}{2}} a^m}{n^{m+1}(m+1)} \left[\sum_{j=0}^q \binom{m+1}{j} \frac{(m+1-jn)}{(n-1)^j} \right] \begin{bmatrix} (1-\chi)b_0^{(m)} \\ (1+\chi)c_0^{(m)} \end{bmatrix}. \end{aligned} \quad (6.11)$$

Recalling that the definition (4.1) for the remote applied shear stress implies

$$\tau_{13}^{\infty(m)}(x_1 = a, 0) = b_0^{(m)} a_1^m, \quad \tau_{23}^{\infty(m)}(x_1 = a, 0) = c_0^{(m)} a_1^m, \quad (6.12)$$

the particularization of eq (6.11) to the case of a void or a rigid n -cusped hypocycloidal inclusion, leads to

$$\begin{aligned} & \begin{bmatrix} K_{\text{III}}^{\star\text{S}}(n, m) \\ K_{\text{III}}^{\diamond\text{A}}(n, m) \end{bmatrix} \\ &= \frac{2\sqrt{\pi a}(n-1)^{m+\frac{1}{2}}}{n^{m+1}(m+1)} \left[\sum_{j=0}^q \binom{m+1}{j} \frac{(m+1-jn)}{(n-1)^j} \right] \begin{bmatrix} \tau_{13}^{\infty(m)}(a, 0) \\ \tau_{23}^{\infty(m)}(a, 0) \end{bmatrix}, \end{aligned} \quad (6.13)$$

and

$$K_{\text{III}}^{\diamond\text{S}}(n, m) = K_{\text{III}}^{\star\text{A}}(n, m) = 0, \quad (6.14)$$

where the apexes \diamond and \star have been introduced to distinguish between the cases of voids and rigid inclusions.

Expression (6.13) for the SIFs simplifies in the special case $n > m + 1$ (and therefore $q = 0$)

$$\begin{bmatrix} K_{\text{III}}^{\star\text{S}}(n, m) \\ K_{\text{III}}^{\diamond\text{A}}(n, m) \end{bmatrix} = \frac{2\sqrt{\pi a}(n-1)^{m+\frac{1}{2}}}{n^{m+1}} \begin{bmatrix} \tau_{13}^{\infty(m)}(a, 0) \\ \tau_{23}^{\infty(m)}(a, 0) \end{bmatrix}. \quad (6.15)$$

The above case (6.15) embraces an infinite set of solutions, one of such solutions is that for an astroid ($n = 4$) subject to uniform, linear and quadratic remote out-of-plane shear load ($m = 0, 1, 2$). Moreover, expression (6.15) reduces to the values obtained for SIFs in the case of cracks or stiffeners ($n = 2$)

$$\begin{aligned} & \begin{bmatrix} K_{\text{III}}^{\star\text{S}}(n = 2, m) \\ K_{\text{III}}^{\diamond\text{A}}(n = 2, m) \end{bmatrix} = \frac{\sqrt{\pi a}}{2^m(m+1)} \left[\sum_{j=0}^q \binom{m+1}{j} (m+1 \right. \\ & \left. - 2j) \right] \begin{bmatrix} \tau_{13}^{\infty(m)}(a, 0) \\ \tau_{23}^{\infty(m)}(a, 0) \end{bmatrix}. \end{aligned} \quad (6.16)$$

Note that, in the particular case of uniform antiplane shear ($m = 0$), equation (6.15) provides the same result as equation (4.142) in [112].

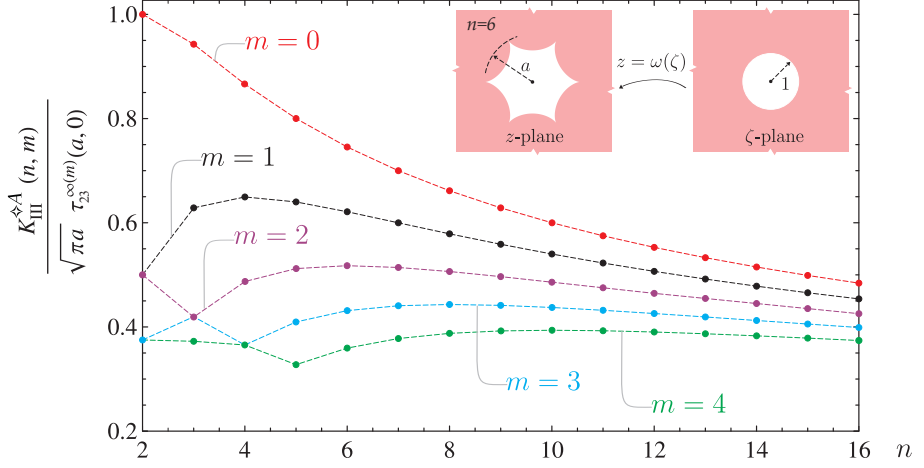


Figure 6.2: Stress Intensity Factors for n -cusped hypocycloidal voids $K_{\text{III}}^{\diamond A}(n, m)$, eq (6.13), normalized through division by the unperturbed stress evaluated at the inclusion cusp $\tau_{23}^{\infty}(a, 0)$, as a function of the order m of the remote loading. Note that the curves also represent the Stress Intensity Factors for n -cusped hypocycloidal rigid inclusions $K_{\text{III}}^{\diamond S}$, when normalized through division by the unperturbed stress evaluated at the inclusion cusp $\tau_{13}^{\infty}(a, 0)$. The inset shows the conformal mapping transforming the exterior region of a hypocycloidal inclusion (inscribed in a circle of radius a) into the exterior region of a circular inclusion of unit radius in the ζ -plane.

The SIFs for a n -cusped hypocycloidal inclusion (6.13) satisfy the following properties

$$\frac{K_{\text{III}}^{\diamond A}(n, m)}{\tau_{23}^{\infty(m)}(a, 0)} \geq \frac{K_{\text{III}}^{\diamond A}(n, m+1)}{\tau_{23}^{\infty(m+1)}(a, 0)}, \quad \frac{K_{\text{III}}^{\diamond S}(n, m)}{\tau_{13}^{\infty(m)}(a, 0)} \geq \frac{K_{\text{III}}^{\diamond S}(n, m+1)}{\tau_{13}^{\infty(m+1)}(a, 0)}, \quad (6.17)$$

and are reported in Fig. 6.2 for different values of n and m . These values are also reported in Fig. 6.3 through normalization with the respective

values for n -pointed star-shaped inclusions [116]

$$\begin{aligned} \begin{bmatrix} K_{\text{III}}^{\star\text{S}}(n, m) \\ K_{\text{III}}^{\star\text{A}}(n, m) \end{bmatrix} &= \frac{2^{\frac{3n-4(m+1)}{2n}} \sqrt{\pi a}}{(m+1)\sqrt{n}} \left[\sum_{j=0}^q \frac{(m+1-jn)}{j!} \prod_{l=0}^{j-1} \left(\frac{2(m+1)}{n} \right. \right. \\ &\quad \left. \left. - l \right) \right] \begin{bmatrix} \tau_{13}^{\infty(m)}(a, 0) \\ \tau_{23}^{\infty(m)}(a, 0) \end{bmatrix}. \end{aligned} \quad (6.18)$$

It can be noted from Fig. 6.3 that:

- differently from the uniform loading case ($m = 0$), the stress intensification around a cusp can be higher than that occurring around a crack, so that a cusp can be more detrimental to failure than a crack for certain values of m . Moreover, the following relations have been found numerically (an analytical proof looks awkward) to hold for every value used for n and m

$$K_{\text{III}}^{\star\text{A}}(n, m = n - 1) \geq K_{\text{III}}^{\star\text{A}}(n, m = n - 1), \quad (6.19)$$

$$K_{\text{III}}^{\star\text{S}}(n, m = n - 1) \geq K_{\text{III}}^{\star\text{S}}(n, m = n - 1). \quad (6.20)$$

- While the ratio between the SIFs for a hypocycloidal void and a star-shaped crack displays a monotonic increase for $m < n - 1$, an oscillatory behaviour around 1 is observed for $m > n - 1$. Such an oscillation in the SIFs' ratio evidences a decreasing amplitude, with peaks corresponding to the values $m = nj - 1$ ($j \in \mathbb{N}_1$). Therefore, when $m \gg n$, the SIF for the hypocycloidal inclusion approaches that for star-shaped inclusion, namely, the following relations have been numerically found to hold

$$K_{\text{III}}^{\star\text{A}}(n, m) \simeq K_{\text{III}}^{\diamond\text{A}}(n, m), \quad K_{\text{III}}^{\star\text{S}}(n, m) \simeq K_{\text{III}}^{\diamond\text{S}}(n, m), \quad \text{if } m \gg n. \quad (6.21)$$

Since the asymptotics for a cusp and a crack coincide, when $m \gg n$ the hypocycloidal void and the star-shaped crack tend to become mechanically equivalent, thus inducing the same stress field in the elastic plane. This property is also highlighted in Fig. 6.4, where the level sets for the shear stress modulus

$$\tau = \sqrt{\tau_{13}^2 + \tau_{23}^2}, \quad (6.22)$$

around a hypocycloidal rigid inclusion and a star-shaped stiffener are compared and shown to coalesce at high m .

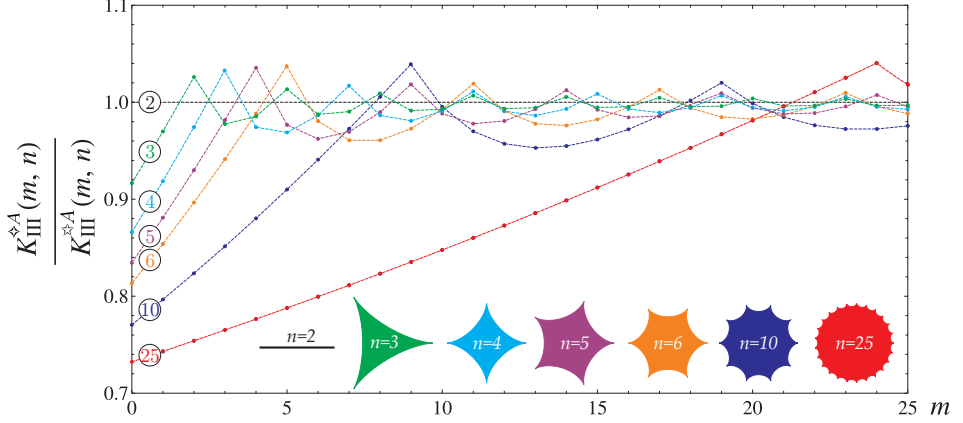


Figure 6.3: Ratio between the Stress Intensity Factors for an n -cusped hypocycloidal void $K_{III}^{\diamond A}$, eqn (6.16), and that for an n -pointed star-shaped crack $K_{III}^{\star A}$, eqn (6.18), as a function of the order m of the remote loading. A mechanical equivalence for the two geometries is observed when $m \gg n$. Note that the curves also represent the Stress Intensity Factors ratio for an n -cusped hypocycloidal rigid inclusion $K_{III}^{\diamond S}$ and for an n -pointed star-shaped stiffener $K_{III}^{\star S}$.

6.2.2 Stress Reduction Factors

In the cases of a void ($\chi = 1$), loaded with $c_0^{(m)} = 0$, or a rigid inclusion ($\chi = -1$), loaded with $b_0^{(m)} = 0$, the following equation holds

$$b_0^{(m)}(1 - \chi) - i c_0^{(m)}(1 + \chi) = 0, \quad (6.23)$$

and the asymptotic stress, eq. (6.9), loses the singular behaviour at the considered cusp, ($x_1 = a$, $x_2 = 0$), so that the asymptotics is ruled by the second-order term, the well-known S-stress ([127] and [137]). The second-order expansion for the stress field (6.6) around $\zeta = 1$ leads to

$$\tau_{13}^{(m)} - i \tau_{23}^{(m)} = \frac{(n-1)^m a^m}{n^{m+1}} \sum_{j=0}^q \binom{m+1}{j} \frac{(m+1-jn)^2}{(n-1)^j} [T + \chi \bar{T}], \quad (6.24)$$

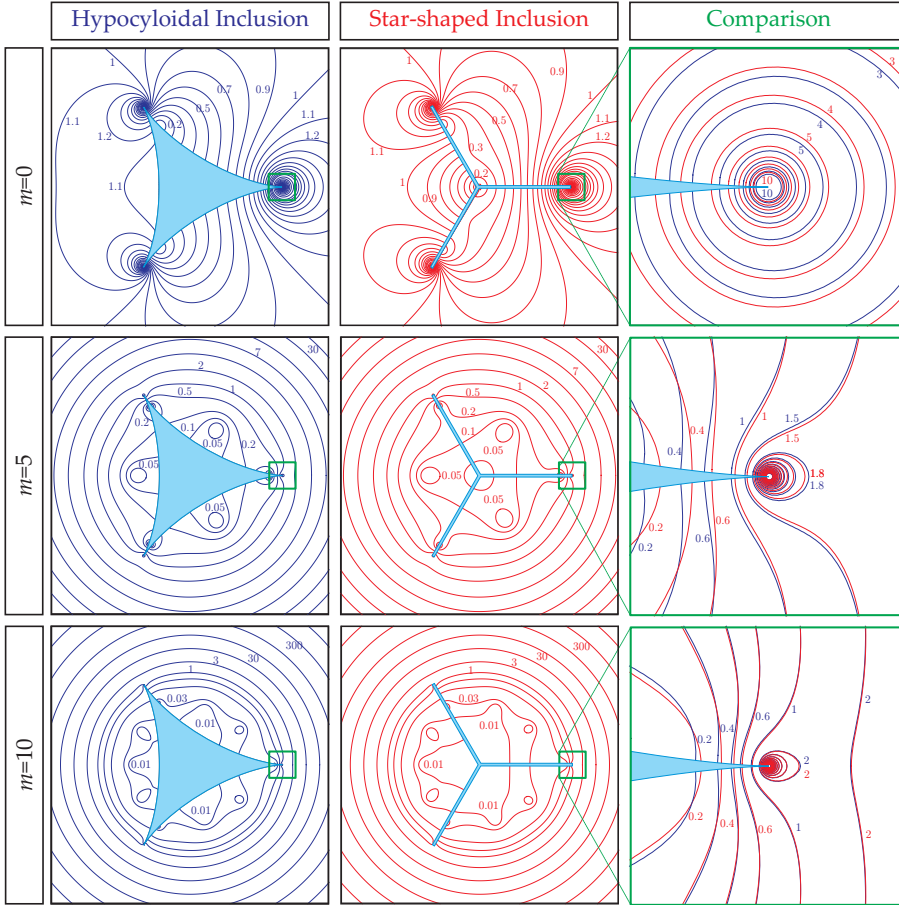


Figure 6.4: Level sets of dimensionless shear stress modulus $\tau^{(m)}(x_1, x_2)/\tau^{\infty(m)}(a, 0)$ highlighting stress singularities near n -cusped rigid inclusions (left column) and n -pointed star-shaped stiffeners (central column) at different orders m of shear load ($c_0^{(m)} = 0$). The right column shows comparisons between the two stress fields reported in the left and central column near the inclusion vertex having coordinates $x_1 = a$ and $x_2 = 0$. The mechanical equivalence can be noted between the two inclusion geometries for $m \gg n$. Note that these level sets also represent the stress state near an n -cusped hypocycloidal void (left column) and an n -pointed star-shaped crack (central column) in the case when the loading is provided by $b_0^{(m)} = 0$.

so that, recalling eq (6.12), the stress state at the cusp point $(a, 0)$ of an hypocycloidal void or a rigid inclusion can be obtained from eq (6.24) respectively as

$$\begin{cases} \tau_{13}^{\diamond(m)} = \mathcal{A}(n, m)\tau_{13}^{\infty(m)}(a, 0), \\ \tau_{23}^{\diamond(m)} = 0, \end{cases} \quad \begin{cases} \tau_{13}^{\star(m)} = 0, \\ \tau_{23}^{\star(m)} = \mathcal{A}(n, m)\tau_{23}^{\infty(m)}(a, 0), \end{cases} \quad (6.25)$$

where $\mathcal{A}(n, m)$ is the following function of the number of cusps n and the loading order m

$$\mathcal{A}(n, m) = \frac{2}{(m+1)n^{m+1}} \sum_{j=0}^q \binom{m+1}{j} \frac{(m+1-jn)^2}{(n-1)^{j-m}}. \quad (6.26)$$

When the loading condition (6.23) holds, a new parameter, the Stress Reduction Factor (SRF), can be defined as a dimensionless measure of the stress decrease at the hypocycloidal (void or rigid) cusp point with respect to the stress measured at the same point when the inclusion is absent,¹

$$\text{SRF}(n, m) := 1 - \frac{\tau^{(m)}(a, 0)}{\tau^{\infty(m)}(a, 0)} = 1 - \mathcal{A}(n, m) \in [0; 1], \quad (6.27)$$

so that the stress state at the cusp point is described by

$$\tau^{(m)}(a, 0) = [1 - \text{SRF}(n, m)] \tau^{\infty(m)}(a, 0). \quad (6.28)$$

Values of the SRF, eq (6.27), are reported in Fig. 6.5 at varying number n of cusps and for different orders m of the applied remote polynomial out-of-plane shear loading. It can be noted from the figure that two limit values are attained: (i.) $\text{SRF} \rightarrow 1$, when n grows at fixed m (see Fig. 6.5 upper part) and (ii.) $\text{SRF} \rightarrow 0$, when m grows at fixed n (see Fig. 6.5 lower part). These two limit values, $\text{SRF}=1$ and $\text{SRF}=0$ correspond respectively to a stress annihilation and to an unchanged stress amount at the cusp point. It can be observed that the latter limit value is achieved in the case of $n = 2$ (linear inclusions, crack or stiffener), $\text{SRF}(n = 2, m) =$

¹ The concept of Stress Reduction Factor introduced here should not be confused with an analogous terminology used in rock mechanics [108] or in seismic engineering [125].

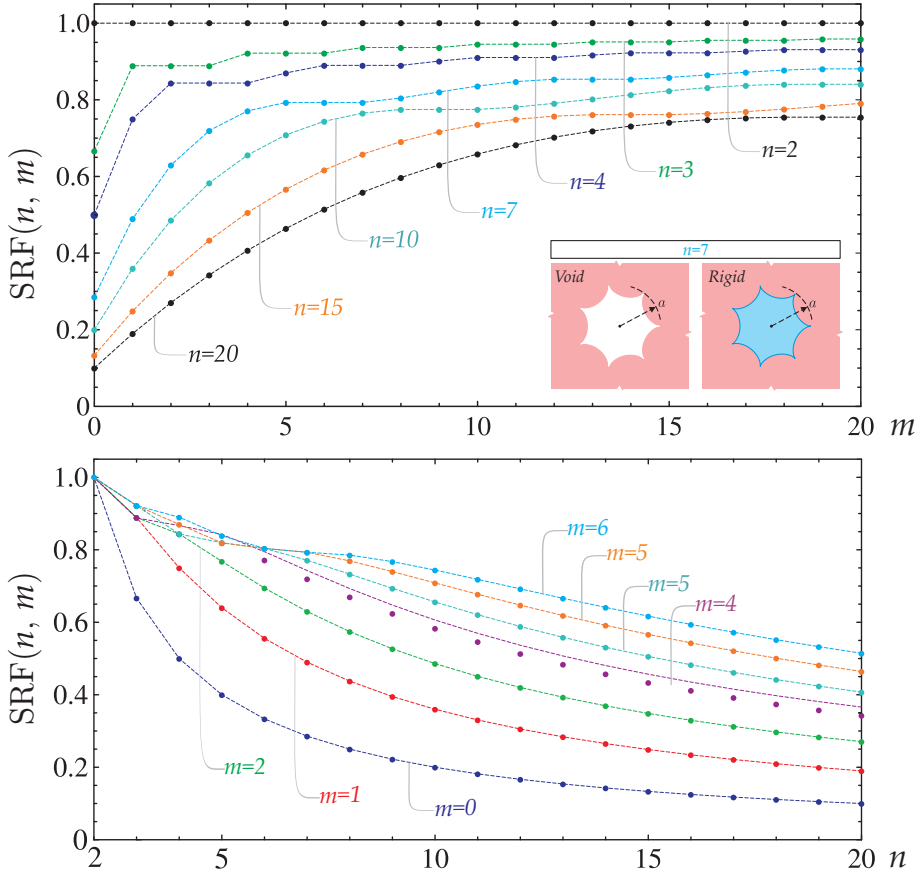


Figure 6.5: SRF reported as a function of the number n of cusps for a hypocycloidal void or a rigid inclusion, for different orders m of the applied remote polynomial out-of-plane shear loading. The graphs show the properties expressed by equations (6.29) and (6.30).

0, corresponding to the condition of inclusion invisibility or neutrality discussed in [116]. It is also worth to note that the annihilation condition related to $SRF=1$ also occurs for a different type of inclusions, namely, polygonal voids or rigid inclusions [116].

The following properties for the SRF have been numerically verified (while a rigorous proof seems to be awkward) to hold

$$\text{SRF}(n, m + 1) \leq \text{SRF}(n, m) \leq \text{SRF}(n + 1, m), \quad (6.29)$$

$$\text{SRF}(n, m = n) = \text{SRF}(n, m = n - 1) = \text{SRF}(n, m = n - 2). \quad (6.30)$$

Finally, singularities disappear, and therefore stress reduction occurs, at all cusps of an hypocycloidal inclusion, whenever the following condition is satisfied (for every $j \in \mathbb{N}_1$)

$$m = [3 - (-1)^n] \frac{jn}{4} - 1. \quad (6.31)$$

Dimensionless shear stress modulus $\tau^{(m)}(x_1, x_2)/\tau^{\infty(m)}(a, 0)$ level sets near rigid hypocycloidal inclusions $n = 3$ (upper part) and $n = 6$ (lower part) are reported in Fig. 6.1 for quadratic out-of-plane loading ($m = 2$). The figure highlights cases of stress singularity (left column, $c_0^{(m)} = 0$) and stress reduction (right column, $b_0^{(m)} = 0$). Stress reduction vs stress singularity is also depicted in Fig. 6.6, through the representation of the dimensionless shear stress modulus as a function of the distance from the cusp tip along the x_1 -axis, for the cases considered in Fig. 6.1. While the stress blows up to infinity as a square root singularity in the case of $c_0^{(m)} = 0$, the stress approaches a finite value, smaller than that unperturbed, in the case of $b_0^{(m)} = 0$.

Cases of *partial* stress reduction occur when stress reduction is verified at some cusps, but not at the other, namely, eq (6.23) holds while eq (6.31) does not. Examples of such cases are reported in Fig. 6.7 for rigid hypocycloidal inclusion with five and eight cusps. Uniform ($m = 0$) and quadratic ($m = 2$) out-of-plane shear loadings are applied. These cases feature cusps at which the stress falls to a value smaller than that would be attained at the same point in the absence of the inclusion, while stress singularities are still present at the other cusps.

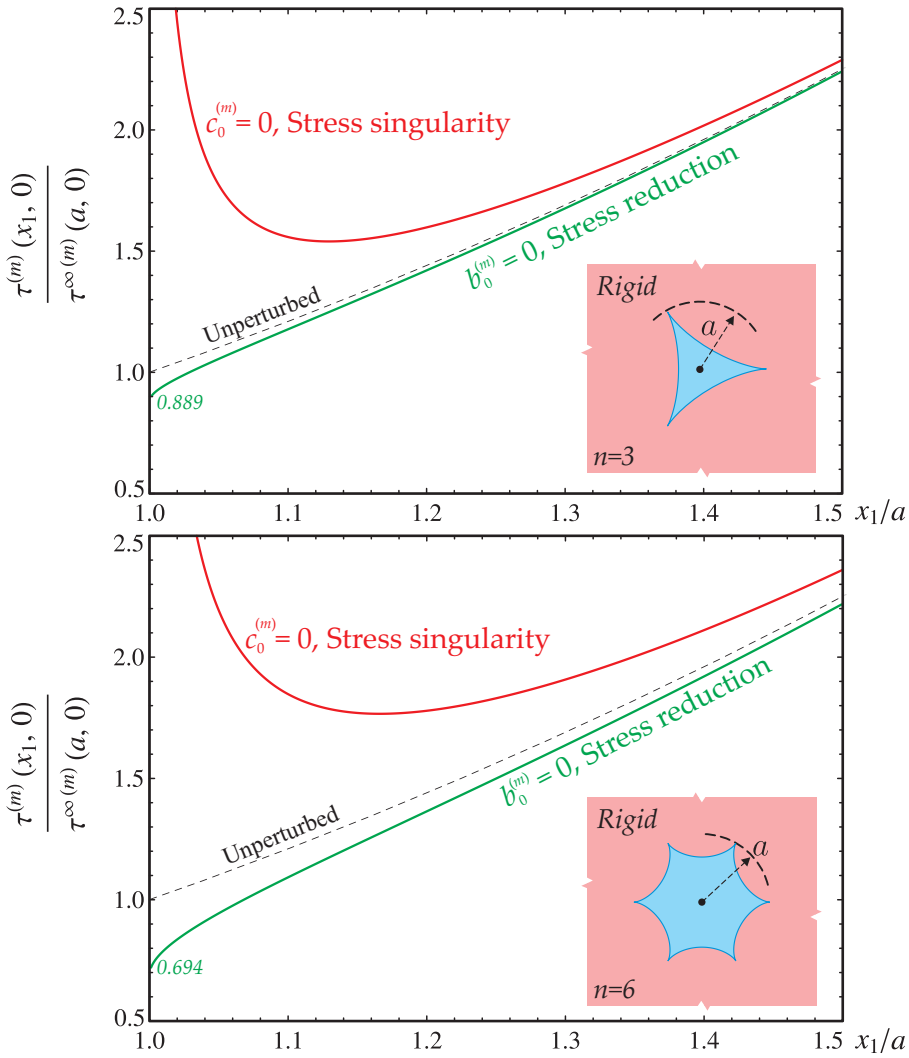


Figure 6.6: The shear stress modulus ahead of the cusp is reported as a function of the radial distance x_2 from the apex of three- and six- cusped hypocycloidal inclusions for quadratic ($m = 2$) remote out-of-plane shearing (the same case is considered in Fig. 6.1). Stress singularity and stress reduction are visible at the inclusion cusp for the two considered loading conditions, $c_0^{(m)} = 0$ and $b_0^{(m)} = 0$, respectively.

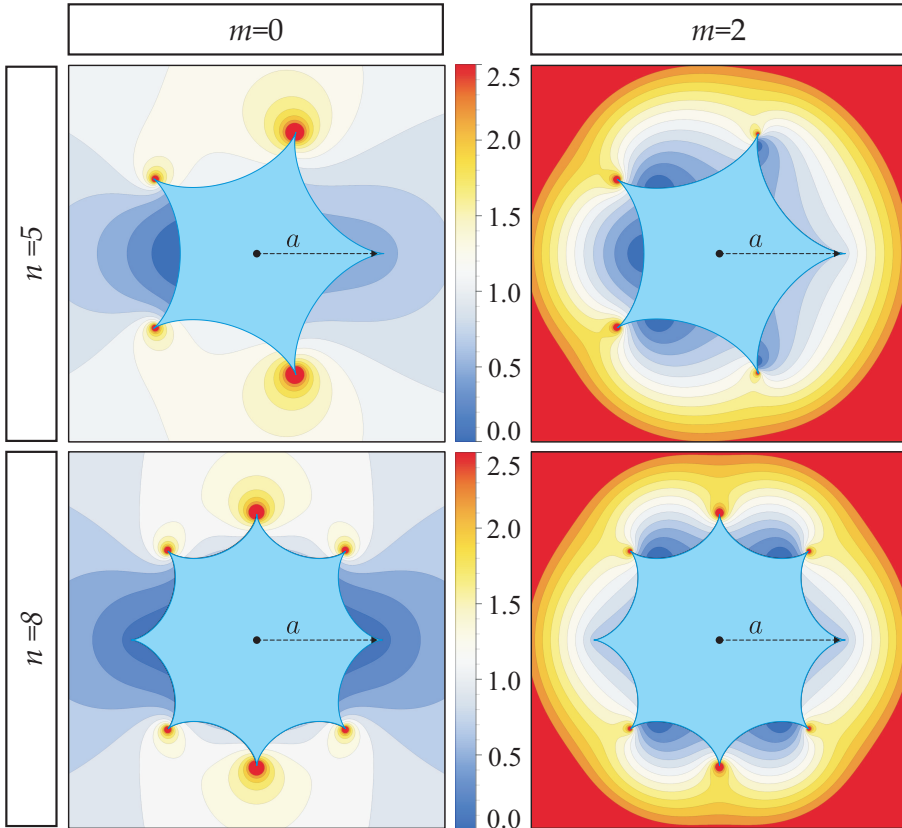


Figure 6.7: Level sets of dimensionless shear stress modulus $\tau^{(m)}(x_1, x_2)/\tau^{\infty(m)}(a, 0)$ near n -cusped rigid hypocycloidal inclusions ($n = 5$ and $n = 8$), subject to uniform ($m = 0$) and quadratic ($m = 2$) remote out-of-plane shearing ($b_0^{(m)} = 0$), show *partial* stress reduction, defined as the condition in which reduction occurs at some, but not all, of the inclusion vertices. When stress reduction occurs, the stress singularity is absent and the stress at the cusp is smaller than that which would be attained without any inclusion. In the figures a stress singularity corresponds to the appearance of ‘red spots’ at the inclusion cusp.

Appendix A

Fundamental equations in linear elasticity

When loading or displacements are prescribed, a solid deforms and is subject to a stress state. The kinematical and the statical fields are related each other through the constitutive relationship. Neglecting inelastic behaviour, the elasticity theory properly describes the material behaviour of a solid during a mechanical process. In the case that small deformations are involved and the material can be characterized by constant elastic properties, a simplified constitutive behaviour can be considered, the linear theory of elasticity, which is the linearization of the general theory of non-linear elasticity. This simplified constitutive model is still nowadays widely exploited to predict the stress state within solids, a fundamental concept in the failure analysis and the engineering design of materials.

A.1 Basic Formulas

Let's assume a fixed right-hand rectangular coordinate system $O-x_1x_2x_3$ and define the displacement vector from the initial to the final configuration $\underline{u}(\underline{x}) = [u_1(\underline{x}), u_2(\underline{x}), u_3(\underline{x})]$ of a generic point $\underline{x} = [x_1, x_2, x_3]$ of an elastic body. This kinematic quantity is fundamental to construct the

infinitesimal deformation tensor $\underline{\underline{\varepsilon}}$, which components are defined as

$$\varepsilon_{11} = \frac{\partial u_1}{\partial x_1}, \quad \varepsilon_{22} = \frac{\partial u_2}{\partial x_2}, \quad \varepsilon_{33} = \frac{\partial u_3}{\partial x_3}, \quad (\text{A.1})$$

as stretch strains and

$$\begin{aligned} \gamma_{12} &= \frac{1}{2}\varepsilon_{12} \\ &= \frac{1}{2} \left(\frac{\partial u_1}{\partial x_2} + \frac{\partial u_2}{\partial x_1} \right), \end{aligned} \quad (\text{A.2a})$$

$$\begin{aligned} \gamma_{13} &= \frac{1}{2}\varepsilon_{13} \\ &= \frac{1}{2} \left(\frac{\partial u_1}{\partial x_3} + \frac{\partial u_3}{\partial x_1} \right), \end{aligned} \quad (\text{A.2b})$$

$$\begin{aligned} \gamma_{23} &= \frac{1}{2}\varepsilon_{23} \\ &= \frac{1}{2} \left(\frac{\partial u_2}{\partial x_3} + \frac{\partial u_3}{\partial x_2} \right), \end{aligned} \quad (\text{A.2c})$$

as the shearing strains. From the static point of view, the stress tensor $\underline{\underline{\sigma}}$ can be defined as work-conjugate to the deformation tensor $\underline{\underline{\varepsilon}}$ and must satisfy the equilibrium equations, which, in the case of null body-forces, are given by

$$\begin{cases} \frac{\partial \sigma_{11}}{\partial x_1} + \frac{\partial \sigma_{12}}{\partial x_2} + \frac{\partial \sigma_{13}}{\partial x_3} = 0, \\ \frac{\partial \sigma_{21}}{\partial x_1} + \frac{\partial \sigma_{22}}{\partial x_2} + \frac{\partial \sigma_{23}}{\partial x_3} = 0, \\ \frac{\partial \sigma_{31}}{\partial x_1} + \frac{\partial \sigma_{32}}{\partial x_2} + \frac{\partial \sigma_{33}}{\partial x_3} = 0. \end{cases} \quad (\text{A.3})$$

Note that, both deformation and stress tensor results to be symmetric, therefore

$$\begin{aligned} \varepsilon_{12} &= \varepsilon_{21}, & \varepsilon_{23} &= \varepsilon_{32}, & \varepsilon_{13} &= \varepsilon_{31}, \\ \sigma_{12} &= \sigma_{21}, & \sigma_{23} &= \sigma_{32}, & \sigma_{13} &= \sigma_{31}. \end{aligned} \quad (\text{A.4})$$

Moreover a traction vector \underline{t} for a plane defined by the normal \underline{n} is given as follows

$$\underline{t} = \underline{\sigma} \cdot \underline{n}. \quad (\text{A.5})$$

In linear theory of elasticity, the fundamental Hooke's law states that the deformations are linear functions of the stresses and vice versa. In the following paragraphs constitutive laws in linear elasticity are reported.

A.1.1 Direct constitutive law

For linear elastic and isotropic material the direct constitutive law is given in the following form

$$\underline{\underline{\sigma}} = \lambda \text{tr}(\underline{\underline{\varepsilon}}) \underline{\underline{I}} + 2\mu \underline{\underline{\varepsilon}}, \quad (\text{A.6})$$

where λ and μ are Lamé's constants, while $\underline{\underline{I}}$ is an identity matrix and $\text{tr}(\underline{\underline{\varepsilon}})$ represents the trace of the given tensor, as follows

$$\text{tr}(\underline{\underline{\varepsilon}}) = \varepsilon_{11} + \varepsilon_{22} + \varepsilon_{33}. \quad (\text{A.7})$$

Moreover equation (A.6) can be rewritten in function of Young's modulus E and Poisson's ratio ν in index notation, as

$$\sigma_{ij} = \frac{E}{1+\nu} \left[\sigma_{ij} + \frac{\nu}{1-2\nu} \varepsilon_{kk} \delta_{ij} \right]. \quad (\text{A.8})$$

Some useful relations among the elastic constants are given below

$$\left\{ \begin{array}{l} E = \frac{\mu(3\lambda + 2\mu)}{\lambda + \mu}, \\ \nu = \frac{\lambda}{2(\lambda + \mu)}, \\ \lambda = \frac{E\nu}{(1+\nu)(1-2\nu)}, \\ \mu = G = \frac{E}{2(1+\nu)}. \end{array} \right. \quad (\text{A.9})$$

For an elastic solid storing positive strain energy during a loading process, the following restrictions on the elastic constants hold

$$\lambda > -\frac{2}{3}\mu, \quad \mu > 0, \quad E > 0, \quad -1 \leq \nu \leq \frac{1}{2}. \quad (\text{A.10})$$

Note that a tensor $\underline{\underline{H}}$ can be decomposed in hydrostatic and deviatoric parts. This decomposition differs on the dimension of the tensor $\underline{\underline{H}}$, and is given below for the 3D and 2D cases,

$$\begin{cases} \underline{\underline{H}}^{(3D)} = \frac{1}{3} \text{tr}(\underline{\underline{H}}) \underline{\underline{I}} + \text{dev}_{(3D)}(\underline{\underline{H}}), \\ \underline{\underline{H}}^{(2D)} = \frac{1}{2} \text{tr}(\underline{\underline{H}}) \underline{\underline{I}} + \text{dev}_{(2D)}(\underline{\underline{H}}), \end{cases} \quad (\text{A.11})$$

from which the definition of the operator $\text{dev}(\cdot)$ in the 3D and 2D cases is evident.

So that rewriting equation (A.6) by separating into hydrostatic part (in function of bulk modulus K) and deviatoric part, as follows

$$\underline{\underline{\sigma}} = K \text{tr}(\underline{\underline{\varepsilon}}) \underline{\underline{I}} + 2\mu \text{dev}(\underline{\underline{\varepsilon}}), \quad (\text{A.12})$$

where K is a bulk modulus or Modulus of volume expansion and can be expressed by the following two cases (three-dimensional strain state and two-dimensional strain state) as

$$K^{(3D)} = \lambda + \frac{2}{3}\mu > 0, \quad K^{(2D)} = \lambda + \mu > 0. \quad (\text{A.13})$$

The following property on the bulk modulus for the 3D and 2D cases is observed

$$K^{(2D)} = K^{(3D)} + \frac{\mu}{3} > K^{(3D)}, \quad (\text{A.14})$$

which can be physically explained through the stiffening effects of the solid when a plane strain condition is considered.

For rubber like material ($\nu \rightarrow 1/2$), which means in-compressibility or no change in volume, then

$$K^{(3D)} \rightarrow \infty, \quad K^{(2D)} \rightarrow \infty. \quad (\text{A.15})$$

While for cork like material with $\nu \rightarrow 0$ which means no lateral contraction, so that

$$K^{(3D)} \rightarrow \frac{E}{3}, \quad K^{(2D)} \rightarrow \frac{E}{2}. \quad (\text{A.16})$$

A.1.2 Inverse constitutive law

For linear elastic and isotropic material the inverse constitutive law is given as follows

$$\underline{\underline{\varepsilon}} = \frac{1}{2\mu} \underline{\underline{\sigma}} - \frac{\lambda}{2\mu(3\lambda + 2\mu)} \text{tr}(\underline{\underline{\sigma}}) \underline{\underline{\mathbf{I}}}. \quad (\text{A.17})$$

Rewriting the above equation in function of E and ν , the following equation is obtained

$$\underline{\underline{\varepsilon}} = \frac{1}{E} [(1 + \nu) \underline{\underline{\sigma}} - \nu \text{tr}(\underline{\underline{\sigma}}) \underline{\underline{\mathbf{I}}}] . \quad (\text{A.18})$$

The inverse constitutive law in the index notation

$$\varepsilon_{ij} = \frac{1}{E} [(1 + \nu) \sigma_{ij} - \nu \sigma_{kk} \delta_{ij}] . \quad (\text{A.19})$$

A.2 Plane elasticity

There are two well known cases in the so-called in-plane elasticity: plane stress and plane strain problems.

A.2.1 Plane stress problem

Let's suppose a body in which two dimensions (transversal i.e. x_1 and x_2) are very large compared to the longitudinal one i.e. x_3 . The plane is made of linear elastic and isotropic material. Under the plane stress hypothesis we assume that the longitudinal stresses in the fibers to be null i.e. $\sigma_{33} = 0$ which doesn't implicate that $\varepsilon_{33} = 0$, thus

$$\begin{cases} \sigma_{33} = 0, \\ \varepsilon_{33} = -\frac{\lambda}{\lambda + 2\mu} (\varepsilon_{11} + \varepsilon_{22}). \end{cases} \quad (\text{A.20})$$

Stress field under plane-stress hypothesis

$$\begin{cases} \sigma_{11} = \frac{4\mu(\lambda + \mu)}{\lambda + 2\mu}\varepsilon_{11} + \frac{2\lambda\mu}{\lambda + 2\mu}\varepsilon_{22} = (\bar{\lambda} + 2\bar{\mu})\varepsilon_{11} + \bar{\lambda}\varepsilon_{22}, \\ \sigma_{22} = \frac{4\mu(\lambda + \mu)}{\lambda + 2\mu}\varepsilon_{22} + \frac{2\lambda\mu}{\lambda + 2\mu}\varepsilon_{11} = (\bar{\lambda} + 2\bar{\mu})\varepsilon_{22} + \bar{\lambda}\varepsilon_{11}, \\ \sigma_{12} = 2\mu\varepsilon_{12}, \\ \sigma_{33} = \sigma_{31} = \sigma_{32} = 0, \end{cases} \quad (\text{A.21})$$

where 3D elastic constants λ and μ are permuted into 2D elastic constants $\bar{\lambda}$ and $\bar{\mu}$ respectively following the hypothesis of plane stress.

$$\bar{\lambda} = \frac{2\mu}{\lambda + 2\mu}\lambda, \quad \bar{\mu} = \mu. \quad (\text{A.22})$$

Note that, $\bar{\lambda}$ is softer than λ (i.e. $\bar{\lambda} \leq \lambda$) when the values of Poisson's ratio satisfy positive interval $0 \leq \nu \leq 1/2$, whereas μ remains unchanged. Moreover it is possible to switch to plane strain by simply substituting $\bar{\lambda} = \lambda$ and $\bar{\mu} = \mu$ in equations (A.21).

Strain field under plane-stress hypothesis

$$\begin{cases} \varepsilon_{11} = \frac{1}{E} [\sigma_{11} - \nu\sigma_{22}], \\ \varepsilon_{22} = \frac{1}{E} [\sigma_{22} - \nu\sigma_{11}], \\ \varepsilon_{12} = \frac{1 + \nu}{E}\sigma_{12} = \frac{1}{2\mu}\sigma_{12}, \\ \varepsilon_{33} = -\frac{\nu}{E} [\sigma_{11} + \sigma_{22}] = -\frac{\lambda}{2\mu(3\lambda + 2\mu)} [\sigma_{11} + \sigma_{22}]. \end{cases} \quad (\text{A.23})$$

A.2.2 Plane strain problem

Let's suppose a body in which one dimension (longitudinal i.e. x_3) is very large compared to the others (transversal i.e. x_1 and x_2). The

cylinder is made of linear elastic and isotropic material. Under the plane strain hypothesis we assume that the longitudinal deformation of the fibers to be null i.e. $\varepsilon_{33} = 0$ which doesn't implicate that $\sigma_{33} = 0$, thus

$$\begin{cases} \varepsilon_{33} = 0, \\ \sigma_{33} = \nu(\sigma_{11} + \sigma_{22}) = \frac{\lambda}{2(\lambda + \mu)}(\sigma_{11} + \sigma_{22}). \end{cases} \quad (\text{A.24})$$

Stress field under plane-strain hypothesis

$$\begin{cases} \sigma_{11} = (\lambda + 2\mu)\varepsilon_{11} + \lambda\varepsilon_{22}, \\ \sigma_{22} = (\lambda + 2\mu)\varepsilon_{22} + \lambda\varepsilon_{11}, \\ \sigma_{12} = 2\mu\varepsilon_{12}, \\ \sigma_{33} = \lambda(\varepsilon_{22} + \varepsilon_{11}). \end{cases} \quad (\text{A.25})$$

Strain field under plane-strain hypothesis

$$\begin{cases} \varepsilon_{11} = \frac{1 - \nu^2}{E} \left[\sigma_{11} - \frac{\nu}{1 - \nu} \sigma_{22} \right] = \frac{1}{\bar{E}} [\sigma_{11} - \bar{\nu} \sigma_{22}], \\ \varepsilon_{22} = \frac{1 - \nu^2}{E} \left[\sigma_{22} - \frac{\nu}{1 - \nu} \sigma_{11} \right] = \frac{1}{\bar{E}} [\sigma_{22} - \bar{\nu} \sigma_{11}], \\ \varepsilon_{12} = \frac{1 + \nu}{E} \sigma_{12} = \frac{1}{2\mu} \sigma_{12}, \\ \varepsilon_{33} = \varepsilon_{31} = \varepsilon_{32} = 0, \end{cases} \quad (\text{A.26})$$

where 3D elastic constants E and ν are permuted into 2D elastic constants \bar{E} and $\bar{\nu}$ respectively. The latter constants are also called stiffened elastic constants, because they are stiffer than the former ones, as follows

$$\begin{cases} \bar{E} = \frac{E}{1 - \nu^2} = \frac{4\mu(\lambda + \mu)}{\lambda + 2\mu} \geq E, \\ \bar{\nu} = \frac{\nu}{1 - \nu} = \frac{\lambda}{\lambda + 2\mu}. \end{cases} \quad (\text{A.27})$$

Note that, $\bar{\nu}$ is stiffer than ν (i.e. $\bar{\nu} \geq \nu$) when the values of Poisson's ratio satisfy the positive interval $0 \leq \nu \leq 1/2$, while \bar{E} remains stiffer for whole interval of ν . Further it is possible to switch to plane stress by simply substituting $\bar{E} = E$ and $\bar{\nu} = \nu$ in equations (A.26).

A.2.3 A general stress-strain relationship in in-plane elasticity

It is possible to write the two-dimensional stress-strain relations in alternative and an elegant form [13], as follows

$$\begin{cases} \varepsilon_{11} = \frac{(\kappa + 1)\sigma_{11} + (\kappa - 3)\sigma_{22}}{8\mu}, \\ \varepsilon_{22} = \frac{(\kappa + 1)\sigma_{22} + (\kappa - 3)\sigma_{11}}{8\mu}, \\ \varepsilon_{12} = \frac{\sigma_{12}}{2\mu}, \end{cases} \quad (\text{A.28})$$

where constant κ expressed by the Poisson's ratio which distinguishes the plane stress from plane strain is defined as follows

$$\kappa := \begin{cases} \frac{3 - \nu}{1 + \nu} & \text{for plane stress,} \\ 3 - 4\nu & \text{for plane strain.} \end{cases} \quad (\text{A.29})$$

Note that, by substituting 3D Poisson's ratio ν with 2D stiffened value $\bar{\nu} = \nu(1 - \nu)$ into equation (A.29)₁, so that equation (A.29)₂ is obtained.

Appendix B

Some theorems in complex analysis with related examples

B.1 Cauchy Residue Theorem

Let $f(\sigma)$ be analytic inside and on a simple closed contour γ , e.g. a unit circle, except some finite number of isolated singular points σ_j ($j \in \mathbb{N}$), located inside γ , as given by [10]

$$\left\{ \begin{array}{l} \frac{1}{2\pi i} \oint_{\gamma} f(\sigma) d\sigma = \sum_{j=1}^n \text{Res}(f; \sigma_j), \\ f(\sigma) = \frac{f^*(\sigma)}{(\sigma - \sigma_j)^n}, \end{array} \right. \quad (\text{B.1})$$

where function $f(\sigma)$ has n -th order pole, in particular when $n = 0$, then the pole is denominated as a simple pole. While function $f^*(\sigma)$ is analytic in the neighborhood of the given pole, so that the residue

$$\text{Res}(f; \sigma_j) = \frac{1}{(n-1)!} \lim_{\sigma \rightarrow \sigma_j} \left[\frac{d^{n-1}}{d\sigma^{n-1}} f^*(\sigma) \right]. \quad (\text{B.2})$$

Example 1: Cauchy Residue Theorem

A complex function analytic inside the unit circle ($|\zeta| < 1$) except three poles lying inside the given circle, is given by

$$f(\sigma) = \frac{\sigma^3 + 1}{\sigma(\sigma - \frac{1}{2})^3(\sigma - \zeta)}, \tag{B.3}$$

in particular, two simple poles at the points 0 and ζ , and a third order pole at the point $1/2$, then using equation (B.2), one can easily obtain

$$\begin{aligned} \frac{1}{2\pi i} \oint_{|\gamma|=1} \frac{\sigma^3 + 1}{\sigma(\sigma - \frac{1}{2})^3(\sigma - \zeta)} d\sigma &= \text{Res}(f; 0) + \text{Res}(f; \zeta) + \text{Res}\left(f; \frac{1}{2}\right) \\ &= 0. \end{aligned} \tag{B.4}$$

as all three residues calculated through (B.2) are summarized underneath

$$\left\{ \begin{aligned} \text{Res}(f; 0) &= \frac{8}{\zeta}, \\ \text{Res}(f; \zeta) &= \frac{\zeta^3 + 1}{(\zeta - \frac{1}{2})^3 \zeta}, \\ \text{Res}\left(f; \frac{1}{2}\right) &= \frac{1}{2} \left(\frac{6}{(\frac{1}{2} - \zeta)^2} + \frac{9}{2(\frac{1}{2} - \zeta)^3} + \frac{18}{\frac{1}{2} - \zeta} \right). \end{aligned} \right. \tag{B.5}$$

Note that, poles that occurs outside the unit circle, in our case, become the part of the function $f^*(\sigma)$.

Example 2: Cauchy Residue Theorem

A complex function analytic inside a unit circle ($|\zeta| < 1$) except some isolated singular points

$$f(\sigma) = \frac{\sigma(m\sigma^2 + 1)}{(\sigma - \zeta)(m - \sigma^2)} \tag{B.6}$$

has three poles inside inside the given circle, in particular, one simple pole at ζ and two simple poles at $\sigma = \pm\sqrt{m}$ with the value of parameter

varying inside the interval $0 \leq m < 1$. Equation (B.6) can be rewritten in order to highlight the three poles, so that

$$\begin{aligned} f(\sigma) &= -\frac{\sigma(m\sigma^2 + 1)}{(\sigma - \zeta)(\sigma^2 - m)} \\ &= -\frac{\sigma(m\sigma^2 + 1)}{(\sigma - \zeta)(\sigma - \sqrt{m})(\sigma + \sqrt{m})}. \end{aligned} \tag{B.7}$$

Through equation (B.2) one can easily obtain the following

$$\frac{1}{2\pi i} \oint_{|\gamma|=1} \frac{-\sigma(m\sigma^2 + 1)}{(\sigma - \sqrt{m})(\sigma + \sqrt{m})(\sigma - \zeta)} d\sigma = -m\zeta, \tag{B.8}$$

given the residues summarized beneath

$$\left\{ \begin{aligned} \text{Res}(f; \sqrt{m}) &= -\frac{m^2 + 1}{2(\sqrt{m} - \zeta)} \\ \text{Res}(f; -\sqrt{m}) &= -\frac{m^2 + 1}{2(-\zeta - \sqrt{m})} \\ \text{Res}(f; \zeta) &= \frac{\zeta + \zeta^3 m}{m - \zeta^2} \end{aligned} \right. \tag{B.9}$$

Note that the well-known formula for a unit disc [4]

$$\frac{1}{2\pi i} \oint_{|\gamma|=1} \frac{d\sigma}{\sigma^p(\sigma - \zeta)} = \begin{cases} 1 & \text{if } p = 0 \\ 0 & \text{if } p > 0 \end{cases} \tag{B.10}$$

can be immediately verified through residue theorem, as follows

- $p = 0$

$$\begin{aligned} \frac{1}{2\pi i} \oint_{|\gamma|=1} \frac{d\sigma}{(\sigma - \zeta)} &= \text{Res}(f; \zeta) \\ &= 1. \end{aligned} \tag{B.11}$$

- $p = 1$

$$\begin{aligned}
 & \frac{1}{2\pi i} \oint_{|\gamma|=1} \frac{d\sigma}{\sigma(\sigma - \zeta)} \\
 &= \operatorname{Res}(f; 0) + \operatorname{Res}(f; \zeta) \\
 &= -\frac{1}{\zeta} + \frac{1}{\zeta} \\
 &= 0.
 \end{aligned} \tag{B.12}$$

- $p = 2$

$$\begin{aligned}
 & \frac{1}{2\pi i} \oint_{|\gamma|=1} \frac{d\sigma}{\sigma^2(\sigma - \zeta)} \\
 &= \operatorname{Res}(f; 0) + \operatorname{Res}(f; \zeta) \\
 &= -\frac{1}{\zeta^2} + \frac{1}{\zeta^2} \\
 &= 0.
 \end{aligned} \tag{B.13}$$

It is noteworthy that, for the case $p = 2$, the pole in the point 0 is of the order 2 and therefore it is necessary to apply the formula B.2.

B.2 Cauchy Integral Formula

Let's consider a domain bounded by the unit circle of contour γ . The region inside and outside γ is denoted by D^+ and D^- respectively. So that a complex function $f(\sigma)$ analytic in D^+ and continuous in $D^+ + \gamma$, except some points σ_j ($j = 1, 2, \dots, k \in \mathbb{N}$) of D^+ , where it may have poles with the principal parts $g_j(\zeta)$ ($j = 1, 2, \dots, k$), as given by [11]

$$\left\{ \begin{aligned}
 & \frac{1}{2\pi i} \oint_{|\gamma|=1} f(\sigma) \frac{d\sigma}{\sigma - \zeta} = f(\zeta) - \sum_{j=1}^k g_j(\zeta), \quad \text{if } \zeta \in D^+ \\
 & \frac{1}{2\pi i} \oint_{|\gamma|=1} f(\sigma) \frac{d\sigma}{\sigma - \zeta} = -\sum_{j=1}^k g_j(\zeta). \quad \text{if } \zeta \in D^-
 \end{aligned} \right. \tag{B.14}$$

A complex function $f(\sigma)$ can be represented by

$$f(\sigma) = \frac{f^*(\sigma)}{(\sigma - \sigma_j)^n}, \tag{B.15}$$

where function $f^*(\sigma)$ is analytic in the neighborhood of the given pole and n represents the order of the pole.

So that the principal part $g_j(\zeta)$ of the Laurent series expansion around the pole can be expressed by the following expression

$$g_j(\zeta) = \lim_{\sigma \rightarrow \sigma_j} \left[\sum_{i=0}^{n-1} \frac{1}{i! (\zeta - \sigma_j)^{n-i}} f^{*(i)}(\sigma) \right] \tag{B.16}$$

where apex $^{(i)}$ is intended as the i -th derivative with respect to the variable σ of the given function $f^*(\sigma)$.

Example 1: Cauchy Integral Formula

A complex function analytic inside a unit circle D^+ except some singular points is given as follows

$$f(\sigma) = \frac{\sigma^3 + 1}{\sigma(\sigma - \frac{1}{2})^3}. \tag{B.17}$$

The function above has two poles, in particular, one simple pole at 0 and a 3rd order pole at $1/2$ lying inside D^+ . Through equation (B.16) the desired result is obtained, as

$$\begin{aligned} \frac{1}{2\pi i} \oint_{|\gamma|=1} \frac{\sigma^3 + 1}{\sigma(\sigma - \frac{1}{2})^3} \frac{d\sigma}{(\sigma - \zeta)} &= \frac{\zeta^3 + 1}{\zeta(\zeta - \frac{1}{2})^3} - \sum_{j=1}^2 g_j(\zeta) \\ &= 0, \end{aligned} \tag{B.18}$$

given the principal part through Laurent series expansion equation (B.16)

$$\begin{cases} g_1(\zeta) = -\frac{8}{\zeta}, \\ g_2(\zeta) = \frac{9}{4(\zeta - \frac{1}{2})^3} - \frac{3}{(\zeta - \frac{1}{2})^2} + \frac{9}{\zeta - \frac{1}{2}}. \end{cases} \tag{B.19}$$

Note that, the result provided by (B.18) coincide with the result given by (B.4) obtained via Cauchy Residue Theorem, as expected.

Example 2: Cauchy Integral Formula

An complex function analytic inside a unit circle D^+ except some isolated singular points

$$\begin{aligned} f(\sigma) &= \frac{\sigma (m\sigma^2 + 1)}{(m - \sigma^2)} \\ &= -\frac{\sigma (m\sigma^2 + 1)}{(\sigma - \sqrt{m})(\sigma + \sqrt{m})} \end{aligned} \quad (\text{B.20})$$

has three poles in D^+ , in particular, one simple pole at ζ and two simple poles at $\sigma = \pm\sqrt{m}$ with the value of parameter varying inside the interval $0 \leq m < 1$. So that

$$\begin{aligned} \frac{1}{2\pi i} \oint_{|\gamma|=1} \frac{f(\sigma)}{\sigma - \zeta} d\sigma &= \frac{-\zeta (m\zeta^2 + 1)}{(\zeta - \sqrt{m})(\zeta + \sqrt{m})} - \sum_{j=1}^2 g_j(\zeta) \\ &= -m\zeta, \end{aligned} \quad (\text{B.21})$$

as the principal parts given through equation (B.16) are summarized as

$$\begin{cases} g_1(\zeta) = \frac{-m^2 - 1}{2(\zeta - \sqrt{m})}, \\ g_1(\zeta) = \frac{-m^2 - 1}{2(\zeta + \sqrt{m})}. \end{cases} \quad (\text{B.22})$$

Note that, the result provided by (B.21) coincide with the result given by (B.8) obtained via Cauchy Residue Theorem, as expected.

Bibliography

- [1] Slaughter, W.S., 2002. The linearized theory of elasticity. Birkhäuser.
- [2] Chen, Y.Z., Hasebe, N., and Lee, K.Y., 2003. Multiple crack problems in elasticity. WIT press.
- [3] Janssen, M., Zuidema, J, Wanhill, R.J.H., 2004. Fracture mechanics, second Edition, Spon Press.
- [4] Sokolnikoff I.S., 1956. Mathematical theory of elasticity, McGraw-Hill.
- [5] Edouard G., 19516. A Course in mathematical analysis functions of a complex Variable, being part I of volume II, vol. 2, Ginn and Company.
- [6] Ivanov, V.I., Trubetskov, M.K., 1994. Handbook of Conformal Mapping with Computer-Aided Visualization. CRC Press.
- [7] Liebowitz, H., 1968. Fracture : an advanced treatise. Vol. II, mathematical fundamentals. Academic Press.
- [8] Murakami, Y., 1987. Stress Intensity Factors Handbook. Vol. I, Pergamon Press.
- [9] Murakami, Y., 1987. Stress Intensity Factors Handbook. Vol. II, Pergamon Press.
- [10] Ablowitz M. J., Fokas A. S. (2003) *Complex Variables: Introduction and Applications*, Cambridge University Press.

- [11] Muskhelishvili, N.I., 1953. Some Basic Problems of the Mathematical Theory of Elasticity. P. Nordhoff Ltd., Groningen.
- [12] Stein A. B., Dag L., Annette M. and Leon S., Narvik, 2003. Some methods for calculating stiffness properties of periodic structures, Applications of Mathematics 2, 97-110.
- [13] Barber, J.R., 2004. Elasticity, Kluwer. Evaluation of the effective elastic and conductive properties of a material containing concave pores. Int. J. Eng. Sci., 97, 60-68.
- [14] Bigoni, D., 2012. Nonlinear Solid Mechanics. Bifurcation Theory and Material Instability. Cambridge University Press.
- [15] Chang and Conway, 1968. A parametric study of the complex variable method for analyzing the stresses in an infinite plate containing a rigid rectangular inclusion. Int. J. Solid Struct. 4, 11, 1057-66.
- [16] Dal Corso, F. and Bigoni, D., 2009. The interactions between shear bands and rigid lamellar inclusions in a ductile metal matrix. Proc. R. Soc. A 465, 143-163.
- [17] Dal Corso, F. and Bigoni, D., 2010. Growth of slip surfaces and line inclusions along shear bands in a softening material. Int. J. Fract., 166, 225-237.
- [18] Dal Corso, F., Bigoni, D. and Gei, M., 2008. The stress concentration near a rigid line inclusion in a prestressed, elastic material. Part I. Full field solution and asymptotics. J. Mech. Phys. Solids 56, 815-838.
- [19] Dally, J.W. and Riley W.F., 1965. Experimental stress analysis. McGraw-Hill.
- [20] Dundurs, J., 1989. Cavities vis-a-vis rigid inclusions and some related general results in plane elasticity. J. Appl. Mech. 56, 786-790.
- [21] Evan-Iwanowski, R.M., 1956. Stress solutions for an infinite plate with triangular inlay. J. Appl. Mech. 23, 336.
- [22] Frocht, M.M., 1965. Photoelasticity. J. Wiley and Sons, London.

- [23] Gdoutos, E.E., 1982. Photoelastic analysis of the stress field around cuspidal points of rigid inclusions. *J. Appl. Mech.* 49, 236-238.
- [24] Ishikawa H., Kohno Y., 1993. Analysis of stress singularities at the corner point of square hole and rigid square inclusion in elastic plates by conformal mapping, *Int. J. Engng. Scie.* 31, 1197-1213.
- [25] Kohno Y., Ishikawa H., 1994. Analysis of stress singularities at the corner point of lozenge hole and rigid lozenge inclusion in elastic plates by conformal mapping. *Int. J. Engng. Scie.* 32, 1749–1768.
- [26] Movchan, A.B. and Movchan, N.V., 1995. *Mathematical Modeling of Solids with Nonregular Boundaries*, CRC Press.
- [27] Noselli, G., Dal Corso, F. and Bigoni, D., 2010. The stress intensity near a stiffener disclosed by photoelasticity. *Int. J. Fract.* 166, 91–103.
- [28] Piccolroaz, A., Mishuris, G., Movchan, A., and Movchan, N., 2012. Perturbation analysis of Mode III interfacial cracks advancing in a dilute heterogeneous material. *Int. J. Solid Struct.* 49, 244-255.
- [29] Piccolroaz, A., Mishuris, G., Movchan, A., and Movchan, N., 2012. Mode III crack propagation in a bimaterial plane driven by a channel of small line defects. *Comput. Materials Sci.* 64, 239-243.
- [30] Lim, J. and Ravi-Chandar K., 2007. Photomechanics in dynamic fracture and friction studies. *Strain* 43, 151-165.
- [31] Lim, J. and Ravi-Chandar, K., 2009. Dynamic Measurement of Two Dimensional Stress Components in Birefringent Materials. *Exper. Mech.* 49, 403-416.
- [32] Panasyuk V.V., Berezhnitskii L.T., Trush I.I., 1972. Stress distribution about defects such as rigid sharp-angled inclusions, *Problemy Prochnosti*, 7, 3-9.
- [33] Reedy, E.D. and Guess, T.R., 2001. Rigid square inclusion embedded within an epoxy disk: asymptotic stress analysis. *Int. J. Solid Struct.* 38, 1281-1293.

- [34] Rosakis, A.J. and Zehnder, A.T., 1985. On the method of caustics: An exact analysis based on geometrical optics, *J. Elasticity* 15, 347-367.
- [35] Schubnel, A., Nielsen, S., Taddeucci, J., Vinciguerra, S. and Rao, S., 2011. Photo-acoustic study of subshear and supershear ruptures in the laboratory, *Earth Planetary Sci. Letters* 308, 424-432.
- [36] Seweryn, A., Molski, K., 1996. Elastic stress singularities and corresponding generalized stress intensity factors for angular corners under various boundary conditions. *Eng. Fract. Mech.* 55, 529-556.
- [37] Templeton, E. L., Baudet, A., Bhat, H.S., Dmowska, R., Rice, J.R., Rosakis, A.J. and Rousseau, C.-E., 2009. Finite element simulations of dynamic shear rupture experiments and dynamic path selection along kinked and branched faults, *J. Geophys. Res.* 114, B08304.
- [38] Theocaris, P.S., 1975 Stress and displacement singularities near corners. *J. Appl. Math. Phys. (ZAMP)* 26, 77-98.
- [39] Theocaris, P.S., Paipetis S.A., 1976a. State of stress around inhomogeneities by the method of caustics. *Fibre Science and Technology* 9, 19-39.
- [40] Theocaris, P.S., Paipetis S.A., 1976b. Constrained zones at singular points of inclusion contours. *Int. J. Mech. Scie.* 18, 581-587.
- [41] M. Valentini, S.K. Serkov, D. Bigoni and A.B. Movchan, 1999. Crack propagation in a brittle elastic material with defects. *J. Appl. Mech.* 66, 79-86.
- [42] Williams M.L. 1952. Stress singularities resulting from various boundary conditions in angular corners of plates in extension. *J. Appl. Mech.* 19, 526-528.
- [43] Andersson, H., 1969. Stress-intensity factors at the tips of a star-shaped contour in an infinite tensile sheet. *J. Mech. Phys. Solids* 17, 5, 405-406.

- [44] Abramowitz, M., Stegun, I.A., 1972. Handbook of Mathematical Functions with Formulas, Graphs, and Mathematical Tables. Wiley-Interscience, NY.
- [45] Bacca, M., Dal Corso, F., Veber, D. and Bigoni, D., 2013. Anisotropic effective higher-order response of heterogeneous Cauchy elastic materials. *Mec. Res. Comm.* , 54, 63-71.
- [46] Barbieri, E., Pugno, N.M., 2015. A computational model for large deformations of composites with a 2D soft matrix and 1D anticracks. *Int. J. Solid Struct.*77, 1-14.
- [47] Bigoni, D., Drugan, W.J., 2007. Analytical derivation of Cosserat moduli via homogenization of heterogeneous elastic materials. *J. Appl. Mech.* 74, 1-13.
- [48] Chen, J., 2012. Indentation-based methods to assess fracture toughness for thin coatings. *J. Phys. D: Appl. Phys.* 45, 203001.
- [49] Chen, F., Sevostianov, I., Girauda, A., Grgic, D., 2015. Evaluation of the effective elastic and conductive properties of a material containing concave pores. *Int. J. Eng. Sci.*, 97, 60-68.
- [50] Seagraves, A.N., Radovitzky, R.A., 2013. An analytical theory for Radial crack propagation: application to spherical indentation. *J. Appl. Mech.* 80, 1-5.
- [51] Rassoulova, N.B., 2010. The propagation of star-shaped brittle cracks. *J. Appl. Mech.* 77, 1-5.
- [52] Coxeter, H.S.M., 1989. Introduction to geometry. John Willey and Sons, NY.
- [53] Das, S.C., 1953. On the stresses due to a small spherical inclusion in a uniform beam under constant bending moment. *Bull. Calcutta Math. Soc.* 45, 55-63.
- [54] Eshelby, J.D., 1957. The Determination of the Elastic Field of an Ellipsoidal Inclusion and Related Problems. *Proc. R. Soc. A* 241, 376-396.

- [55] Gauthier, G., Lazarus, V., Pauchard, L., 2010. Shrinkage star-shaped cracks: Explaining the transition from 90 degrees to 120 degrees. *EPL* 89, 26002.
- [56] Gupta, M., Alderliesten, R.C., Benedictus, R., 2015. A review of T-stress and its effects in fracture mechanics. *Eng. Fract. Mech.* 134, 218-241.
- [57] Grunbaum, B., Shephard, G.C., 1987. *Tilings and Patterns*. W.H. Freeman and Company, NY.
- [58] Maurini, C., Bourdin, B., Gauthier, G., Lazarus, V., 2013. Crack patterns obtained by unidirectional drying of a colloidal suspension in a capillary tube: experiments and numerical simulations using a two-dimensional variational approach. *Int. J. Fract.* 184, 75-91.
- [59] Misseroni, D., Dal Corso, F., Shahzad, S., Bigoni, D., 2014. Stress concentration near stiff inclusions: Validation of rigid inclusion model and boundary layers by means of photoelasticity. *Eng. Fract. Mech.* 121-122, 87-97.
- [60] Noselli, G., Dal Corso, F. and Bigoni, D., 2010. The stress intensity near a stiffener disclosed by photoelasticity. *Int. J. Fract.* 166, 91-103.
- [61] Moon, H.J., Earmme, Y.Y., 1998. Calculation of elastic T-stresses near interface crack tip under in-plane and anti-plane loading. *Int. J. Fract.* 91, 179-195.
- [62] Radaj, D., 2013. State-of-the-art review on extended stress intensity factor concepts. *Fatigue Fract. Eng. Mat. Str.* 37, 1-28.
- [63] Movchan, A.B., Movchan, N.V., 1995. *Mathematical Modelling of Solids with Nonregular Boundaries*. CRC Press.
- [64] Movchan, A.B., Movchan, N.V., Poulton, C.G., 2002. *Asymptotic Models of Fields in Dilute and Densely Packed Composites*. Imperial College Press.

-
- [65] Olver, F.W.J., Lozier, D.W., Boisvert, R.F., Clark, C.W., 2010. NIST Handbook of Mathematical Functions. Cambridge University Press, NY.
- [66] Piccolroaz, A., Mishuris, G., Movchan, A.B., 2010. Perturbation of Mode III interfacial cracks. *Int. J. Fract.* 166, 41-51.
- [67] Piccolroaz, A., Mishuris, G., Movchan, A.B., 2009. Symmetric and skew-symmetric weight functions in 2D perturbation models for semi-infinite interfacial cracks. *J. Mech. Phys. Solids* 57, 1657-1682.
- [68] Piccolroaz, A., Mishuris, G., Movchan, A., Movchan, N., 2012. Perturbation analysis of Mode III interfacial cracks advancing in a dilute heterogeneous material. *Int. J. Solid Struct.* 49, 244-255.
- [69] Morini, L., Piccolroaz, A., Mishuris, G., Radi, E., 2013. Integral identities for a semi-infinite interfacial crack in anisotropic elastic bimetals. *Int. J. Solid Struct.* 50, 1437-1448.
- [70] Piccolroaz, A. and Mishuris, G., 2013. Integral identities for a semi-infinite interfacial crack in 2D and 3D elasticity. *J. Elasticity* , 110, 117-140.
- [71] Schiavone, P., 2003. Neutrality of the elliptic inhomogeneity in the case of non-uniform loading. *Int. J. Eng. Sci.* 8, 161-169.
- [72] Savin, G.N., 1961. Stress concentration around holes. Pergamon Press.
- [73] Sen, B., 1933. On the Concentration of Stresses Due to a Small Spherical Cavity in a Uniform Beam Bent by Terminal Couples. *Bull. Calcutta Math. Soc.* 25, 107-114.
- [74] Sih, G.C., 1965. Stress Distribution Near Internal Crack Tips for Longitudinal Shear Problems. *J. Appl. Mech.* 32, 51-58.
- [75] Seweryn, A., Molski, K., 1996. Elastic stress singularities and corresponding generalized stress intensity factors for angular corners under various boundary conditions. *Eng. Fract. Mech.* 55, 529-556.

- [76] Driscoll, T.A., Trefethen, L.N., 2002. Schwarz-Christoffel Mapping. Cambridge University Press.
- [77] Vandenberghe, N., Vermorel, R., Villermaux, E., 2013. Star-shaped crack pattern of broken windows. *Phys. Rev. Lett.*110, 174302.
- [78] Van Vliet, D., Schiavone, P., Mioduchowski, A., 2003. On the Design of Neutral Elastic Inhomogeneities in the Case of Non-Uniform Loading. *Math. Mech. Solids* 41, 2081-2090.
- [79] Vasudevan, M., Schiavone, P., 2006. New results concerning the identification of neutral inhomogeneities in plane elasticity. *Arch. Mechanics* 58, 45-58.
- [80] Anderson, T.L., 2005. Fracture Mechanics: Fundamentals and Applications. CRC Press, Taylor and Francis.
- [81] Benveniste, Y., Miloh, T., 2007. Soft neutral elastic inhomogeneities with membrane-type interface conditions. *J. Elasticity* 88, 87-111.
- [82] Bertoldi, K., Bigoni, D., Drugan, W.J., 2007. Structural interfaces in linear elasticity. Part II: Effective properties and neutrality. *J. Mech. Phys. Solids* 55, 35-63.
- [83] Bigoni, D., Serkov, S.K., Movchan, A.B., Valentini, M., 1998. Asymptotic models of dilute composites with imperfectly bonded inclusions. *Int. J. Solid Struct.* 35, 3239-3258
- [84] Brun, M., Colquitt, D.J., Jones, I.S., Movchan, A.B., Movchan, N.V., 2014. Transformation cloaking and radial approximations for flexural waves in elastic plates. *New J. Physics* 16, 093020.
- [85] Brun, M., Guenneau, S., Movchan, A.B., 2009. Achieving control of in-plane elastic waves. *Appl. Phys. Letters* 94, 061903.
- [86] Christensen, R.M., 1979. Mechanics of composite materials. Wiley.
- [87] Colquitt, D.J., Jones, I.S., Movchan, N.V., Brun, M., McPhedran, R.C., 2013. Making waves round a structured cloak: lattices, negative refraction and fringes. *Proc. R. Soc. A* 469, 20130218.

- [88] Farhat, M., Guenneau, S., Enoch, S., 2009. Ultrabroadband elastic cloaking in thin plates. *Phys. Rev. Lett.* 103, 024301.
- [89] Milton, G.W., 2007. New metamaterials with macroscopic behavior outside that of continuum elastodynamics. *New J. Phys.* 9, 359.
- [90] Kohno Y. Ishikawa H., 1995. Singularities and stress intensities at the corner point of a polygonal hole and rigid polygonal inclusion under antiplane shear. *Int. J. Eng. Sci.* 33, 1547-1560.
- [91] Mahboob, M., Schiavone, P., 2005. Designing a neutral elliptic inhomogeneity in the case of a general non-uniform loading. *Appl. Math. Letters* 18, 1312-1318
- [92] Misseroni, D., Colquitt, D.J., Movchan, A.B., Movchan, N.V., Jones, I.S., 2015. Cymatics for the cloaking of flexural vibrations in a structured plate.
- [93] Norris, A.N., Parnell, W.J., 2012. Hyperelastic cloaking theory: transformation elasticity with pre-stressed solids. *Proc. R. Soc. A* 468, 2881-2903.
- [94] Ru, C.Q., 1998. Interface design of neutral elastic inhomogeneities. *Int. J. Solid Struct.* 35, 559-572.
- [95] Ru, C.Q., Schiavone, P., 1997. A circular inhomogeneity with circumferentially inhomogeneous interface in antiplane shear. *Proc. R. Soc. A* 453, 2551-2572.
- [96] Vasudevan, M., Schiavone, P., 2005. Design of neutral elastic inhomogeneities in plane elasticity in the case of non-uniform loading. *Int. J. Eng. Sci.* 43, 1081-1091.
- [97] Wang, X. Schiavone, P., 2014. Harmonic circular inclusions for non-uniform fields through the use of multicoating. *Quart. Appl. Math.* 72, 267-280.
- [98] Livieri, P., 2008. Use of J-integral to predict static failures in sharp V-notches and rounded U-notches. *Eng. Fract. Mech.* 75, 1779-1793.

- [99] Weichen, S., 2011. Path-independent integral for the sharp V-notch in longitudinal shear problem, *Int. J. Solid Struct.* 48, 567-572.
- [100] Weichen, S., 2014. Equivalence of the notch stress intensity factor, tip opening displacement and energy release rate for a sharp V-notch. *Int. J. Solid Struct.* 51, 904-909.
- [101] Duan, J., Li, X., Lei, Y., 2012. A note on stress intensity factors for a crack emanating from a sharp V-notch. *Eng. Fract. Mech.* 90, 180-187.
- [102] Lazzarin, P., Zappalorto, M., 2008. Plastic notch stress intensity factors for pointed V-notches under antiplane shear loading. *Int. J. Fract.* 152, 1-25.
- [103] Noda, N.A., Takase, Y., 2003. Generalized stress intensity factors of V-shaped notch in a round bar under torsion, tension, and bending. *Eng. Fract. Mech.* 70, 1447-1466.
- [104] Zappalorto, M., Lazzarin, P., Berto, F., 2009. Elastic notch stress intensity factors for sharply V-notched rounded bars under torsion. *Eng. Fract. Mech.* 76, 439-453.
- [105] Zappalorto, M., Lazzarin, P., Berto, F., 2009. Stress concentration near holes in the elastic plane subjected to antiplane deformation. *Materials Science* 48, 415-426.
- [106] Bacca, M., Bigoni, D., Dal Corso, F., Veber, D., 2013. Mindlin second-gradient elastic properties from dilute two-phase Cauchy-elastic composites Part II: Higher-order constitutive properties and application cases. *Int. J. Solid Struct.* 50, 4020-4029.
- [107] Barbieri, E., Pugno, N.M., 2015. A computational model for large deformations of composites with a 2D soft matrix and 1D anticracks. *Int. J. Solid Struct.* 77, 1-14.
- [108] Barton, N., Lien, R. Lunde, J., 1974. Engineering Classification of Rock Masses for the Design of Tunnel Support. *Rock Mechanics* 6, 189-236

- [109] Chen, Y.Z., 2013. Evaluation of T-stress for a hypocycloid hole in an infinite plate. *Multidiscipline Model. Materials Struct.* 9, 450-461.
- [110] Chen, Y.Z., 2014. Eigenfunction expansion variational method for the solution of a cusp crack problem in a finite plate. *Acta Mech.* 168, 157-166.
- [111] Craciun, E.M., SoĂşs, E., 1998. Interaction of two unequal cracks in a prestressed fiber reinforced composite. *Int. J. Fract.*, 94, 137-159.
- [112] Chen, Y.Z., Hasebe, N., and Lee, K.Y., 2003. Multiple crack problems in elasticity. WIT press.
- [113] Chu, C.M., 1994. The stress field singularity near a cusp. *Eng. Fract. Mech.* 47, 361-365.
- [114] Dal Corso, F., Bigoni, D., Gei, M., (2008). The stress concentration near a rigid line inclusion in a prestressed, elastic material. Part I. Full field solution and asymptotics. *J. Mech. Phys. Solids*, 56, 815-838.
- [115] Dal Corso, F., Shahzad, S., Bigoni D., 2016. Isotoxal star-shaped polygonal voids and rigid inclusions in nonuniform antiplane shear fields. Part I: Formulation and full-field solution. *Int. J. Solid Struct.* 85-86, 67-75.
- [116] Dal Corso, F., Shahzad, S., Bigoni D., 2016. Isotoxal star-shaped polygonal voids and rigid inclusions in nonuniform antiplane shear fields. Part II: Singularities, annihilation and invisibility. *Int. J. Solid Struct.* 85-86, 76-88.
- [117] Gao H., 1995. Mass-conserved morphological evolution of hypocycloid cavities: a model of diffusive crack initiation with no associated energy barrier. *Proc. R. Soc. Lond. A* 448, 465-483.
- [118] Gdotus, E.E., 2003. Problem 68: Failure of a plate with a hypocycloidal inclusion, In *Problems of Fracture Mechanics and Fatigue*, E. Gdotous, C.A. Radopoulos and J.R. Yates Editors, Springer.

- [119] Gourgiotis, P.A., Piccolroaz, A., 2014. Steady-state propagation of a mode II crack in couple stress elasticity. *Int. J. Frac.* 188 (2), 119-145.
- [120] Hasebe, N., Nemat-Nasser, S., Keer, L.M., 1984. Stress analysis of a kinked crack initiating from a rigid line inclusion. Part II: Direction of propagation. *Mech. Mat.*, 3 (2), 147-156
- [121] Homencovski, D., Dascalu, C., 2000. Uniform asymptotic solutions for lamellar inhomogeneities in plane elasticity. *J. Mech. Phys. Solids*, 48, 153-173
- [122] Kohno, Y., Ishikawa, H., 1995. Singularities and stress intensities at the corner point of a polygonal hole and rigid polygonal inclusion under antiplane shear. *Int. J. Eng. Sci.* 33, 1547-1560.
- [123] Ivanov, V.I., Trubetskov, M.K., 1994. *Handbook of Conformal Mapping with Computer-Aided Visualization*. CRC Press.
- [124] Misseroni, D., Dal Corso, F., Shahzad, S., Bigoni, D., 2014. Stress concentration near stiff inclusions: Validation of rigid inclusion model and boundary layers by means of photoelasticity. *Eng. Fract. Mech.* 121-122, 87-97.
- [125] Kumar, J. 2006. Stress Reduction Coefficient and Amplification Factor for Seismic Response of Ground. *Int. J. Geomech.* 6, 141-146.
- [126] Misra, S., Mandal, N., 2007. Localization of plastic zones in rocks around rigid inclusions: insights from experimental and theoretical models. *J. Geophys. Res.* 112, B09 206.
- [127] Moon, H.J., Earmme, Y.Y., 1998. Calculation of elastic T-stresses near interface crack tip under in-plane and anti-plane loading. *Int. J. Fract.* 91, 179-195.
- [128] Movchan, A.B., Movchan, N.V., 1995. *Mathematical Modelling of Solids with Nonregular Boundaries*. CRC Press.
- [129] Movchan, A.B., Movchan, N.V., Poulton, C.G., 2002. *Asymptotic Models of Fields in Dilute and Densely Packed Composites*. Imperial College Press.

- [130] Nik Long, N.M.A., Yaghobifar, M., 2011. General analytical solution for stress intensity factor of a hypocycloid hole with many cusps in an infinite plane. *Philosophical Magazine Letters* 91:4, 256-263.
- [131] Noselli, G., Dal Corso, F. and Bigoni, D., 2010. The stress intensity near a stiffener disclosed by photoelasticity. *Int. J. Fract.* 166, 91-103.
- [132] Ozturk, T., Poole, W.J., Embury, J.D., 1991. The deformation of Cu-W laminates. *Mater. Sci. Eng. A* 148, 175-178.
- [133] Panasyuk, V.V., Berezhnitskii, L.T. and Trush, I.I., 1972. Stress distribution about defects such as rigid sharp-angled inclusions. *Physico-mechanical institute of the academy of science of Ukrainian SSR, L'vov*. Translated from *Problemy Prochnosti* 7, 3-9.
- [134] Panasyuk, V.V., Buina, E.V., 1966. Threshold equilibrium of a plate weakened by a polygonal hole. *Fiziko-Khimicheskaya Mekhanika Materialov* 2, 15-20.
- [135] Panasyuk, V.V., Buina, E.V., 1967. Critical stress diagrams for brittle materials with defects of the cusped void/crack type. *Fiziko-Khimicheskaya Mekhanika Materialov*, 3, 584-591.
- [136] Piccolroaz, A., Mishuris, G., Movchan, A.B., 2010. Perturbation of mode III interfacial cracks. *Int. J. Frac.* 166, 41-51.
- [137] Radaj, D., 2013. State-of-the-art review on extended stress intensity factor concepts. *Fatigue Fract. Eng. Mat. Str.* 37, 1-28.
- [138] Radi, E., 2007. Effects of characteristic material lengths on mode III crack propagation in couple stress elastic-plastic materials. *Int. J. Plast.* 23 (8), 1439-1456.
- [139] Schiavone, P., 2003. Neutrality of the elliptic inhomogeneity in the case of non-uniform loading. *Int. J. Eng. Sci.* 8, 161-169.
- [140] Sih, G.C., 1965. Stress Distribution Near Internal Crack Tips for Longitudinal Shear Problems. *J. Appl. Mech.* 32, 51-58.

- [141] Vasudevan, M., Schiavone, P., 2006. New results concerning the identification of neutral inhomogeneities in plane elasticity. *Arch. Mechanics* 58, 45-58.
- [142] Vigdergauz, S., 2007. Shape-optimization of a rigid inclusion in a shear-loaded elastic plane. *J. Mech. Materials Structures* 2, 275-291.
- [143] Vigdergauz, S., 2008. Energy-minimizing inclusion in an elastic plate under remote shear. *J. Mech. Materials Structures* 3, 63-83.
- [144] Wang, X., Schiavone, P. 2014. Finite deformation of harmonic solids with cusp cracks. *IMA J. Appl. Math.* 79, 790-803.

